A biophysical study of the dynamic process of surface bacterial colonisation

Emilia Maria Hudzik

A thesis presented for the degree of
Doctor of Philosophy

Department of Physics and Astronomy
The University of Sheffield
June 2024

Contents

List of Figures

List of Tables

Abstract

Bacteria colonise surfaces to form biofilms, which are communities that can cause persistent contamination or infections. Understanding the early stages of biofilm formation and the factors that influence it is crucial for developing better prevention strategies. However, capturing the dynamic process of bacterial adhesion and growth on surfaces in real time remains challenging. This study addresses that gap by using a biophysical approach to monitor and characterise surface colonisation by bacteria under various conditions.

Quartz crystal microbalance with dissipation (QCM-D) was used to monitor bacterial adhesion and biofilm formation on gold surfaces in real time. Two model bacteria were studied: *Staphylococcus aureus* (Gram-positive) and *Pseudomonas aeruginosa* (Gram-negative). The effects of varying nutrient availability, temperature, and the presence of a quorum sensing inhibitor on biofilm development were examined. Complementary biofilm assays and imaging were performed to confirm and expand upon the QCM-D observations.

QCM-D captured distinct patterns of surface colonisation and biofilm growth, which were consistent with microscopy and biomass measurements. Both species formed much more extensive biofilms in nutrient-rich broth than in nutrient-poor medium, and a higher temperature (37 °C) accelerated biofilm development compared to room temperature (25 °C). *S. aureus* and *P. aeruginosa* exhibited markedly different adhesion behaviours: *S. aureus* rapidly formed multilayered clusters resulting in a soft, highly viscoelastic biofilm, whereas *P. aeruginosa* adhered more gradually and produced thinner, stiffer biofilm layers. In *S. aureus*, inhibiting quorum sensing with savirin delayed biofilm maturation, prolonging the initial attachment phase and reducing overall biofilm accumulation. Comparisons with inert silica colloidal particles indicated that physical deposition alone could mimic the early stage of adhesion, but live bacteria diverged by actively aggregating and producing a viscoelastic polymer matrix.

These findings demonstrate the effectiveness of QCM-D for real-time biofilm monitoring and reveal how growth conditions and microbial traits shape biofilm formation. The study highlights that *S. aureus* and *P. aeruginosa* employ different strategies to colonise surfaces, and that interfering with bacterial signalling can modulate biofilm development. Overall, this work provides a more comprehensive biophysical understanding of how biofilms develop on surfaces, which could inform the design of targeted strategies to control or prevent biofilm-related issues.

Streszczenie

Bakterie kolonizują powierzchnie, tworząc biofilmy – złożone społeczności komórek, które mogą powodować długotrwałe skażenia lub przewlekłe infekcje. Zrozumienie wczesnych etapów powstawania biofilmu oraz czynników wpływających na ten proces jest kluczowe dla opracowania skuteczniejszych strategii zapobiegania. Uchwycenie dynamicznego przebiegu adhezji i wzrostu bakterii na powierzchniach w czasie rzeczywistym pozostaje jednak wyzwaniem. Niniejsza praca podejmuje to zagadnienie, wykorzystując podejście biofizyczne do monitorowania i scharakteryzowania kolonizacji powierzchni przez bakterie w różnych warunkach.

Wykorzystano mikrowagę kwarcową z pomiarem dyssypacji (QCM-D) do monitorowania adhezji bakterii i formowania biofilmu na złotych powierzchniach w czasie rzeczywistym. Badano dwa gatunki modelowe: *Staphylococcus aureus* (Gram-dodatnia) i *Pseudomonas aeruginosa* (Gram-ujemna). Zbadano wpływ dostępności substancji odżywczych, temperatury oraz obecności inhibitora 'quorum sensing' na rozwój biofilmu. Dodatkowo, w celu potwierdzenia wyników QCM-D, przeprowadzono klasyczny test biofilmu z fioletem krystalicznym oraz obserwacje mikroskopowe.

Pomiary QCM-D zarejestrowały charakterystyczne wzorce kolonizacji powierzchni i wzrostu biofilmu, zgodne z obserwacjami mikroskopowymi i pomiarami biomasy. Oba badane gatunki tworzyły znacznie obfitszy biofilm w bogatym podłożu odżywczym niż w medium ubogim, a wyższa temperatura (37 °C) przyspieszała rozwój biofilmu w porównaniu z temperaturą pokojową (25 °C). Zaobserwowano wyraźne różnice między gatunkami w sposobie zasiedlania powierzchni: *S. aureus* szybko tworzył wielowarstwowe skupiska prowadzące do powstania miękkiego, silnie lepko-sprężystego biofilmu, podczas gdy *P. aeruginosa* kolonizowała powierzchnię bardziej stopniowo, tworząc cieńszy i sztywniejszy biofilm. W przypadku *S. aureus* zahamowanie quorum sensing za pomocą saviryny opóźniało dojrzewanie biofilmu, wydłużając fazę początkowej adhezji i zmniejszając ogólną akumulację biomasy. Porównanie z inertnymi koloidalnymi cząstkami krzemionkowymi wykazało, że sama fizyczna depozycja może naśladować jedynie początkowy etap adhezji, jednak żywe bakterie zachowują się odmiennie poprzez aktywne agregowanie się i wytwarzanie lepko-sprężystej matrycy.

Uzyskane wyniki potwierdzają skuteczność metody QCM-D w monitorowaniu formowania biofilmu w czasie rzeczywistym oraz pokazują, jak warunki środowiskowe i cechy drobnoustrojów

kształtują proces powstawania biofilmu. Praca uwydatnia, że *S. aureus* i *P. aeruginosa* stosują odmienne strategie kolonizacji powierzchni, a ingerencja w komunikację bakteryjną może modulować rozwój biofilmu. Całościowo, badanie to dostarcza bardziej wszechstronnego, biofizycznego zrozumienia procesu tworzenia biofilmów na powierzchniach, co może pomóc w opracowaniu ukierunkowanych strategii zapobiegania i zwalczania tych struktur.

Acknowledgments

First and foremost, I would like to express my heartfelt gratitude to my supervisors, Prof. Mark Geoghegan and Dr Andrew Parnell. Their feedback, encouragement, and mentorship have been invaluable throughout this project, especially during the challenging times of the COVID-19 pandemic.

I am also deeply thankful to my collaborators at Arxada, Dr Jordan Petkov and Paula McGeechan. Their insightful comments, constructive feedback, and contributions were crucial to the development of this project. My visit to Blackley provided valuable insights into the motivations behind antimicrobial agent development and taught me essential microbiological techniques.

My appreciation extends to all my colleagues and friends on G floor, particularly Dr Jamie Blakeman, Dr Emily Hall, and Dr Stephanie Burg, for their unwavering support, encouragement, and camaraderie. A special thank you to Jamie for taking the time in his final year to teach me how to use the AFM and various other experimental techniques. I also thank Dr Thomas Sexton for sharing his QCM-D knowledge and skills with me.

Many individuals across the university have been instrumental in the completion of my project. In Physics and Astronomy, I am grateful to Dr Nic Mullin for his AFM expertise. In the Wolfson Light Microscopy Facility, I appreciate Dr. Darren Robinson's assistance with fluorescence imaging. I extend my gratitude to Prof. Simon Foster and Dr Mack Durham for allowing me to conduct my microbiology work in their laboratories at the School of Bioscience. Lastly, I am deeply thankful to Dr Jenn Dick, the CDT manager, for her invaluable 'behind the scenes' support.

I would also like to acknowledge the support of Dr Jacqui Papadopoulos and Dr Steven Gurr, my biology and chemistry teachers at St. Augustine's Catholic College, along with my Master's project mentor, Dr James Shipp. They have been sources of inspiration, motivation, and intellectual stimulation throughout my scientific education.

I would also like to thank my work colleagues, especially Rachit, Ammar, Jazz, Elly and Rawda, among others, for their support. Your encouragement and flexibility have made it possi-

ble for me to balance work and research effectively. I appreciate the team spirit and the positive work environment you have provided, which has been a great source of motivation during this journey.

I am profoundly grateful to my family for their unwavering support. My parents have been my pillars of strength and my biggest cheerleaders. Their sacrifices and understanding have been fundamental to my academic journey. Dziękuję wam mamo i tato. Lastly, I am deeply thankful to my boyfriend Jack, for his love, encouragement, and patience in answering countless microbiology questions.

Abbreviations

ΔD dissipation factor shift

$\Delta\Gamma$ half-bandwidth at half-maximum

Δf frequency shift (Hz)

C mass sensitivity constant (g m^{-2} Hz^{-1}))

D dissipation

N_s number density of spheres (m^{-2})

Z_q acoustic impedance of AT-cut quartz (8.8×10^6 kg m^{-2} s^{-1})

Γ halfbandwidth at half-maximum

γ damping coefficient (s^{-1})

κ_s stiffness of contact (g s^{-2})

ω resonance frequency of resonator

ω_q resonance frequency of coupled-resonator

ρ_q mass density of quartz (2.65 g cm^{-3})

υ_q quartz shear wave velocity (m s$^-$1)

f frequency (Hz)

f_0 fundamental resonant frequency (Hz)

m_f mass per unit area (g m^{-2})

m_s mass of the sphere (g)

n harmonic number

t time

P. aeruginosa *Pseudomonas aeruginosa*

S. aureus *Staphylococcus aureus*

agr accessory gene regulator

AC alternating current

AFM atomic force microscopy

ATCC American Type Culture Collection

CV crystal violet

DI deionised

DNA deoxyribonucleic acid

EPS extracellular polymeric substance

GFP green fluorescent protein

MRSA methicillin-resistant *Staphylococcus aureus*

OD optical density

OD600 optical density at 600 nm

PBS phosphate-buffered saline

PFA paraformaldehyde

PI propidium iodide

QCM quartz-crystal microbalance

QCM-D quartz-crystal microbalance with dissipation monitoring

QS quorum sensing

QSI quorum sensing inhibition/inhibitor

R2A Reasoner's 2A broth

RT room tmperature

SDS sodium dodecyl sulfate

SFCS single-cell force spectroscopy

SMCS single-molecule force spectroscopy

TSA tryptic soy agar

TSB tryptic soy broth

Chapter 1

Introduction

1.1 Bacteria

1.1.1 *Staphylococcus aureus*

Staphylococci are Gram-positive bacteria, characterised by individual cocci that divide in multiple planes to form clusters. To date, 32 species and eight subspecies within the genus *Staphylococcus* have been identified. These bacteria are non-motile, facultative anaerobes. First discovered in 1884, *Staphylococcus aureus* is now one of the most extensively characterised and studied species. The species name "aureus" is derived from the golden colour of the colonies when grown on solid media [1, 2]. *S. aureus* is the leading cause of bacterial infections worldwide, which range in severity from minor skin infections to fatal pneumonia [3]. It is also a commensal organism in humans, asymptomatically colonising the nostrils of about 30% of healthy individuals [4].

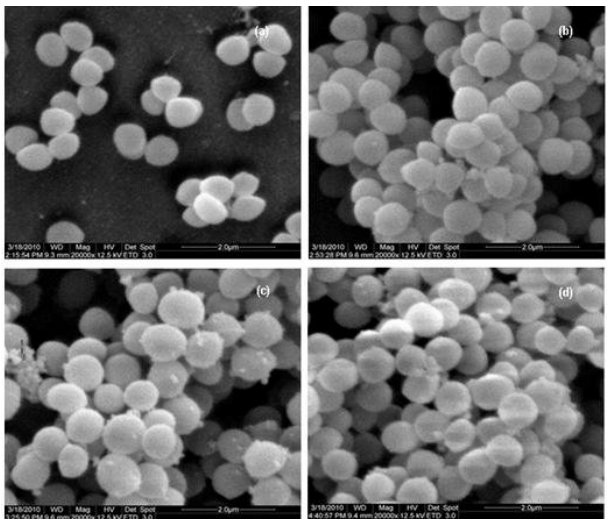

Figure 1.1: SEM images of *S. aureus* biofilms. From A*fr. J. Microbiol. Res.*, 2012, 6(13), 3284-3291, used under Creative Commons CC-BY license.[5]

S. aureus	
Domain	Bacteria
Phylum	Bacillota
Class	Bacilli
Order	Bacillales
Family	Staphylococcaceae
Genus	*Staphylococcus*
Species	*S. aureus*

Table 1.1: Taxonomy of *S. aureus*.

S. aureus has an striking capacity to develop antibiotic resistance,[6] which elevates its significance as a pathogen in the context of growing antibiotic resistance. Epidemics of antibiotic-resistant *S. aureus* have arisen in the past 60 years. The commonly used benzylpenicillin was no longer effective for the treatment of most *S. aureus* infections within 10 years of its introduction for use in humans, and penicillin-resistant strains became endemic throughout the late 1950s[7]. Methicillin-resistant *Staphylococcus aureus* (MRSA) was first reported in 1961, only two years after the antibiotic was introduced to treat the penicillin-resistant strain. MRSA spread worldwide over the next several decades and is now endemic in most hospitals and healthcare facilities. A key concern for the treatment of MRSA infections is the increasing prevalence of multidrug resistance [8–10].

The *S. aureus* cell wall is primarily composed of peptidoglycan and teichoic acids (phosphate-containing polymers). These components create a strong protective coat, integral to the formation of compact, layered cell wall networks capable of withstanding high internal osmotic pressure [11, 12]. They also contribute a negative charge to the cell surface. The cell wall structure includes surface proteins, exoproteins, and peptidoglycan hydrolases. These components are involved in bacterial attachment to surfaces and are therefore key to staphylococcal virulence.[13, 14]

1.1.2 *Pseudomonas aerugionsa*

The Gram-negative, facultatively anaerobic bacilli of the *Pseudomonas* genus are common inhabitants of soil, marine, and freshwater environments. The genus comprises over 120 species, which are ubiquitous in wet environments such as water and soil ecosystems [15, 16]. The production of pigments such as pyoverdine (yellow-green) and pyocyanin (blue-green) in *Pseudomonas* species makes them easily identifiable on agar.[17, 18]

Interestingly, *Pseudomonas aeruginosa* can decompose hydrocarbons and has been used to break down oil and tarballs resulting from oil spills [20]. However, research interest in *P. aeruginosa* is primarily due to its considerable medical importance, as it is the species most frequently associated with causing human infection. It is is an opportunistic pathogen capable of extensive

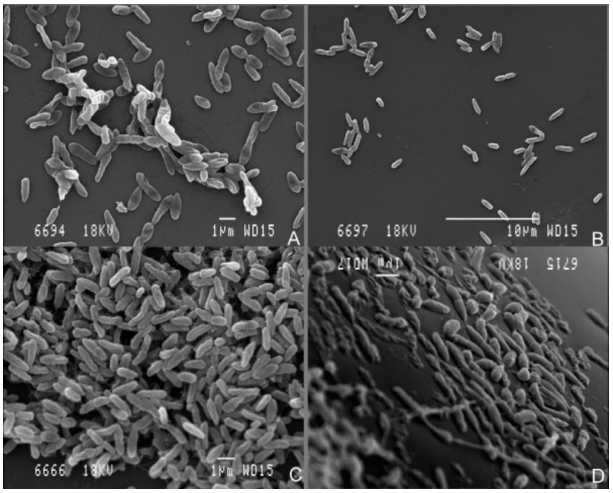

Figure 1.2: Scanning electron microscopy (SEM) images *P. aeruginosa* attachment and biofilm formation on glass. From *BMC Microbiol.*, 2010, 1(10), 38, used under Creative Commons CC-BY license.[19]

P. aeruginosa	
Domain	Bacteria
Phylum	Pseudomonadota
Class	Gammaproteobacteria
Order	Pseudomonadales
Family	Pseudomonadaceae
Genus	*Pseudomonas*
Species	*P. aeruginosa*

Table 1.2: Taxonomy of *P. aeruginosa*.

colonisation, known for its ubiquity, multidrug resistance, and antibiotic resistance mechanisms [21–23]. These enduring biofilms contribute to its association with causing nosocomial infections in immunocompromised patients. It is known for its ability to establish permanent residency in the airways of cystic fibrosis patients and for being the most commonly isolated bacterium colonising severe burns and wound infections [24, 25].

Type IV pili are a type of cell appendage and can be found attached to the cell surface of *P. aeruginosa*. These pili have been shown to account for 90% of the adherence, function, and virulence in a mouse infection model [26]. Type IV pili also assist in facilitating 'twitching motility'—the retraction and extension of pili—which aids in bacterial movement and colonisation.[27–29]

1.1.3 The bacterial cytoskeleton

The cytoskeleton is a complex network of protein filaments found within cells, crucial for maintaining cell shape, enabling cellular movement, and ensuring the proper organisation of internal

structures. In bacteria, the cytoskeleton, though simpler than its eukaryotic counterpart, is vital for various cellular processes, including cell division, shape maintenance, and intracellular transport. This dynamic framework allows bacteria to adapt to different environmental conditions and supports their survival and pathogenicity.[30]

Key components of the bacterial cytoskeleton include several protein structures, each performing specific functions (Fig. 1.3). The only cytoskeletal element present in spherical bacteria such as *S. aureus* is the tubulin-like cell division protein FtsZ. FtsZ localises in a ring at the onset of cell division, recruits other cell division proteins, and defines the division plane. In rod-shaped bacteria, such as *P. aeruginosa*, additional cytoskeletal elements are present. For instance, most rod-shaped bacteria contain one or more actin-like MreB homologues, which exhibit helix-like localisation patterns and are essential for cell width control. At the onset of cell division, the FtsZ ring forms and defines the division plane in these bacteria as well.[30, 31]

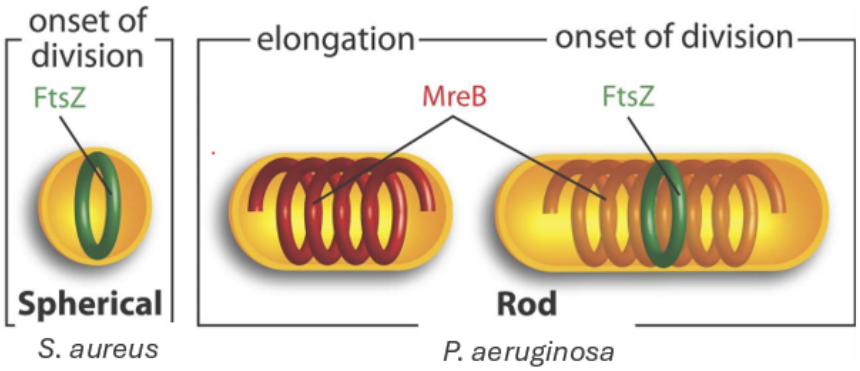

Figure 1.3: The bacterial cytoskeleton. Adapted from *J. Cell Biol.*, 2007, 179(3), 381–387. Used under Creative Commons CC BY-NC-SA 4.0 license.[31]

The bacterial cytoskeleton indirectly impacts adhesion and colonisation by influencing the shape and structural integrity of bacterial cells. A well-defined cell shape and robust cell wall are essential for the effective functioning of surface proteins involved in adhesion. For example, the proper localisation and functioning of adhesins, pili, and other surface structures depend on the overall architecture of the bacterial cell, which is maintained by the cytoskeleton. Additionally, the cytoskeleton plays a role in the spatial organisation of the cell surface, ensuring that adhesins and other attachment factors are positioned optimally to interact with host tissues or abiotic surfaces.[32]

Moreover, the cytoskeleton can influence the ability of bacteria to form biofilms. The formation and maintenance of biofilms require coordinated cell movement and division, processes that are heavily dependent on a functional cytoskeleton. For instance, the twitching motility facilitated by Type IV pili in *P. aeruginosa* is supported by the cytoskeleton, enabling the bacteria to move across surfaces and establish biofilms more effectively.[32]

1.1.4 Differences Between Gram-Positive and Gram-Negative Bacteria

Bacteria can be classified into two major groups: Gram-positive and Gram-negative. This classification is based on the Gram staining technique, developed by Hans Christian Gram in 1884, which differentiates bacteria by the structural and chemical composition of their cell walls, which significantly influence their adhesion and colonisation capabilities.[33]

Gram-positive bacteria are characterised by a thick peptidoglycan layer that constitutes the majority of their cell wall. This dense, multilayered structure is rich in teichoic acids and lipoteichoic acids, which contribute to the rigidity of the cell wall and its overall negative charge. During the Gram staining process, the thick peptidoglycan layer retains the crystal violet stain, causing Gram-positive bacteria to appear purple under a microscope. This robust peptidoglycan layer not only provides structural support but also plays a crucial role in the initial stages of adhesion to surfaces, which is vital for colonisation and infection. The dense peptidoglycan layer also contains surface proteins that function as adhesins, facilitating the attachment to host tissues and abiotic surfaces. For example, in *S. aureus*, surface proteins such as clumping factor and fibronectin-binding proteins are vital for its ability to adhere to and colonise host tissues.[34, 35]

In contrast, Gram-negative bacteria possess a more complex cell envelope structure. Their cell wall is composed of a thin peptidoglycan layer located within the periplasmic space, sandwiched between an inner cytoplasmic membrane and an outer membrane. The outer membrane is unique to Gram-negative bacteria and contains lipopolysaccharides (LPS), phospholipids, and proteins, which provide a formidable barrier to many antibiotics and harmful substances. During Gram staining, the thin peptidoglycan layer does not retain the crystal violet stain and instead takes up the counterstain (safranin), causing Gram-negative bacteria to appear pink or red under a microscope. The outer membrane's LPS plays a significant role in interactions with host cells and contributes to the pathogenicity of these bacteria.[36, 37]

The differences in cell wall structure between Gram-positive and Gram-negative bacteria lead to distinct adhesion strategies. Gram-positive bacteria rely on the robust, thick peptidoglycan layer and associated adhesins to establish strong and stable attachments to surfaces. This is particularly advantageous in environments like host tissues where long-term stability and resistance to mechanical and immune clearance are crucial.[39, 40] On the other hand, Gram-negative bacteria, with their complex outer membrane and surface structures, are better equipped to adapt to diverse environments.[40] Their ability to form biofilms and utilise various motility mechanisms, such as twitching motility facilitated by Type IV pili, enables them to adapt to a wide range of environments, move across surfaces, and form biofilms that are resilient and responsive to environmental changes.[41, 42]

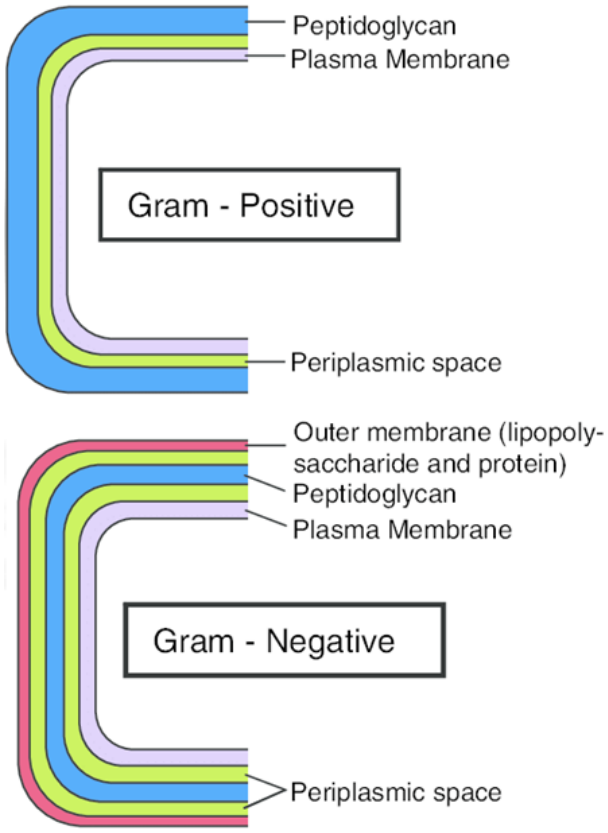

Figure 1.4: Gram classification diagrams. Adapted from *J. Nanosci. Nanotechnol.*, 2012, 12(6), 5004-5008. Used under Creative Commons CC BY 4.0 license.[38]

1.2 Bacterial adhesion

The process of bacterial adhesion can be divided into three distinct stages: approach to the surface, initial reversible attachment, and irreversible adhesion. These stages are influenced by three main factors: the liquid environment, the characteristics of the surface, and the physiology of the bacterial cell.[43]

Approaching the surface

The process of bacterial attachment begins when bacterial cells come into close proximity with a surface. This critical step can be achieved through passive or active means. All bacteria are subject to Brownian motion and gravitational forces, which can bring cells near a surface [44]. However, motility present in certain self-propelling bacteria is a more efficient way of reaching the surface. This active movement is driven by flagella, which generate propulsive force through their rotation. Flagella-containing bacteria can swim directionally towards a surface in response to environmental cues such as nutrient availability, light, oxygen levels, and temperature [45]. Additionally, motile bacteria can be attracted to surfaces by other bacteria, either of the same or different species, through electrical signalling.[46]

Flow and shear rates greatly affect the efficiency of bacteria approaching a surface. The dynamics of flow in the bulk liquid environment are influenced by the surface, with the flow rate being negligible at the hydrodynamic boundary layer (liquid-surface interface) near the surface. The size of the hydrodynamic boundary layer depends on the flow rate in the bulk liquid; generally, the higher the flow rate, the thinner the boundary layer. Consequently, bacteria near the surface are subjected to higher shear forces at high flow rates and are transported with the flow, reducing their chances of approaching the surface.[47]

Swimming is randomly altered by Brownian motion in the bulk liquid, and this phenomenon increases near the surface boundary. This results in more circular trajectories, enabling bacteria to spend more time close to the surface. Furthermore, drag forces on the bacterial cell are stronger near the surface, resulting in decreased swimming velocity compared to the bulk liquid environment [48]. Additionally, extracellular appendages present on some bacterial cells can help increase residence time near the surface. For example, pili can affect near-surface swimming by creating intermittent mechanical contacts with the surface. Once near the surface, bacteria use a variety of methods such as chemotaxis and active motility to achieve close proximity.[49]

Bacterial adhesion forces

Adhesion occurs if the sum of the attractive forces between the cell and the surface outweighs the sum of the repulsive ones. Multiple forces act on the cells at long range, tens of nanometres away from the surface. The longest-range interactions are van der Waals forces, which aid in cell-surface adhesion when the cell is close to the surface where their magnitude is greatest [50]. However, the magnitude of van der Waals forces decreases sharply with distance from the surface, and repulsive forces prevent cell attachment if the bacterium is not close enough.

Electrostatic interactions, determined by the ionic strength and pH of the liquid environment, also play a critical role. These interactions can either attract or repel bacterial cells depending on the charge distribution of the cell and the surface. Lastly, hydrophobic interactions can be either attractive or repulsive, depending on the composition of the liquid environment and the chemistries of the cell and surface.[51]

Steric forces are another type of interaction that contributes to cell adhesion. Bacteria such as *P. aeruginosa* and *Escherichia coli* possess a system of biopolymers, such as polysaccharide chains, known as the polymeric brush layer. The charge and composition of this layer are species-dependent and determine the nature of the long-range steric forces. Studies have demonstrated that these steric interactions can be more significant than van der Waals and electrostatic interactions in cell adhesion.[51]

Physical and chemical surface properties

Bacteria can colonise all natural and man-made materials. Although cell surface composition varies, bacteria are typically negatively charged. This means that surface materials with positive to neutral charges are preferentially colonised [52]. Similarly, bacteria with hydrophobic cell surfaces colonise hydrophobic materials more readily, and vice versa. [53]

The efficiency of adhesion is also largely dependent on the physical and chemical properties of the surface. Charge and hydrophobicity are two major factors affecting cell-surface interaction. Surface hydrophobicity can be altered by surface patterning, making surface topography an important factor in bacterial attachment. For example, microscopic-sized surface structures increase surface area and reduce shear experienced by cells, promoting bacterial adhesion. It has been shown that some bacteria attach preferentially to certain micropatterned substrates compared to smooth surfaces [54, 55]. However, opposing findings exist for studies examining adhesion to nanopatterned substrates, where the features are smaller than the cell size. Previous studies show impaired adhesion of Staphylococcus aureus [56] and no effect on *P. aeruginosa* and *E.coli*.[57] More recent studies, however, show a decrease in adhesion of all three bacteria types [55, 58, 59].

Organic and inorganic molecules present in the bulk liquid may be deposited on the surface, forming a conditioning film. These films alter physicochemical surface properties such as charge, potential, or surface tension. The film composition varies widely, with its components originating from the liquid environment as well as being generated by either planktonic or attached bacteria [60]. *P. aeruginosa* has been shown to secrete Psl exopolysaccharide upon reaching a clean surface, creating microcolony nucleation sites that planktonic cells preferentially bind to.[61] Conversely, biosurfactants deposited by P. aeruginosa have been shown to inhibit bacterial adhesion.[62]

Bacterial cell surface and appendages

A variety of proteins, lipids, and exopolysaccharides, as well as structures such as flagella and pili, can be found on the cell surface. These components directly or indirectly impact the process of adhesion. The conformation of this heterogeneous environment is largely dependent on conditions such as pH and ionic strength, which influence the cell surface charge and hydrophobicity. These factors can vary within a single bacterial population, affecting adhesion efficiency [63].

Flagella not only propel bacterial cells but also act as adhesins, aiding reversible adhesion by increasing cell-surface contact area. They are used to probe the nearby surface topography and approach environments that would otherwise be inaccessible to the comparatively large cell body, thereby optimising cell position and ultimately facilitating irreversible adhesion [65].

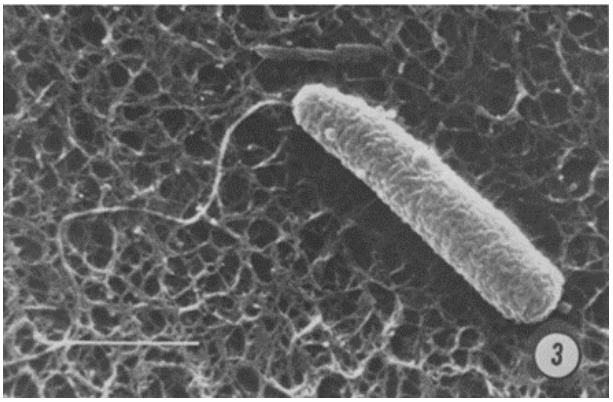

Figure 1.5: Single flagellated *P. aeruginosa* cell. From *Microbiol. Immunol.*, 1982, 26(2), 113-117, used under Creative Commons CC-BY license.[64]

Besides flagella, other extracellular appendages aid in the adhesion of many Gram-positive and Gram-negative bacteria. These thin fibres include pili, fimbriae, and curli. Although some pili, such as type I pili in Escherichia coli, possess specific receptors, most pili bind to a varied range of nonspecific substrates. Studies have shown dynamic pilus activity, involving repeated extension and retraction upon reaching the surface, which increases the efficiency of cell attachment.[49]

However, the presence of surface appendages does not always lead to more efficient adhesion. This is illustrated by the phenomenon of surface shielding, wherein longer adhesins sterically restrict the interaction between shorter appendages and the surface. For example, E. coli possesses short adhesins that are blocked by longer appendages such as lipopolysaccharides and fimbriae.[44]

Irreversible attachment

Once bacteria are sufficiently close to the surface after overcoming the repulsive forces, they strengthen their adhesion to achieve more permanent attachment. The cells and their appendages optimise their positioning, and adhesin molecules are generated to mature the cell-surface interactions. Once the irreversible adhesion of single cells is attained, biofilm formation is initiated.[56]

1.3 Bacterial colonisation

1.3.1 Bacterial proliferation in liquid media

S. aureus is known for its robust growth in various liquid media. Literature indicates that the doubling time of *S. aureus* in nutrient-rich broth, such as tryptic soy broth (TSB), is approximately 20-30 minutes under optimal conditions (37°C, pH 7.0) [66]. However, in minimal

buffer solutions, the doubling time can extend significantly, often ranging between 40-60 minutes depending on the availability of essential nutrients and environmental factors.[67] Studies conducted over a 24-hour period show that *S. aureus* can achieve substantial population growth in TSB, reaching stationary phase within 8-10 hours. In contrast, growth in minimal buffer solutions is slower, with the stationary phase often not reached within the 24-hour timeframe. These findings highlight the adaptability of *S. aureus* to different aqueous environments, albeit with varying growth rates depending on the nutrient composition of the media.[68, 69]

P. aeruginosa exhibits an ability to proliferate in a wide range of liquid media. The literature reports a doubling time of approximately 30-45 minutes in nutrient-rich conditions, under optimal conditions (37°C, pH 7.0).[70] Similar to *S. aureus*, the doubling time of *P. aeruginosa* increases in minimal buffer solutions, often extending to 60-140[71, 72] minutes depending on the nutrient availability and environmental factors. Over a 24-hour experimental period, *P. aeruginosa* demonstrates rapid growth in nutrient-rich, typically reaching the stationary phase within 10-12 hours. In minimal buffer solutions, the growth rate is slower, and the stationary phase may not be achieved within 24 hours. The ability of *P. aeruginosa* to adapt to various aqueous environments underscores its versatility and resilience, which are key factors contributing to its pathogenicity and persistence in clinical settings.[41, 42]

1.3.2 Biofilms

The majority of bacteria exist in collaborative surface communities known as biofilms. Suspended organic material deposits on horizontal surfaces, promoting growth and division in surface-attached microbes due to a high local nutrient concentration. Sessile bacteria encase themselves in a matrix that serves various mechanical functions, such as providing structural rigidity and protection from the external environment, including shear forces caused by fluid flow [73–77]. Additionally, biofilm-bound bacteria benefit from antibiotic resistance, as the matrix acts as a physical barrier against antimicrobial agents and host immune defences [78–80]. The matrix also hosts dormant persister cells [81] and small colony variants [82], which are linked to persistent and highly resistant infections. Consequently, biofilms create favourable microbial environments, ultimately enhancing the pathogenicity of bacteria.

Fig.1.6 illustrates the biofilm life cycle. The process begins with the deposition of a conditioning film on a surface, consisting of organic materials such as proteins and polysaccharides that aid in the adhesion of planktonic bacteria. Bacteria can reach the surface through Brownian motion or active movement using surface appendages such as flagella, seeking the higher nutrient environment of the surface. The colonising bacteria then attach reversibly using weak interactions such as van der Waals forces. At this stage, bacteria can detach and return to a planktonic mode. Irreversible attachment follows the initial weak interaction and arises due to hydrophobic/hydrophilic interactions, as well as surface structures such as flagella, pili, and

lipopolysaccharides that aid in attachment by overcoming electrostatic repulsion [71, 79, 83–85]. Stronger attachment is accompanied by residence-time dependent cell wall deformation [86], requiring detergents, enzymes, or heat to remove the biofilm.

Following their irreversible attachment, bacteria become encased in a self-generated matrix known as the extracellular polymeric substance (EPS). This matrix comprises proteins, polysaccharides, lipids, and nucleic acids [87–89]. The protective and structural properties of the EPS allow for biofilm maturation, where cells form complex 3D structures containing water channels, facilitating the distribution of nutrients and autoinducers [90]. The bacterial population is then propagated as cells detach and disperse to new sites. Cells can be released due to fluid shear or enzyme-enabled self-degradation.[91]

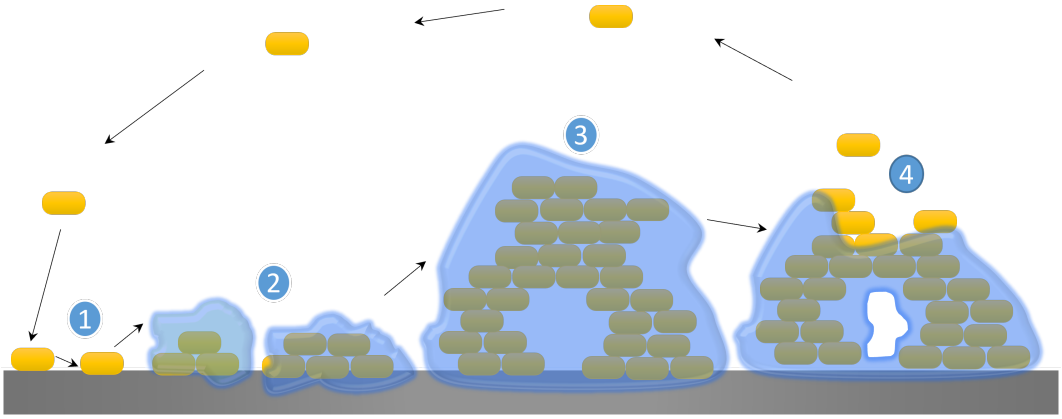

Figure 1.6: Diagram of the biofilm lifecycle stages. (1) Initial reversible, then permanent attachment. (2) Microcolony formation through growth and division at the substrate. Onset of EPS production. (3) Development of complex 3D structures and biofilm maturation. (4) Dispersal of planktonic bacteria. Colonisation of new environments follows.

1.3.3 Quorum sensing

The growth and initial biofilm formation are regulated by a process known as quorum sensing (QS). Quorum sensing is the regulation of gene expression in response to fluctuations in cell density. This process involves the production of chemical signals, known as autoinducers, which increase in concentration as a function of cell density [92–94]. When a minimal threshold concentration of an autoinducer is detected, it leads to an alteration in gene expression. Autoinducers facilitate communication between cells by controlling population density and stimulating phenotypic changes.[95]

Both Gram-positive and Gram-negative bacteria use QS to regulate various physiological processes, including virulence, antibiotic production, motility, sporulation, and biofilm formation [96]. In most Gram-negative bacteria, the autoinducers are acylated homoserine lactones [92], whereas Gram-positive bacteria use processed oligopeptides [97]. Recent advances in the

field indicate that QS occurs both within and between different bacterial species.[98, 99]

1.4 Characterising bacteria on surfaces

1.4.1 Optical methods

Optical methods have played a pivotal role in the study of bacterial attachment and proliferation[43]. Typically, biofilms are grown in well plates and stained using a dye. The dyes bind to cells, and the amount of dye corresponds to the biofilm biomass. Crystal violet (CV) is a commonly used dye, known for its use in the Gram staining method, with a maximum absorbance at 590 nm under standard conditions. It works by staining the nuclei of adherent cells, acting as an intercalating dye. This allows for the quantification of deoxyribonucleic acid (DNA), which is proportional to the number of cells, by measuring the optical density (OD) of the resulting suspension of stained cells. This technique allows for the study of biofilms under varying conditions, such as different nutrient densities or the presence of antibiotics.[100] Unfortunately, the fact that CV is a disruptive assay strongly limits its use for time-dependent characterisation.

The crystal violet assay does not differentiate between live and dead bacteria. To distinguish the two, combinations of dyes are used simultaneously. Propidium iodide (PI) and SYTO 9™are two fluorescent dyes that bind to DNA and are commonly used together. SYTO 9™ can cross the cell membrane and mark both live and dead cells, while PI cannot penetrate the membranes of live cells and therefore only attaches to cells with compromised membranes. Information such as cell location and surface biofilm coverage is then obtained using fluorescence microscopy images.[101]

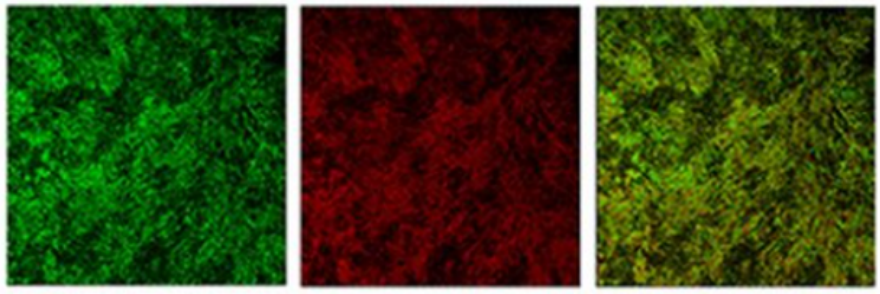

Figure 1.7: Live/Dead bacteria staining assay of a dual-species biofilm (textitStreptococcus mutans and *Streptococcus sanguinis*) - live (green), dead (red) and combined. From Sci. Rep., 2019, 9, 1, 6689-6689, used under Creative Commons CC-BY license.[102]

A disadvantage associated with the use of stains is insufficient penetration of thicker films during shorter contact times, and cell toxicity arising during longer incubation times [103–105]. Fluorescent reporter plasmids resolve these issues. Green fluorescent protein (GFP) labelled *S. aureus* is one of the most studied examples [106]. The reporter plasmids[107] facilitate cell

labelling for a range of experimental applications such as monitoring gene expression, carrying out host interaction studies, and observing biofilm development.[108–110]

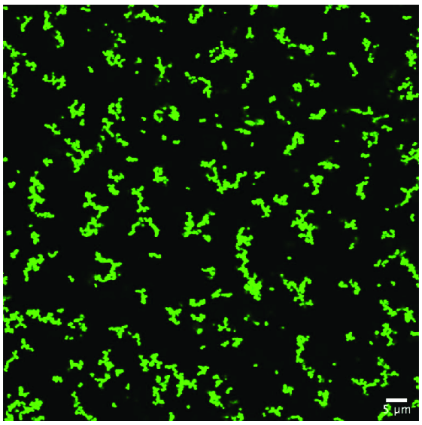

Figure 1.8: Confocal microscopy of GFP-tagged *S. aureus* synovial fluid-induced aggregates 1-hour post exposure, used under Create Commons CC BY-NC-ND 4.0 license.[111]

1.4.2 Atomic force microscopy

Building upon scanning tunnelling microscopy, the atomic force microscope was introduced in 1986 as a method of probing surfaces at the nanometre scale. A major improvement of the method was the removal of the previous prerequisite for samples to be electrically conductive. This enabled the study of biological samples at resolutions beyond the diffraction limit.[112]

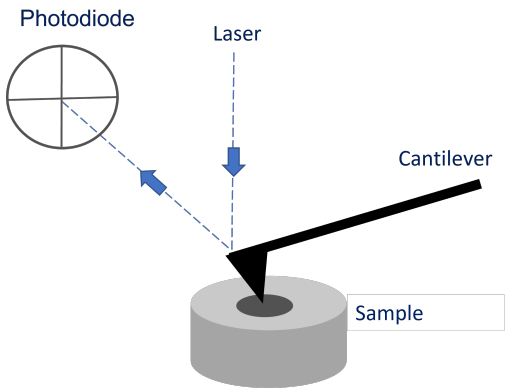

Figure 1.9: Simple diagram representing the core components of an AFM setup in which a laser diode reflects off the back off a cantilever onto an XYZ photodiode.

The technique involves the use of a cantilever, which ends with a sharp tip. The cantilever is brought close to a surface, and the resulting interactions cause it to bend up or down. A laser is reflected off the back of the cantilever (Fig. 1.9) onto a photodiode, which converts the small cantilever movements, as it rasters across a surface, into computer signals. The voltage produced by the photodiode depends on the position of the laser on it. Topography changes or

cantilever adhesion to the sample result in vertical movement, whereas frictional forces twisting the cantilever lead to lateral displacement. Ultimately, the laser position is translated into changes in surface topography during imaging experiments [113, 114]. The use of piezoelectrics enables the sub-nanometre precision of the technique. Piezoelectricity is a phenomenon in which the electrical and mechanical states of a material are coupled. The faces of the material become charged as it is deformed, and when the material is subjected to an electric field, it becomes deformed. A potential difference applied to a four-quadrant piezoelectric tube alters its dimensions, enabling movement in the X and Y axes as it extends and retracts. The tube extends when voltage is applied to all quadrants, enabling movement in the Z direction.[115]

Feedback loop

Without the feedback loop employed, the force experienced by the cantilever is continually varied, and since the forces between the tip and sample are not controlled, strong interactions can damage the tip or surface. The feedback loop maintains constant deflection or amplitude of the cantilever, depending on the mode of operation of the AFM. The position of the z-piezo is compared to a specified set point, and the difference between these values is known as the error signal. The feedback loop reduces this error signal by adjusting the voltage applied to the z-piezo, ensuring that the measured value is close to the set point.[116]

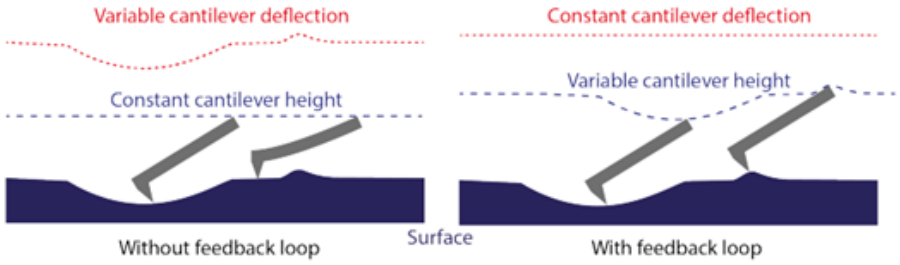

Figure 1.10: Feedback loop in contact mode. Without the feedback loop the height of the cantilever is maintained, with cantilever deflection being converted into height information. When the feedback loop is engaged the deflection is constant as the piezo moves the cantilever accordingly by the piezo, with the cantilever height being converted to height data.[117]

Tapping mode

AFM imaging can be separated into two different modes: static and dynamic. In the static mode, described above, the cantilever is in physical contact with the probed surface. With a feedback loop engaged, the z-piezo moves the tip vertically as it encounters features of different sizes to maintain a constant force.[114]

Dynamic mode imaging, often called tapping mode (also known as alternating current (AC) or intermittent contact mode), involves the oscillation of the cantilever at its resonant frequency. As the probe approaches the surface, the amplitude signal is recorded. Tall features dampen the oscillation while depressions in the surface increase it. These variations in amplitude are then translated into a height profile. Typically, the tip is moved by the z-piezo motor to maintain a constant amplitude with the use of the feedback loop. The height profile of the surface is therefore captured from the z-piezo movements.[118]

Dynamic methods of scanning are preferred for studying biological samples due to decreased vertical applied forces and the elimination of lateral forces, which can otherwise easily disturb the samples [113]. Tapping mode imaging of bacteria has been used in a wide range of studies, providing insights on bacterial distribution on surfaces, cellular dimensions [119], cell division [120], and surface effects on bacterial adhesion [121].

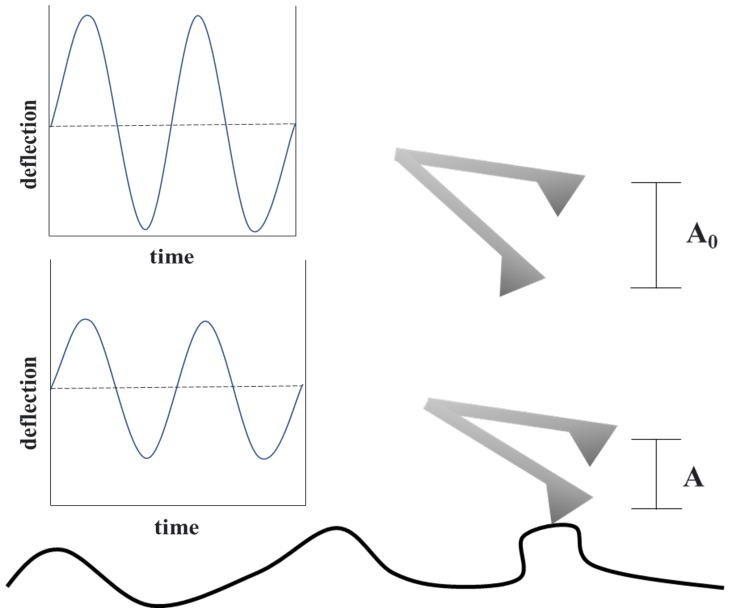

Figure 1.11: Diagram showing the principle of tapping mode imaging. The cantilever is made to oscillate at its resonant frequency, with an amplitude of A_0. As the cantilever nears the surfaces the amplitude of the oscillation is reduced to A

Force mode

Aside from the use of scanning force microscopy (SFM) in capturing detailed images, it can also be employed to obtain force information in force spectroscopy experiments. A force-distance curve is generated, representing the force experienced by the cantilever in relation to its distance from the probed sample.[122, 123]

Although the SFM is typically operated using cantilevers with sharp tips at the end, tip-

less cantilevers have been used to develop bioprobes [124, 125]. These AFM force studies have been instrumental in advancing our understanding of how cells interact with surfaces [126–128]. Much of this research has focused on characterising the structure and function of surface adhesins [129, 130]. For example, experiments where a single bacterial cell is immobilised on an AFM cantilever, known as single-cell force spectroscopy (SCFS) [131], have enabled mechanistic studies of pili [132]. Another AFM-based method, known as single-molecule force spectroscopy (SMFS), has been developed to study the material properties of purified bioadhesives [133]. This method has helped identify the presence of a DNA and peptide residue polymer brush layer on *Caulobacter crescentus* holdfasts (a type of adhesin) [134]. The identified polymer brush was determined to play a key role in facilitating initial surface-holdfast interactions.

1.4.3 Quartz-crystal microbalance with dissipation monitoring

Quartz crystal microbalance (QCM) is a surface-sensitive, real-time technology typically used to detect mass changes at a surface with nanoscale resolution. These mass changes are used in the analysis and quantification of surface-molecule interactions. Initially used to study thin-film deposition in the gas phase and under vacuum conditions [135], the development of liquid phase experiments allowed for the analysis of viscoelastic layers produced by the deposition of substances such as biomolecules or polymers. The quartz crystal microbalance with dissipation monitoring (QCM-D) captures energy loss in addition to mass changes, providing insight into the viscoelastic properties of the system. This is particularly useful for monitoring viscoelastic layers.[136]

QCM-D is a type of acoustic technology. The technique centers around the oscillation of a thin quartz crystal disk. The crystal sensor has electrodes deposited on each side and is made to resonate using an applied voltage. The resonance frequency, f, is dependent on the thickness, or mass, of the sensor. Therefore, nanoscale changes in mass can be detected by monitoring changes in the resonance frequency, Δf.[137] Piezoelectricity plays a crucial role in QCM-D technology. It is a phenomenon where displacement is proportional to the applied voltage. The crystal is made to oscillate as it is composed of a piezoelectric material, typically quartz, allowing for its excitation.[138]

Günter Sauerbrey identified the relation between frequency and mass in 1959, giving rise to the Sauerbrey relation.[140, 141] The equation states that there is a linear relationship between the change in frequency (Δf) and the change in deposited mass per unit area (Δm_f) on the quartz crystal surface. This relationship is expressed as:

$$\Delta m_f = -C\frac{\Delta f}{n} \tag{1.1}$$

C, the mass sensitivity constant, is determined by the quartz properties, while n represents the harmonic in question. For the Sauerbrey equation to be applicable, multiple conditions must be

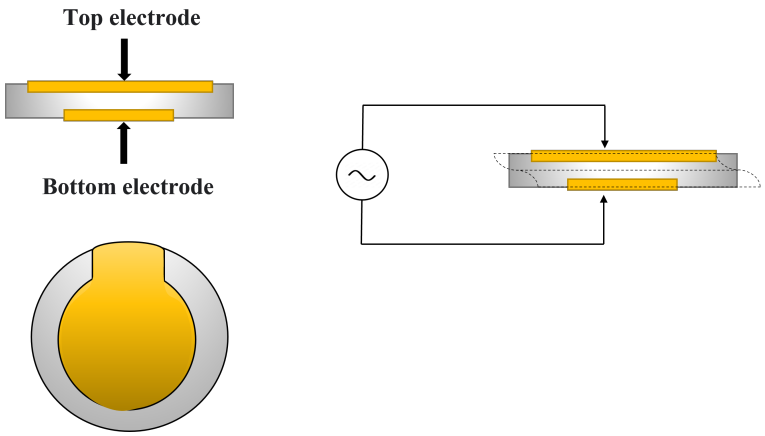

Figure 1.12: Diagram representing the QCM-D oscillating unit which consists of a thin quartz crystal disk with electrodes deposited on both sides. The crystal is excited to resonance with an applied voltage. Changes in the frequency, Δf, are then monitored throughout the experiment. Adapted from reference.[139]

met. The adsorbed mass must be thin, rigid, evenly spread across the sensor, and much smaller than the crystal mass. These limitations necessitate the use of viscoelastic modelling to analyse hydrated systems.[142]

The mass sensitivity constant, C, represents how many nanograms of substance, per cm^2 of the sensor surface, are needed to shift the resonance frequency by 1 Hz. It is dependent on the fundamental resonant frequency of the crystal.[143]

$$C = \frac{\upsilon_q \rho_q}{2 f_0^2} \tag{1.2}$$

The constants υ_q (quartz shear wave velocity), ρ_q (density of quartz), and f_0 (fundamental resonant frequency) are crucial in determining C. Since a smaller C corresponds to higher mass sensitivity, mass sensitivity is better for higher fundamental frequencies.

Dissipation (D) represents the energy loss of the system and indicates how soft or viscoelastic the layer is at the crystal surface. This provides insight into structural changes of the layer, such as swelling, crosslinking, or collapse[144–146]. Dissipation serves as an indicator of whether the Sauerbrey equation can be applied. In cases where the Sauerbrey equation is not applicable, ΔD is used in viscoelastic modelling.[147]

Dissipation is quantified by analysing the damping of the oscillations of the quartz sensor. It is calculated using the resonance frequency (f_r) and the bandwidth of the resonance peak

(Δf). The dissipation factor is given by:

$$D = \frac{1}{2\pi}\frac{\Delta f}{f_r} \tag{1.3}$$

A higher dissipation value indicates a softer, more viscoelastic material, while a lower value suggests a more rigid layer. This measurement helps to evaluate the structural changes in the layer, such as swelling, crosslinking, or collapse.

The QCM crystal is typically made to resonate at a range of different harmonics (n). For the commonly used AT-cut QCM crystals, only the odd harmonics (n=1,3,5,...) can be excited.[148] The overtone order needs to be odd to ensure an antisymmetric motion pattern in the quartz. When the overtone order is even, the deformation becomes symmetric, resulting in no current flow between the electrodes.[148] The lowest resonance frequency ($n = 1$) is called the fundamental, while all higher n values are overtones of the fundamental. Measuring multiple overtones, typically ranging from the 3rd to the 11th, can be measured simultaneously, providing a comprehensive view of the processes occurring at different depths relative to the sensor surface. Higher overtones are particularly sensitive to changes happening near the sensor surface, making them reflective of surface-bound interactions and thin films. In contrast, lower overtones, which penetrate deeper into the sample, are representative of processes occurring further from the sensor surface, capturing bulk material properties and thicker layers.[149, 150] This simultaneous measurement of multiple overtones allows for a nuanced analysis of both surface and bulk phenomena, enhancing the overall understanding of the sample's behaviour. The common exclusion of the fundamental frequency from QCM-D results is due to its significant time-dependent variations.

Measuring a range of harmonics can help determine whether the studied sample falls under the Sauerbrey regime. If the Sauerbrey relationship holds, the adsorbed mass should be derivable using any of the harmonics. Therefore, if the results show very different normalised frequency shifts ($\frac{\Delta f_n}{n}$), the Sauerbrey equation cannot be applied as the film is not rigid. Typically, spread-out harmonics indicate a thick, viscoelastic layer, while rigid, thin layers show harmonics that are close in space. Furthermore, information from multiple overtones is crucial when performing viscoelastic modelling [136].

Methods for modelling the mass of viscoelastic layers have been developed using changes in f and D at a range of harmonics. In addition to the quartz crystal, a viscoelastic layer has its own shear modulus. Viscoelasticity indicates that a material possesses both viscous and elastic responses to applied stress. Models of viscoelasticity attempt to describe the response to stress, which includes both the viscous and elastic components. The Kelvin-Voigt model is one of the most commonly used models for analysing viscoelastic layers. This model was adapted to relate the change in f to layer thickness, density, and viscosity.[147]

The applicability of the Kelvin-Voigt model is limited. If the thickness of the layer exceeds 25% of the crystal oscillation wavelength, the film resonance effect occurs, wherein an increase in mass results in an increase in frequency. Although the Kelvin-Voigt model has been used to determine the thickness of adsorbed layers of various biomolecules such as proteins and enzymes [151–153], its thickness limitation means that it has not been widely used in the study of thick, viscoelastic films, such as bacterial biofilms.[154]

Despite the limitations of both the Sauerbrey and viscoelastic models, many QCM-D investigations have successfully studied bacterial attachment [155, 156]. This has been achieved by analysing the QCM-D results in conjunction with complementary results from additional experiments, such as fluorescence microscopy [157], crystal violet biomass estimation [158], AFM imaging, or force spectroscopy [158, 159]. QCM-D studies focusing on bacteria typically do not extract mass or thickness information directly from the f or D data. Instead, changes in f and viscoelasticity, alongside other data (e.g., microscopy), have been used to indicate changes in processes including the onset of attachment [157, 160], detachment [161, 162], or alteration of the mode of attachment [163]. These studies have explored the effects of various factors that affect bacterial adhesion to different substrates, including the effects of ionic strength [157, 163], cell and surface hydrophobicity [160], and the presence of EPS.[164–166] For example it has been found in one study that Δf does not directly correlate with the number of adhering bacteria; rather, the QCM-D output parameters are determined by the thickness of the interfacial region, which is influenced by the length of the surface appendages. Furthermore, positive frequency shifts occur when the bacterial cell body is not in direct contact with the crystal sensor surface but is maintained at a distance, depending on the length of the surface appendages. Such positive shifts contradict the expected outcome of mass addition on the sensor surface, leading to a significant challenge when modelling bacteria with QCM-D.[167]

Some studies have employed the $\Delta D/\Delta f$ ratio to understand bacterial adhesion and biofilm development processes.[165, 168–170] This ratio is an effective indicator of the viscoelastic properties of the adhered bacteria or biofilm. One study used the $\Delta D/\Delta f$ ratio to examine biofilm architecture and distinguish between two separate biofilm formation phases. When used alongside other QCM-D outputs, this ratio can identify highly sensitive phenomena, such as conformational shifts and the reorganisation of bacterial cells or biofilms.[162, 169, 171]

1.4.4 Research aims

The QCM-D presents an ideal platform for studying bacterial adhesion and biofilm formation due to its capacity for real-time monitoring and large sampling areas. Unlike many commonly used techniques that are invasive, involving mechanical forces, infrared radiation, conductive coatings, exposure to vacuums, or requiring optically transparent substrates and dedicated flow

cells, QCM-D is minimally invasive and label-free. This non-invasive nature is crucial as invasive methods can alter the natural adhesion properties of cells. Additionally, QCM-D allows for easy tuning of various physicochemical parameters such as temperature, pH, and ionic strength during measurements, which is essential given that bacterial adhesion is influenced by surface free energy, wettability, surface charge and surface roughness.[172]

Furthermore, QCM-D's sensitivity enables it to detect not only contact dynamics but also mechanical changes within the bacterial-medium overlayer on the sensor surface, providing comprehensive 3D insights into the system.[157] The importance of monitoring bacterial adhesion in real-time is underscored by the fact that bacterial adhesion and biofilm formation involve time-dependent events that are key to understanding their mechanisms.

Moreover, studying adhesion at the cell population level is vital for understanding interactions such as cell–cell communication and social cooperativity effects.[173, 174] The dynamic and complex process of bacterial adhesion is further complicated by the influence of EPS, which have been shown to affect adhesion mechanisms in EPS-producing bacteria compared to non-EPS-producing bacteria. Variations in the viscoelastic properties of the bacterial-substrate interface, particularly during the dynamic evolution of EPS stages in biofilm maturation and dispersal, also play a significant role.

QCM-D stands out as a powerful tool in the study of bacterial colonisation, providing the necessary capabilities to observe and control the various factors involved in this intricate process. Despite the advances in using QCM-D for studying bacterial adhesion, several critical aspects remain under-explored. To date, most dynamic studies, including those using QCM-D, focus primarily on short-term initial adhesion, lasting less than a couple of hours.[157, 166, 168, 175] This limited timeframe restricts the visualisation to short-term interaction patterns and neglects the long-term processes such as the formation of extracellular polymeric substances (EPS) and biofilm development, which are crucial for understanding bacterial proliferation on surfaces.

Additionally, these short-term studies often overlook bacterial multiplication, which can begin as early as 20 minutes after initial adhesion. Ignoring this aspect means missing significant data on bacterial growth and biofilm maturation over extended periods. Moreover, the majority of these studies are conducted in pure buffer solution[161, 170] to eliminate the effects of complex media and focus solely on pure cell-material interactions. However, this approach over prolonged periods does not accurately reflect real-world conditions, as bacteria are under extreme stress under nutrient-free conditions[13] unlike in most laboratory and natural environments.

Furthermore, QCM-D has not been extensively used to explore several other vital factors. The effects of different temperatures on bacterial adhesion and growth, the impact of quorum sensing inhibitors on biofilm formation, and comparisons between bacteria and colloids with

similar parameters to contrast the results remain largely largely unexplored. Addressing these gaps is essential for a more comprehensive understanding of bacterial behaviour in various environments, and it underscores the need for long-term studies that can capture the full spectrum of bacterial interactions and their implications.

In this study, a label-free QCM-D-based approach is used to discriminate bacterial adhesion profiles and viscoelastic fingerprints at a strain-specific level. Gold is the surface of choice for all experiments due to its dual advantages: research has identified a water contact angle of 65 $\pm$ 5° as optimal for cell adhesion on biomaterials, which matches the water contact angle of pure gold.[176] Additionally, gold's biocompatibility makes it suitable for implants and prosthetic parts, such as screws, due to its established safety and efficacy in medical applications.[177]

The primary bacteria of interest in this study are *S. aureus* and *P. aeruginosa*, representing the unique surface properties of Gram-positive and Gram-negative bacteria, respectively. A range of media with varying nutrient concentrations, more reflective of common laboratory conditions, will be used to determine if QCM-D experiments can be conducted in nutrient-containing media rather than sterile, nutrient-less PBS. This approach aims to provide more realistic insights into biofilm formation.

The overall aim is to enhance our understanding of biofilms and how they are influenced by various factors such as temperature, nutrient conditions, and the presence of quorum sensing inhibitors. Ultimately, the goal is to explore QCM-D as a method of monitoring biofilms to inform prevention and removal strategies in the long term.

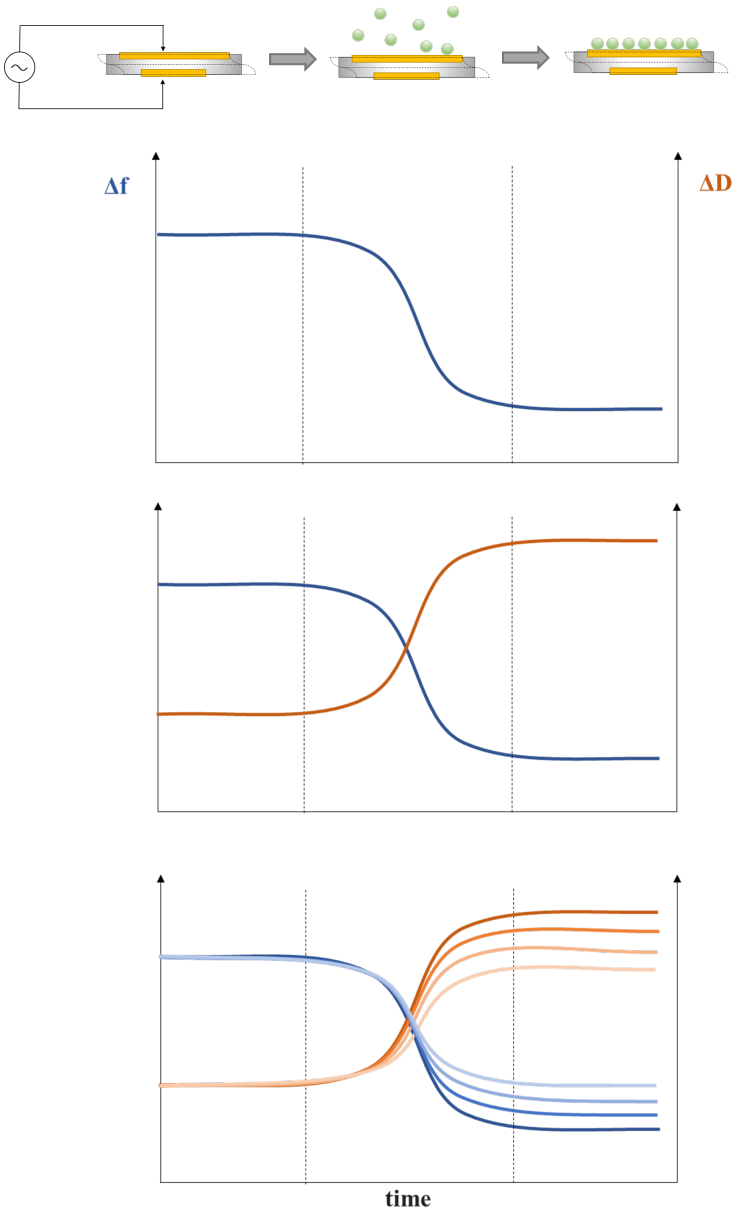

Figure 1.13: A schematic showing model QCM-D experiment results. The top diagram shows the Δf response. As material deposits on the crystal, the frequency becomes more negative. The diagram below includes a model ΔD response, which shows an increase as mass is deposited, representing an increase in viscoelasticity. The bottom diagram shows the results for multiple overtones. Initially, when little material is on the crystal surface, all the overtones overlap, which indicates that the viscoelastic response is insignificant. As the film thickness increases, the overtones separate.

Chapter 2

Experimental methods

2.1 Microbiology

The focal point of this research project lies in the utilisation of QCM-D analysis to explore bacterial colonisation of a gold surface across various nutrient environments. This investigation is complemented by a series of additional experiments encompassing crystal violet assays, fluorescence microscopy, and atomic force microscopy imaging, all designed to gather data on biomass and bacterial coverage. To ensure comparability, these supplementary experiments strive to closely replicate the conditions established in QCM-D studies, following a standardised bacterial attachment protocol outlined herein. The initial growth conditions for bacteria remain consistent across both QCM-D investigations and supporting experiments.

P. aeruginosa (American Type Culture Collection (ATCC) 15442™) and *S. aureus* (ATCC 6538™) were the main bacteria studied in this project. Furthermore, tests were also conducted with a fluorescently labelled *S. aureus* strain (SH1000-GFP), selected for its suitability for fluorescent microscopy.

2.1.1 General protocol for bacterial growth

OD600, or “Optical Density at 600 nm" is a crucial parameter in microbiology for assessing the density of microorganisms in liquid cultures. The term “OD" denotes optical density, reflecting the degree of light absorption or scattering by a solution, while “600" signifies the specific wavelength of light employed for measurement. As bacterial populations proliferate in liquid media, they contribute to increased turbidity or cloudiness due to the scattering and absorption of light by bacterial cells. Consequently, OD600 serves as a widely adopted relative measure of bacterial density in liquid cultures[160, 178] and was utilised as an indicator of bacterial quantities employed in the experiments.

Bacteria were kept as glycerol stocks at -80 °C. The bacteria were streaked on tryptic soy

agar (TSA) plates and incubated (≈ 16 h, 37 °C). The streak plates were kept at -4 °C for up to a week. Single colonies from the plates were used to inoculate 3 mL of TSB (Table 2.1) under continuous shaking (200 rpm). To ensure consistency across experiments, overnight cultures were adjusted to predefined OD600 values (1, 0.5, or 0.1) using the same media employed during the initial growth phase, thereby standardising bacterial concentrations utilised in each experiment. TSB was used as it is one of the most ubiquitous laboratory growth media. Tryptone provides the nitrogen source and peptides necessary for protein synthesis. Soytone, derived from soy peptone, supplies essential vitamins and growth factors. Dextrose serves as the primary carbon source, promoting robust bacterial metabolism. Sodium chloride helps maintain osmotic balance, while dipotassium phosphate acts as a buffering agent to stabilise the pH. TSB is nutrient-rich medium used for cultivating a wide range of bacteria, making it a good candidate for investigating bacterial growth and adhesion.

Component	**Concentration** (g/L)
Tryptone	7
Soytone	3
NaCl	5
K_2HPO_4	2.5
Dextrose	2.5

Table 2.1: Composition of TSB.

In experiments involving the suspension of bacteria in a low-nutrient environment, bacteria were first grown in TSB as described above. They were then centrifuged (4700 rpm, 5 min, 4°C) and dispersed to a chosen OD600 value in Reasoner's 2A broth (R2A) broth (Table 2.2). In R2A broth, peptone provides the nitrogen source, while yeast extract supplies essential vitamins and growth factors. Dextrose serves as the carbon source, and magnesium sulfate along with potassium phosphate helps maintain osmotic pressure. Starch acts as a detoxifier, and sodium pyruvate enhances the recovery of stressed cells. This composition makes R2A broth suitable for studying bacterial behaviour under low-nutrient conditions.

Component	**Concentration** (g/L)
Yeast extract	0.5
Meat peptone	0.5
Casamino acid	0.5
Glucose	0.5
Starch	0.5
Sodium pyruvate	0.3
K_2HPO_4	0.3
$MgSO_4$	0.05

Table 2.2: Composition of R2A.

For experiments involving the suspension of bacteria in a virtually nutrient-free environment, bacteria were first grown in TSB as described above. They were then centrifuged (4700 rpm, 5 min, 4°C) and dispersed in phosphate-buffered saline (PBS) (Table 2.3) to a chosen OD600 value.

Component	**Concentration** (g/L)
NaCl	8
KCl	0.2
Na_2HPO_4	1.44
K_2HPO_4	0.24

Table 2.3: Composition of PBS.

Both of the bacterial growth media and the PBS buffer were created by dissolving the amounts described in the tables above in 1 L of MiLli-Q water and sterilised by autoclaving. All chemicals were acquired from Sigma-Aldrich (Gillingham, United Kingdom).

GFP-labelled *S. aureus* was used in experiments focused on optical visualisation of cells. To ensure that only the bacteria containing the desired genetic modifications survive and proliferate, a selection marker is added to the growth media. This means only bacteria with the genetic construct of interest (in this case, the GFP gene) and the accompanying tetracycline resistance gene will thrive in the presence of tetracycline, an antibiotic. It serves as a method to select for and maintain bacteria that have successfully incorporated the GFP gene. Tetracycline (2 μg/mL) was therefore added to both the agar and broths in all experiments involving the use of GFP-labelled *S. aureus*.

2.1.2 Gold Substrate Colonisation Protocol

In addition to QCM-D data collection, fluorescence imaging and crystal violet assays were conducted to gather biomass and surface coverage data. These experiments were performed in well plates, with experimental parameters carefully tailored to mimic those of QCM-D experiments. The utilisation of well plates enabled the simultaneous execution of a higher number of experiments. The sample preparation procedures remained consistent for both AFM and fluorescence microscopy imaging. Bacterial cultures were prepared according to the protocol outlined previously, to obtain bacterial suspensions of specific OD600 values (0.1, 0.5, and 1). Au-coated quartz sensors, employed in QCM-D experiments throughout this project, served as the substrate of choice to facilitate direct comparison with QCM-D data. The experiments were conducted in 24-well plates, which share the same dimensions as the QCM-D chamber, ensuring identical volumes were used across all of the experiments.

A sterilised crystal was placed into a well, followed by the addition of 500 μL of TSB, and incubated at 25 °C for 10 minutes. This step replicated the media-only 'background' process

carried out at the commencement of each QCM-D experiment. Subsequently, the crystal was transferred to a sanitised chamber and immersed in 500 μL of bacterial culture. The samples were then incubated at 25 °C for 24 hours to obtain AFM images, aligning with the duration of the QCM-D experiments. Conversely, fluorescence microscopy imaging was conducted over a shorter duration of 30 minutes. This abbreviated timeframe enabled the examination of cell distribution on the surface without significant bacterial multiplication on the substrate, facilitating the investigation of attachment behaviour rather than bacterial proliferation on gold. After the incubation period, the crystals underwent gentle washing in PBS ($\times$ 3). Subsequently, the crystals were either mounted on glass slides for fluorescence imaging or fixed for AFM tapping mode imaging.

Cell-fixing protocol

Prior to tapping mode AFM imaging, samples were fixed using 4% paraformaldehyde (PFA) in PBS. All procedures involving PFA were conducted within a fume hood. After the samples were obtained using the method outlined in Section 2.1.2, samples were submerged in 200 μL of 4% PFA in a clean well. The samples were then incubated at room tmperature (RT) for 30 minutes. Subsequently, the crystals underwent washing in PBS ($\times$ 3) and were stored in PBS at -4 °C. Before AFM tapping mode imaging, the samples were dried under nitrogen flow.

2.1.3 Crystal violet assay

A straightforward approach to assessing bacterial biomass is the use of the crystal violet stain. It works by staining the nuclei of adherent cells, working as a intercalating dye. This allows for the quantification of DNA, which is proportional to the number of cells, by measuring the OD of the resulting suspension of stained cells. Bacteria attachment to a gold-coated crystal was described in section 2.1.2. The rinsed crystal were then immersed in 0.5 % crystal violet stain for 20 min at RT on a bench rocker (20 rpm). The crystals were then washed in PBS ($\times$ 3) to remove all excess dye and left to air dry for 24 h. Next, the crystals were immersed in 1 mL glacial acetic acid (30 %) in a clean well, and incubated for 20 min at RT on a bench rocker (20 rpm) to suspend the surface attached cells. The resulting suspension was added to a cuvette and the OD is measured at 595 nm.

2.1.4 Quorum sensing inhibition experiments

Both QCM-D and fluorescence imaging experiments were conducted to probe the effects of a known *S. aureus* quorum sensing inhibitor, savirin. GFP-labelled *S. aureus* was used in all experiments, due to its fluorescent properties, which make for facile sample imaging. All experimental protocols were unchanged, apart from the addition of savirin to a concentration of 5

μg/mL, which was added to the bacterial culture after its dilution to a chosen OD600 value. The bacterial suspension was then used in the same way as in other experiments, i.e. incubated on gold substrate which was then imaged (Section 2.1.2), or used in a QCM-D experiment (Section 2.2.1).

2.2 Measurement gathering and equipment

The key measurements contained in this project involved the monitoring of bacterial attachment using QCM-D and imaging of attached bacteria using tapping mode AFM and fluorescence microscopy.

2.2.1 Quartz crystal microbalance with dissipation monitoring

AT-cut quartz crystals (open QCM, Novaetech) with a fundamental frequency of 5 MHz were used in all QCM experiments. The electrodes consisted of a 200 nm layer of gold deposited on a 10 nm titanium substrate, with an electrode diameter of 12 mm.

Quartz-crystal cleaning procedure

The cleaning procedure for the crystals began with UV/ozone treatment lasting 10 minutes. Subsequently, a solution consisting of Milli-Q water, ammonia (25%), and hydrogen peroxide (30%) in a ratio of 5:1:1 was heated to 75°C in a fume hood. The sensor was immersed in the solution, maintaining the temperature for 15 minutes. After removal from the solution, the sensor was promptly rinsed with Milli-Q water, followed by blow-drying with nitrogen gas and an additional UV/ozone treatment lasting 10 minutes. The sensors were utilised in experiments within 2 hours of completing this cleaning protocol.

Protocol for QCM-D use in the monitoring bacterial attachment

QCM experiments were conducted using the Q-Sense D300 (QSense, Biolin Scientific) system, alongside the acquisition software QSoft 301 and the analysis software QTools. The cleaning procedure commenced by inserting a designated cleaning sensor crystal into the chamber. A solution of 2% sodium dodecyl sulfate (SDS) was then circulated through the loop and chamber, with 30 mL passed through each. The system temperature was elevated to 40 °C, and the SDS solution to was left in the chamber for 30 minutes to enhance the cleaning process. This was followed by flushing with deionised (DI) water (40 mL $\times$ 2), ethanol (30 mL $\times$ 2), and finally DI water (10 mL $\times$ 2). Residual DI water was expelled from the system using nitrogen gas flow, after which the cleaning crystal was removed, and the chamber area was dried. This cleaning

protocol was conducted both before and after each experiment.

Three distinct types of QCM-D experiments were conducted. The initial set of conditions investigated a high-nutrient environment, wherein bacteria were cultured in TSB and adjusted to an OD600 value of 0.5 using TSB. Subsequent experiments explored lower-nutrient conditions, where bacteria were cultured under identical conditions in TSB broth, then centrifuged and re-suspended in R2A to attain the same OD600 value of 0.5. Finally, experiments were carried out under no-nutrient conditions, whereby bacteria were initially cultured in TSB, centrifuged, and subsequently resuspended in PBS to also achieve an OD600 value of 0.5.

Following cleaning, crystals were inserted into the QCM-D chamber, with the temperature set to 25 °C. Frequency and energy dissipation signals were allowed to stabilize in PBS for 10 minutes to establish a baseline. In experiments involving bacteria suspended in growth media (R2A or TSB), PBS was replaced with the respective growth media for an additional 10 minutes (this step was omitted for PBS experiments). Subsequently, PBS/R2A/TSB media were exchanged for a suspension of cells in the respective media, allowing interaction with the sensor surface in stagnant liquid for 24 hours at 25 °C. Continuous monitoring of frequency shift (Δf) and dissipation (ΔD) was conducted by applying an alternating voltage across the quartz crystal and analyzing the resulting oscillation. Data collection was performed at a room temperature of 19 ± 0.5 °C. Measurements included the 3rd, 5th, and 7th overtones to account for variations in penetration depths, as different overtones have distinct depth penetration capabilities.[167] For example, for a 5 MHz shear wave (fundamental mode) propagating in an aqueous medium, the penetration depth is approximately 250 nm. Since the changes in resonance frequencies are proportional to the overtone number the frequency and dissipation changes are normalised to their respective harmonics ($\Delta fn/n$). Data analysis was conducted using OriginPro 2022 (OriginLab).

2.2.2 Tapping mode atomic force microscopy

Bacteria adhered to a gold substrate following QCM-D experiements were visualised using a Molecular Force Probe 3D system (MFP-3D, Asylum Research, Santa Barbara, USA). Tapping mode in air was opted for due to its capability to reduce vertical forces and eliminate lateral forces associated with the technique, thereby safeguarding the integrity of the sample. MLCT-BIO-DC probes (Bruker AFM Probes, Camarillo, USA) were employed. The cantilever specifications provided by the manufacturer include a resonant frequency of 22 kHz, a spring constant of 0.07 N/m, a length of 175 μm, and a width of 22 µm. Manual tuning of the cantilever approximated the resonant frequency to be ≈ 20 kHz. Scanning at a frequency of 0.5 Hz facilitated the acquisition of images spanning 10 μm × 10 μm.

2.2.3 Fluorescence microscopy

Fluorescence microscopy was conducted on GFP-labelled *S. aureus* on Au-coated crystals employed in QCM-D experiments as substrates. The experimental conditions were designed to mirror those of the QCM-D experiments, with the crystals incubated in plastic wells of identical dimensions to the QCM-D chamber. Uniform volumes (0.5 mL) and a constant temperature (T = 25 °C) were maintained, akin to the QCM-D setup. Following the designated incubation period, the crystals underwent washing and drying under nitrogen. Subsequently, 20 µL of PBS was added to each sample of GFP-labelled *S. aureus* attached to the crystal using PBS, and the samples were sealed with a microscope glass cover slip. Imaging was performed on a Zeiss (Oberkochen, Germany) LSM880 AiryScan confocal microscope equipped with a 63× objective. Initially, samples were located using the epi-fluorescence setting. An argon laser excited the GFP at 488 nm, with detection limited to emission wavelengths ranging between 497 nm and 540 nm. Various image sizes were acquired for each sample: 225 µm × 225 µm, 135 µm × 135 µm, 50 µm × 50 µm, and 25 µm × 25 µm.

Chapter 3

Investigating bacterial colonisation of gold surfaces using QCM-D

This chapter explores the study of bacterial colonisation on gold surfaces. The technique of QCM-D, known for its detailed insights into bacterial attachment in buffer solutions, is fundamental to this research. The QCM-D crystal's total area is considerably larger than the areas usually examined by microscopy, offering extensive sampling and a thorough understanding of bacterial colonisation across a wider area. Gold is chosen for its common use in scientific studies, primarily due to the basic van der Waals forces that predominantly influence its interactions with bacteria.[162, 168] The central focus of this research is to assess the efficacy of QCM-D as a tool for long-term biofilm studies. Initially, the study assesses the effectiveness of QCM-D in analysing bacteria in nutrient-rich environments that promote strong biofilm development, leading to quick colonisation and biofilm creation. After confirming this method's effectiveness, the research shifts focus to the colonisation dynamics between two prevalent pathogens—*S. aureus* and *P. aeruginosa*, examining the effects of different temperatures, comparing strains of *S. aureus*, and analysing the impact of quorum sensing inhibition (QSI) on *S. aureus*. The QCM-D findings are supported by additional experiments, including crystal violet biomass assays and fluorescent microscopy of labeled cells. An OD600 of 0.5 is maintained for all experiments unless specified otherwise. In all QCM-D experiments, sensor signals are initially stabilised in pure media before introducing the bacterial inoculum. Consistent with typical research practices, the exclusion of the first overtone (fundamental) is due to its significant time-dependent variations. Furthermore, the middle, 5th overtone, is selected as the representative signal for some comparative analyses for clarity.

3.1 The viscoelastic and adhesive characteristics of *S. aureus*

This section examines the potential of using QCM-D to study the interactions between the bacterial species *S. aureus* and a gold surface. Known for its robustness and resistance to antibiotics, *S. aureus* is recognised by its spherical form[179]. As a Gram-positive bacterium, it possesses a

thick peptidoglycan layer[180]. It flourishes in various environments but is especially adept at colonising human skin and mucous membranes, making it a common opportunistic pathogen and a key subject of research[181]. *S. aureus* uses surface adhesins, particularly microbial surface components recognising adhesive matrix molecules (MSCRAMMs), to attach to host tissues and inanimate surfaces[182]. These adhesins are critical during the initial attachment phase and subsequently facilitate biofilm formation by promoting the aggregation of bacterial cells into stable communities.[183]

Initially, an experiment with *S. aureus* in PBS buffer was performed to verify the detectability of surface interactions under rudimentary, nutrient-poor conditions. Further experiments were planned to explore the dynamics of these interactions in different environmental settings. The expected results are intended to illuminate the viscoelastic characteristics of bacterial biofilms and clarify their adhesion strategies, crucial for comprehending biofilm formation processes.

3.1.1 QCM-D monitoring of *S. aureus*

Phosphate buffered saline (PBS) closely mimics the ionic composition and pH of physiological fluids, making it suitable for studying biological interactions such as protein adsorption, biomolecular interactions, or cell-surface interactions. As PBS comprises dissolved salts only, the interaction of the buffer with the QCM-D sensor is minimal, allowing for the changes in the Δf and ΔD signals to arise solely due to bacterial interaction with the surface.

Figs 3.1a and 3.1b show the time-dependent frequency, Δf, and dissipation, ΔD, shifts resulting from the interaction of *S. aureus* with a gold-coated QCM-D surface for a period of 24 h. The medium is 1 × PBS (162.7 mM ionic strength, pH pf 7.4). The Δf of the 3rd overtone decreased to -22.8 Hz as a result of cell interactions with the surface. This decrease in Δf is also observed for the 5th and 7th overtones, which reach lower values of -27.0 and -28.2 Hz, respectively. The cell suspension is introduced into the system following an initial 10 minute PBS-only baseline, as can be seen in the insert which focuses on the first 1 h of the experiment. As the system transitions from flow to non-flow after the cell suspension is introduced, a small partial recovery can be observed prior to the gradual decrease in Δf throughout the experiment. This recovery is seen for all overtones.

The corresponding dissipation increases to 10.6×10^{-6} for the 3rd overtone. All overtones follow the same time-dependent trend, with successively lower values being reached with increasing overtone (3.4×10^{-6} and 2.3×10^{-6} for the 5th and 7th overtone, respectively). An increase in dissipation represents the rising viscoelasticity of the bacterial over-layer on the sensor. The stability of the dissipation signal throughout the experiment after the initial swift increase up to approximately 6.5 h suggests that no major changes in the stiffness of the layer occur within the time frame of the experiment. This is possibly due to a lack of nutrients in the environment,

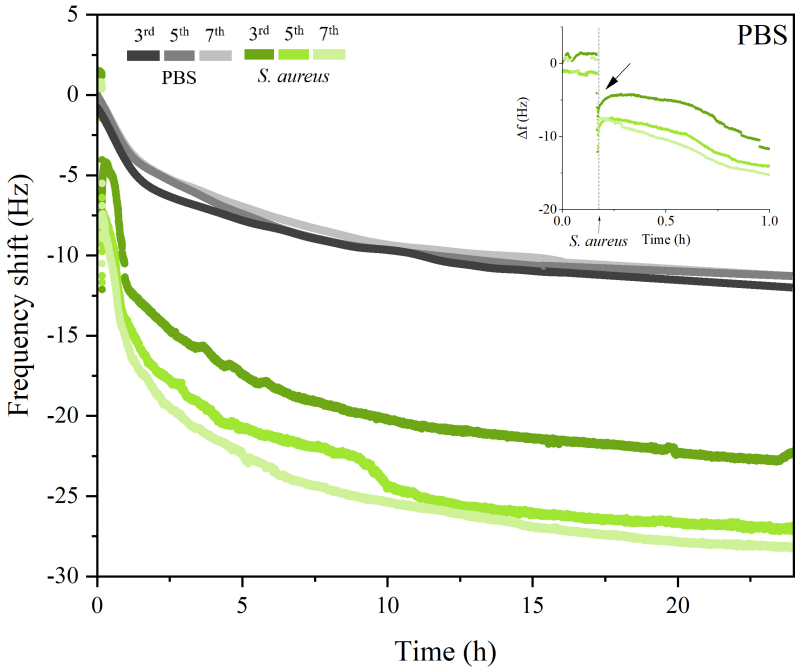

(a) Frequency

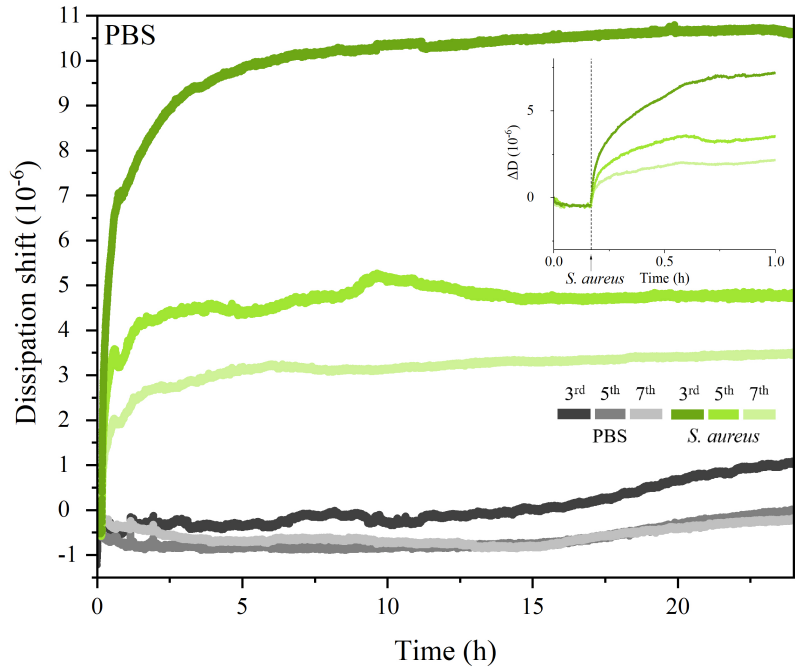

(b) Dissipation

Figure 3.1: Time-dependent frequency, Δf, and dissipation, ΔD, response of gold-coated QCM-D surface to *S. aureus* in PBS buffer. A reference measurement in pure PBS buffer is included.

which is known to prevent cell-surface attachment as well as cell multiplication.[184]

In the reference sample comprising solely of PBS, both the frequency and dissipation signals exhibit relatively minimal changes over the course of the experiment. Nevertheless, there appears to be a gradual drift in the signal, particularly noticeable around the 15-hour mark, wherein the frequency decreases and dissipation increases over time. This may arise due to instrumental factors such as electronic noise, ageing of components, or internal stability issues within the QCM-D instrument itself possibly contributing to the baseline measurement drift. A literature example of PBS on an Au surface suggests that small fluctuations are commonplace, with the Δf drifting by -2 Hz and ΔD exhibiting a slight increase, within the same 24-hour time frame as of the experiments presented here.[170]

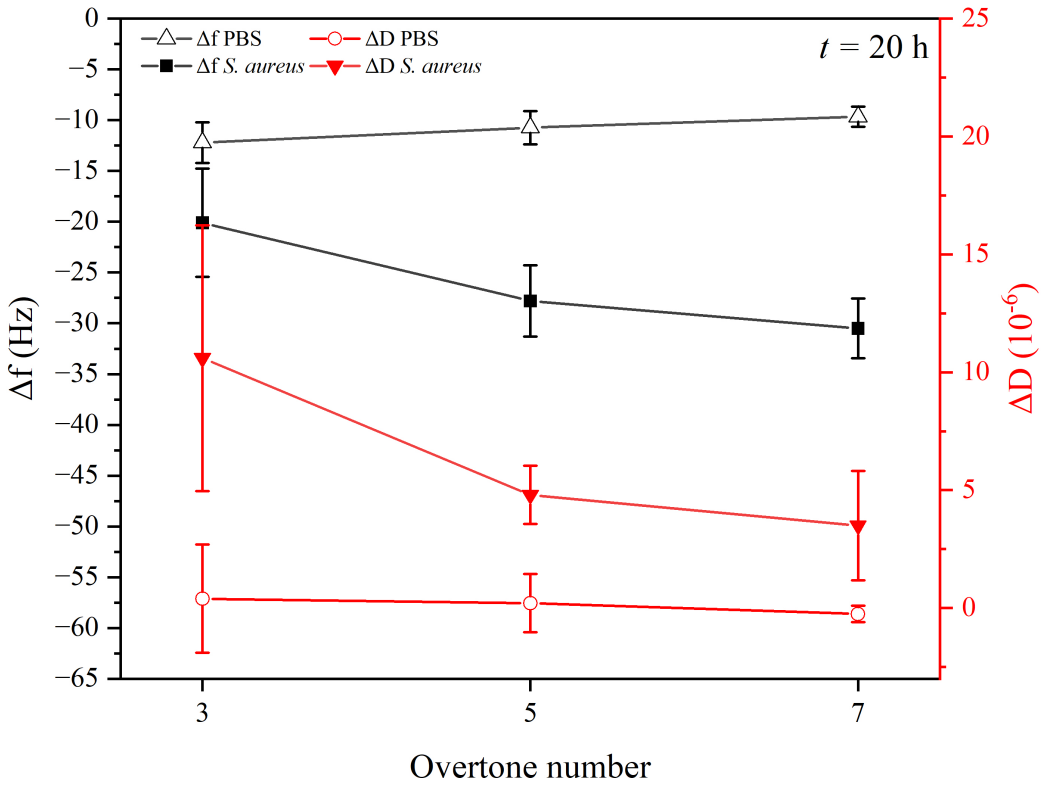

Figure 3.2: Differences in frequency and dissipation at the different overtone numbers for a reference sample (PBS only) and bacterial sample (*S. aureus* in PBS), showing differences for all overtones. The data represent the mean of at least three measurements calculated at the time point t = 20 h. The errors are standard deviations.

Fig. 3.2 presents frequency and dissipation values from various overtones, contrasting the reference sample (1 × PBS only) with the bacterial sample. The data represent the mean of

no fewer than three measurements, derived from raw signals at $t = 20$ h, with error bars indicating standard deviations. This time was chosen due to relative stability of signals at that point. Notably, both frequency and dissipation values across all overtones are markedly elevated compared to those of the reference measurement, indicating that the different signals arise due to bacterial interactions. Moreover, a discernible drift in the magnitude of frequency shifts towards higher values is observed for lower overtones in the bacterial sample. Additionally, lower overtones largely tend to exhibit larger variability, as evidenced by the size of the error bars. This variability may stem from the stronger interaction of these overtones with the liquid medium, attributable to their deeper penetration compared to higher overtones. In summary, the findings suggest that QCM-D shows promise as method for studying long-term bacterial interactions with surfaces. The consistent and reproducible bacterial-surface interactions observed underscore its efficacy as a tool for investigating the dynamics of bacterial adhesion. The next objective is to explore whether this capability can be applied not only to the study of bacterial attachment to gold surfaces, but also to biofilm formation.

All measurements detailed thus far were conducted in pure PBS to mitigate the influence of complex media on cell-material interactions. The presence of complex media may hinder the precise monitoring of cell adhesion behaviour, as the significant contribution of the adsorbed layer of proteins and other substances affects the QCM-D response when medium is present. Many QCM-D studies which focus on long-term cell adhesion therefore involve suspending cells in PBS,[161, 162, 166, 170] or other nutrient-free buffers,[163, 167] to minimise interference from media components. PBS has been shown to preserve some suspended bacteria over long-term storage.[185] However, it is important to recognise that PBS's zero-nutrient conditions induce starvation in bacteria, resulting in decreased viability over time. Moreover, nutrient scarcity can alter bacterial metabolism, leading to changes in the expression of virulence factors in *S. aureus*. This can cause a downregulation of factors involved in surface colonisation and an upregulation of factors promoting survival and persistence, prompting morphological changes that enhance bacterial survival under stressful conditions. It is documented that a significant loss of viability, ranging from 99 to 99.9% of the population within 2 days[184], occurs under glucose and multiple-nutrient limitation. Consequently, a considerable portion of observed interactions will involve dead, stressed, or altered cells, limiting the applicability of PBS being useful in studying bacterial attachment and biofilm formation, unless the aim is to investigate the bacteria under extreme stress conditions. Interestingly, small, protective biofilms of *S. aureus* can form under such nutrient-less conditions, possibly reflecting frequency and dissipation changes observed in the 24-hour experimental data seen in Figs 3.1a and 3.1b. Therefore, it is pertinent and of interest to assess whether the findings remain applicable in more complex media, wherein bacteria are not subjected to stress conditions.

3.1.2 Investigating *S. aureus* colonisation across varied growth media

This section delves into the dynamics of adhesion and biofilm formation of *S. aureus* in three distinct media environments: PBS, Reasoner's 2A (R2A) broth, and tryptic soy broth (TSB). Expanding upon the preceding discussion on *S. aureus* adhesion in PBS, where limited nutrient availability constrains bacterial growth and biofilm formation, the focus now shifts to nutrient-rich conditions to elucidate the impact of media composition on QCM-D signals. The measurements conducted in TSB and R2A necessitate interpretation in the context of bacterial growth on the surface. It's important to acknowledge that the QCM-D data obtained in these buffers will reflect not only adhesion but also bacterial multiplication and exopolysaccharide production, even within the initial hours of the experiments. The objective is to ascertain the utility of QCM-D data under high-nutrient conditions, while bacteria begin forming biofilms, and its potential applicability for subsequent experiments involving variations in other parameters.

Below, the behaviour of bacteria suspended in R2A broth is investigated using QCM-D. R2A broth, a low-nutrient medium, comprises casein peptone, yeast extract, dextrose, and starch, offering a source of amino acids, peptides, vitamins, minerals, and carbohydrates for bacterial growth and metabolism. Unlike the simple composition of PBS, the organic constituents in R2A broth contribute to its greater mass and complexity. Consequently, higher frequency and dissipation signals for an R2A broth baseline measurement compared to pure PBS are anticipated, attributed to the increased adsorption of organic molecules onto the crystal surface over time. A QCM-D literature example using glucose alone[186] shows a frequency shift of -40 Hz reached within 8 minutes for the same glucose concentration (3 mM) as present in R2A. Similarly, a shift of -50 Hz is observed for bovine serum albumin (BSA), a protein often used as a concentration standard, within 25 minutes.[187] However, an example using yeast peptone dextrose medium[162] (a medium used for the cultivation of yeast, consisting of glucose and amino acids) shows a steady decrease to -50 Hz over 24 hours, the same timescale of the experimental results presented here. This suggests that a gradual decrease, rather than a stable line, may be observed in the data, reflecting the continuous adsorption of organic molecules onto the crystal surface throughout the experiment's duration. It is anticipated that PBS will display lower dissipation due to its lack of organic components, whereas the diverse organic compounds in R2A broth should result in a more viscoelastic layer on the crystal surface, resulting in higher dissipation values.

In addition to the variations in QCM-D signals expected due to the differing media, notable differences in the behaviour of *S. aureus* between R2A broth and PBS are also anticipated. Firstly, greater bacterial accumulation on the sensor surface compared to PBS is expected for *S. aureus* suspended in R2A broth. R2A broth provides nutrients, which will deposit on the QCM-D sensor, prompting bacterial attachment, multiplication and biofilm formation. Secondly, variations in bacterial physiology are expected; *S. aureus* in R2A broth is likely to be

actively growing and metabolically active, leading to changes in cell morphology, gene expression, and extracellular polymeric substance (EPS) production. Conversely, nutrient deprivation is likely to be experienced by cells suspended in PBS, potentially impacting cell viability and adhesion properties, with cells predominantly existing as planktonic cells, resulting in differences in Δf signals, as fewer cells interact with the surface. Similarly, more hydrated and viscoelastic biofilms may be produced by *S. aureus* cells in R2A broth compared to those in PBS, resulting in noticeable differences in ΔD signals.

The results of the R2A experiment (Fig. 3.3a) show the 3rd overtone to decrease to -34.3 Hz (n =5: -39.4 Hz, n =7: -40.4 Hz), while the dissipation increases to 11.2 $\times$ 10^{-6} (n =5: 6.9 $\times$ 10^{-6}, n =7: 3.8 10^{-6}). The similarity of results for *S. aureus* in R2A medium to its R2A-only reference measurement for both Δf and ΔD, indicate minimal bacterial interaction with the surface occurs under these conditions. An indicator of the bacterial adsorption occurring is the larger spacing of the overtones for both the Δf and ΔD data, indicating the higher viscoelasticity of the sample. QCM-D baselines can drift due to ambient temperature changes[188], consistent with the simultaneous Δf and ΔD deviation observed here,The peak seen at 10-15 hours is therefore unlikely to be due to a change in the population, but rather a fluctuation in the measurement conditions, such as a temperature variation in the laboratory. This is because both Δf and ΔD change at the exact same time, and population-wide changes, such as multiplication rates, would not result in an increase in mass at the surface. Ultimately, the outcomes closely mirror the baseline. Notably, the final Δf and ΔD values closely resemble those of PBS. This may be because, despite the inclusion of dissolved sugars and other components in R2A media, the nutrient contents may not be adequate to support biofilm development. Consequently, bacteria may resist biofilm formation under these conditions.

Next, QCM-D experiments were conducted on *S. aureus* in TSB. A commonly used medium in laboratory settings for culturing and stimulating bacterial growth, it offers abundant nutrients derived from soybean meal and casein enzymatic digests. It has capacity to support rapid bacterial growth and is suitable for use in a diverse range of microbial populations. Consequently, TSB was selected for the experiment due to its likelihood to promote rapid biofilm formation in all studied bacteria. The TSB-only reference measurement is expected to yield more pronounced shifts in QCM-D signals compared to the R2A baseline. This anticipation stems from its richer nutrient composition, which is likely to result in a greater accumulation of solutes and organic molecules on the crystal surface, leading to more significant changes in frequency over time. Additionally, nutrient profile of TSB is expected to contribute to the formation of a more complex viscoelastic layer on the crystal surface, resulting in higher dissipation values.

While the TSB-only baseline exhibited substantial negative frequency and positive dissipation values indicative of complex surface-medium interactions, the introduction of *S. aureus* resulted in a distinct Δf peak and significantly elevated dissipation values not observed in the

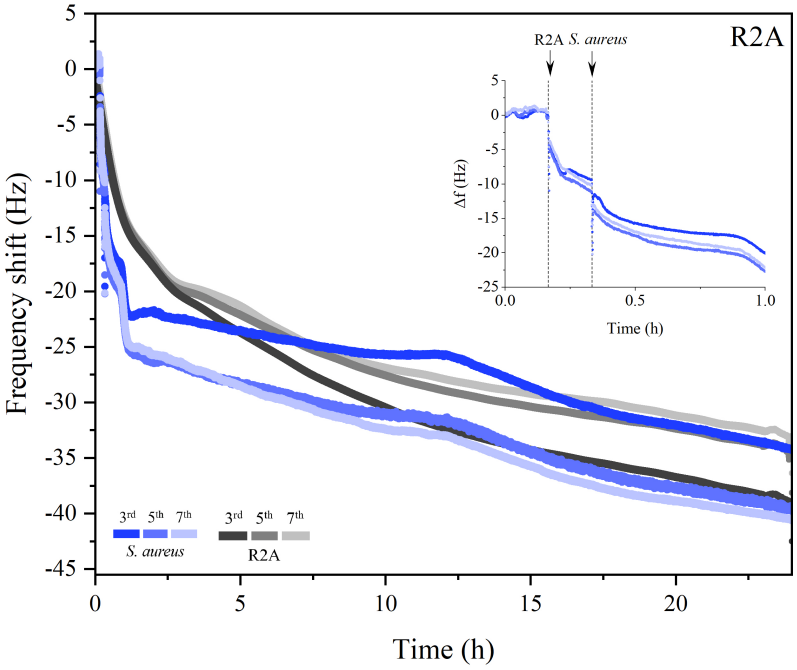

(a) Frequency

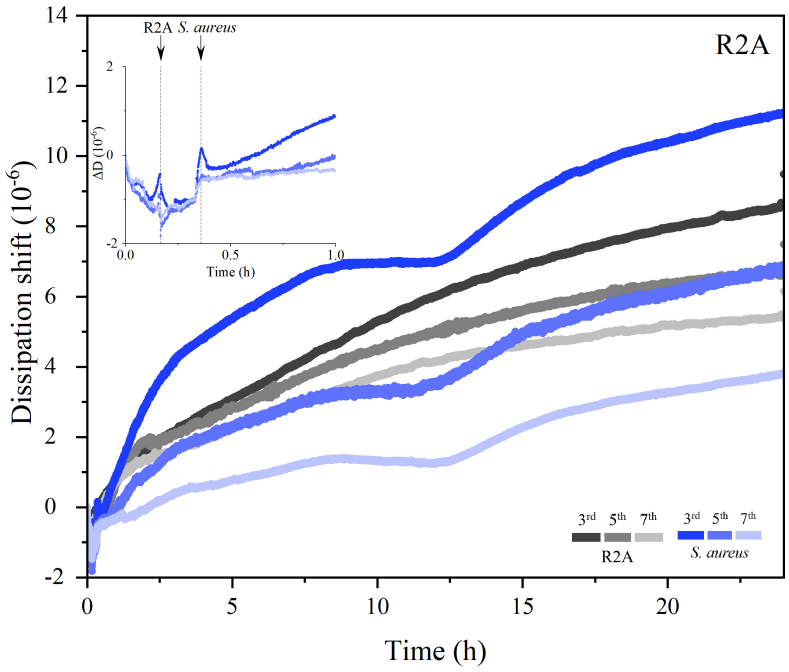

(b) Dissipation

Figure 3.3: Time-dependent frequency, Δf, and dissipation, ΔD, response of gold-coated QCM-D substrate to *S. aureus* suspended in R2A liquid medium. A reference measurement in pure R2A is included.

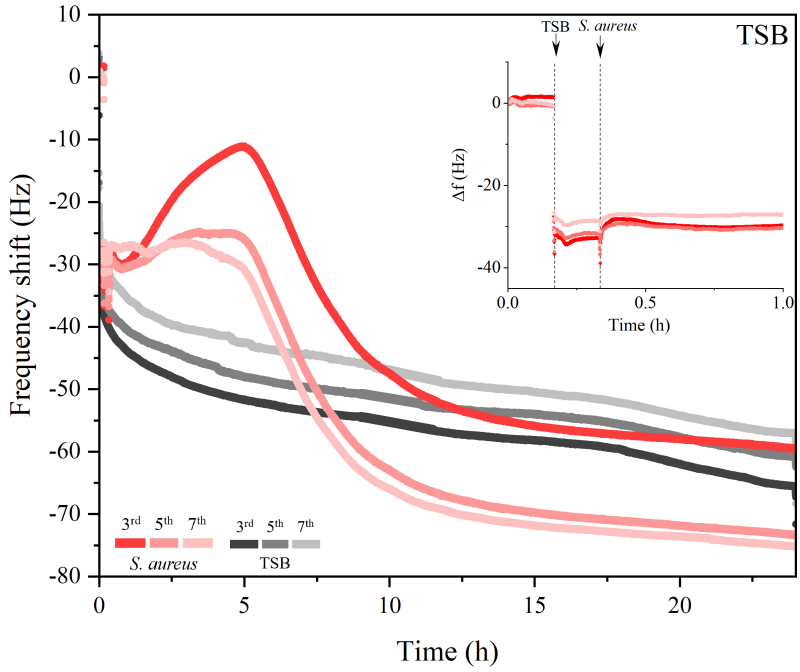

(a) Frequency

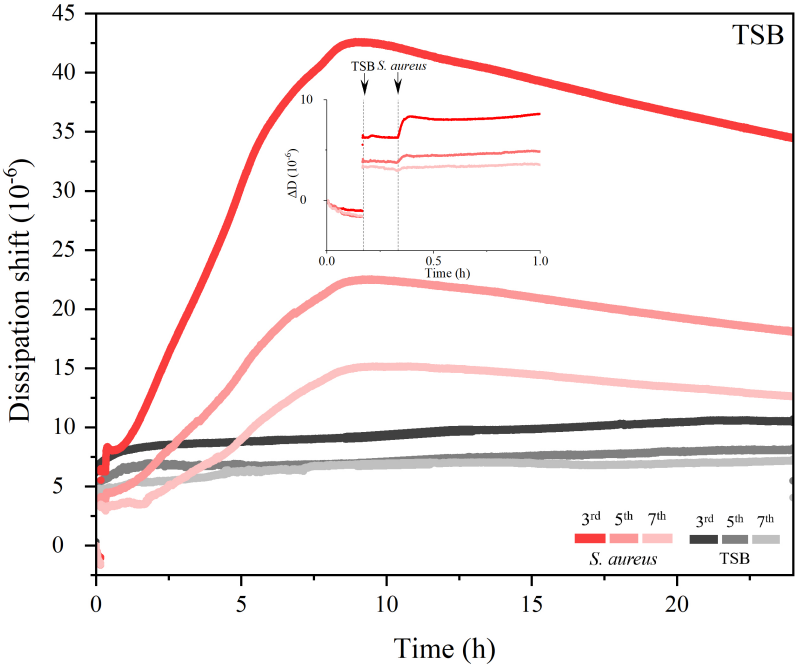

(b) Dissipation

Figure 3.4: Time-dependent frequency, Δf, and dissipation, ΔD, response of gold-coated QCM-D substrate to *S. aureus* in TSB medium. A reference measurement in pure TSB is included.

baseline (Fig. 3.4). The distinguishing features arising from bacterial substrate interactions, absent in the media-only control, indicate the potential of QCM-D in studying bacterial biofilm formation. Mainly, the results seen in Fig. 3.4a show the frequency initially increases, reaching a peak at 4.9 hours, before gradually decreasing to a final value of -59.6 Hz. Concurrently, the dissipation exhibits a similar trend, increasing steadily until reaching a peak at a later time of 8.8 h, followed by a subsequent decrease. This decline in long-term dissipation has been attributed in previous studies to an increase in stiffness, possibly stemming from the reorganisation of the bacterial cytoskeleton and/or restructuring of surface appendages.[175, 189] Such adjustments result in stronger adhesive contact with the substrate, highlighting the dynamic nature of *S. aureus* interactions within the TSB medium environment.

The characteristic positive Δf peak observed at approximately 4 hours in TSB is unusual because it is not accompanied by any corresponding change in dissipation. Under typical conditions, if this peak were caused by the onset of EPS production or cellular reorganisation, an increase in layer stiffness (and thus a change in dissipation) would be expected. The peak likely reflects a temporary increase in effective contact stiffness (weak, oscillatory binding becoming more rigid) rather than a loss of biomass. In one study [163], a similar peak at 3 hours in 100 mM NaCl (with TSB containing 85 mM NaCl) in *P. aeruginosa* was attributed to the oscillation of a soft, thick bacterial layer on the surface, which temporarily counteracted the added inertia. A comparable effect was observed by Pomorska *et al.* [190] on solid micron-sized particles. This coupled resonance effect can produce a positive frequency shift despite additional mass, provided that the interaction with the sensor is initially weak. As bacterial cells transition from weak, reversible interactions to an irreversible bond with the substrate, marked by an increased number of attachment points, a transient rise in Δf is observed, followed by the typical frequency shift progression associated with stronger adhesion [160].

The coupled resonance phenomenon is explored in greater detail in Chapter 4, where the contact stiffness-frequency relationship is presented in Eq. 4.13. In this relationship, the frequency shift is proportional not only to the mass density of the cells but also to the contact stiffness, with both factors contributing to the observed changes in frequency. This relationship indicates that the observed Δf peak represents an early phase during which bacterial interactions with the sensor surface intensify, reaching a maximum at approximately 5 hours, before transitioning into the standard QCM-D mass-frequency dynamics. Similar positive Δf shifts have been reported in several studies [158, 161, 191], typically occurring within the first few hours of an experiment. The presence of proteins, sugars, and other functional groups on the bacterial cell surface permits non-rigid adhesion to the sensor, so that these peaks may signify a stage in biofilm formation where the transition from weak, reversible adhesion to stronger, irreversible attachment takes place. [47, 192]

The formation of the biofilm matrix is a dynamic process influenced by factors such as nu-

trient availability, the synthesis and secretion of extracellular materials, shear stress, and social competition [193, 194]. This process begins with microcolony formation, which enables bacteria to establish stronger and more permanent attachments. As the biofilm matures, EPS production intensifies, and the accumulation of EPS becomes central to the transition from early adhesion to a fully developed biofilm structure [156]. In the TSB experiments with *S. aureus*, the end of the positive Δf regime at approximately 4.9 h may identify the onset of significant polysaccharide production, contributing to the maturation of adhesion bonds. Initially, the weak bonds during early adhesion may result in the observed positive Δf shifts via the coupled resonance effect; as EPS production commences and increases, the bacterial attachment becomes more robust, leading to a sustained frequency decrease in line with the standard QCM-D mass-frequency relationship. Despite an extensive literature search, no studies were found that provide a time-resolved profile of EPS production for *S. aureus* or other bacterial species. Consequently, the proposed 4.9-hour mark as an indicator of EPS production could not be directly correlated with existing data. This gap highlights the need for further research, while also demonstrating the potential of QCM-D as a tool for investigating these processes. This timing aligns with early biofilm maturation; although quantitative EPS measurements for this timeframe are lacking in the literature, it is plausible that polysaccharide synthesis accelerates around 5 h, tipping the system from the 'elastic-dominated' response back to the classical mass-loaded response.

During biofilm formation, the characteristic Δf peak is prominent in the nutrient-rich media, TSB, but is notably absent when bacteria are suspended in basic media like R2A or in PBS. In line with the previous discussion, this peak appears to reflect the transition from weak to strong adhesion, potentially marking the onset or increase in EPS production. In TSB, the abundant nutrients foster heightened metabolic activity and robust quorum sensing, which together prompt a rapid surge in EPS production.[195] Environmental signals and quorum sensing further trigger gene expression changes that modulate biofilm development.[156] Conversely, in R2A and PBS the limited nutrient availability results in slower metabolic rates and more gradual biofilm maturation, thereby precluding the emergence of a distinct sensor response. Overall, the presence of the Δf peak in nutrient-rich conditions underscores the critical role of nutrient availability in modulating bacterial adhesion and EPS production, as evidenced by the QCM-D data.

One literature example of a QCM-D experiment looking at *S. aureus* interaction with the same substrate, Au, and in the same liquid media, TSB, has been found.[196] However, there are major differences between the experimental set-ups. Their experiment uses a modified QCM-D where a series of sensors are immersed into a well-plate. They are immersed vertically into the bacterial suspension, unlike the horizontal set-up of the QCM-D used here. Bacteria are known to preferentially colonise horizontal rather than vertical niches, due to deposition of nutrients on such surfaces.[47] This would suggest the Δf in the literature example should be, comparatively, less negative. However, the volumes used were also much larger (3.8 mL compared with 0.5 mL), and 0.25% glucose was added to TSB, to stimulate biofilm development. Additionally,

the temperature of the QCM-D experiment was not specified, so may also differ, and is known to lead to drastic differences in QCM-D signals[136, 197] as well as in biofilm development.[198] Collectively, these differences are perhaps the reason for the the frequencies reached over the same time-frame to be much more negative (≈-300 Hz compared with ≈ -70 Hz). Additionally, the peak at t =4 observed in the data herein presented is not seen in the literature example. This suggests that the coupled resonance effect only occurs under specific conditions.

In order to validate the robustness of the results across the three media types, the average frequency and dissipation signals were obtained from a minimum of three independent measurements for n = 5 at multiple time points: 30 minutes, 2 hours, 4 hours, 8 hours, 16 hours, and 24 hours. Error bars indicating standard deviations were included to represent data variability. The data from all three media conditions plotted together for comparison can be seen in Fig. 3.5, with only the 5th, middle, overtone included for ease of visualisation. Analysis of these averaged signals reveals a consistent time-dependent profile for *S. aureus* in the different media conditions. This consistency across various time points strengthens the reliability and credibility of the findings, reaffirming the reproducibility of the experimental outcomes. The frequency data reveal that while R2A conditions ultimately yield lower values than PBS at the end of the experiment (maximum of -39.5 Hz compared to PBS at -27.1 Hz), PBS and R2A Δf signal progression and values are similar. Initially, the frequency decreases rapidly for approximately one hour, followed by a gradual decrease. In contrast to the relatively similar PBS and R2A results, TSB demonstrates markedly different bahaviour, with Δf reaching a maximum at 4 hours before declining to -73.4 Hz, a much more negative value compared to the other two media. Notably, since each QCM-D curve was reproduced in at least three independent experiments, the observed Δf peak for *S. aureus* in TSB is a reproducible feature.

Similarly, dissipation results exhibit notable features in TSB, characterised by a markedly higher final value of 18.1×10^{-6} and a significant peak around 9 h, followed by a gradual decrease. Conversely, such bahaviour is not observed in PBS and R2A, where dissipation gradually increases for both media. Specifically, R2A reaches a value of 6.8×10^{-6}, while PBS reaches 3.3×10^{-6}. Interestingly, PBS dissipation shows an initial slight elevation in the first 5 hours. However, a discernible difference emerges between R2A and PBS around the 12-hour mark, where both frequency and dissipation exhibit a slightly accelerated increase in R2A, suggesting a variance in cell interaction and colonisation of the surface between the nutrient-less conditions of PBS and the nutrient-limited environment of R2A. The observed differences may result from R2A conditions providing an environment that supports gradual bacterial colonisation of the surface, whereas the stress-inducing environment of PBS tends to trigger an early, protective colonisation response that does not progress to full biofilm development due to insufficient nutrients.[184]

AFM images of the bacteria layer on the QCM-D sensor were obtained to shed light on the

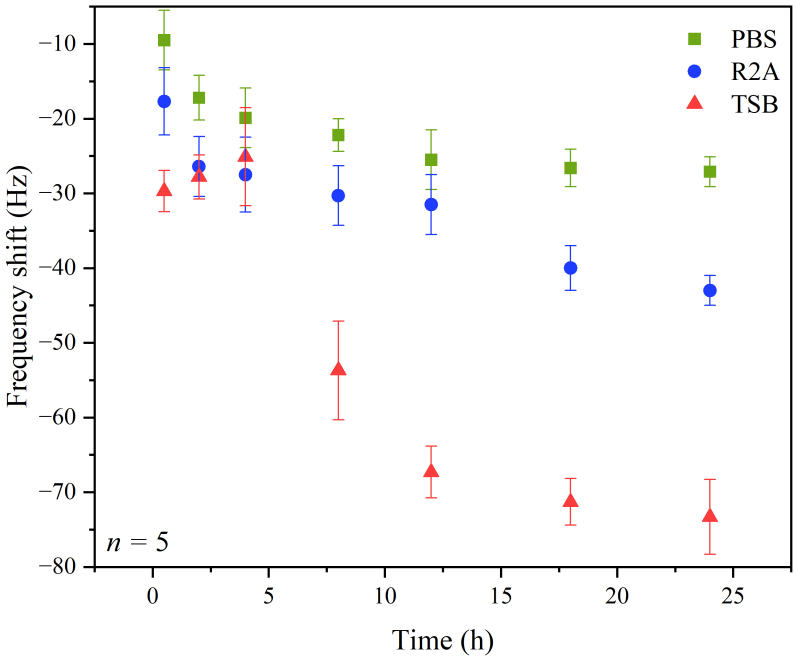

(a) Frequency

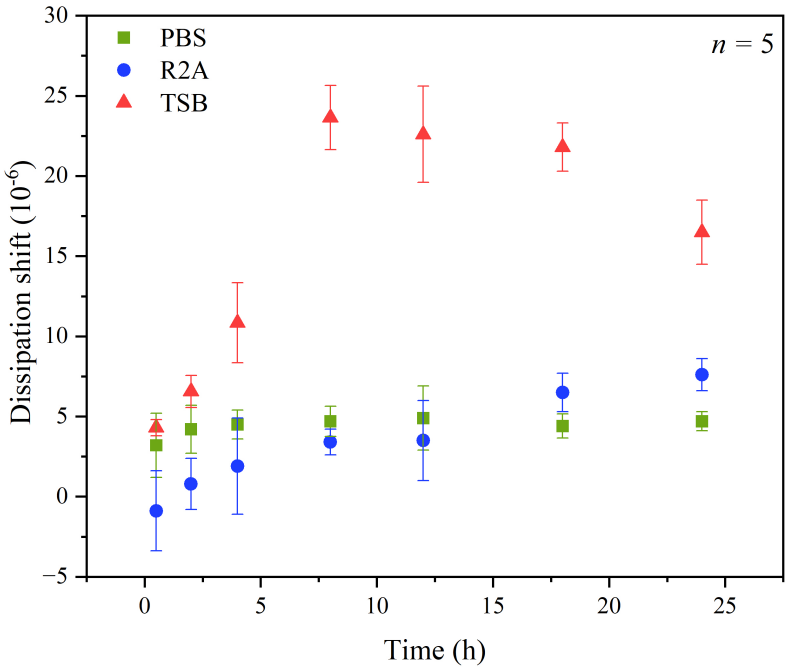

(b) Dissipation

Figure 3.5: Comparison of Δf and ΔD for *S. aureus* in three different growth media displaying emergence of differences over time. The middle, 5th, overtone is chosen for easier visualisation. The data represent the mean of at least three measurements calculated at the time points t = 0.5, 2, 4, 8, 12, 18, 24 h. The errors are standard deviations

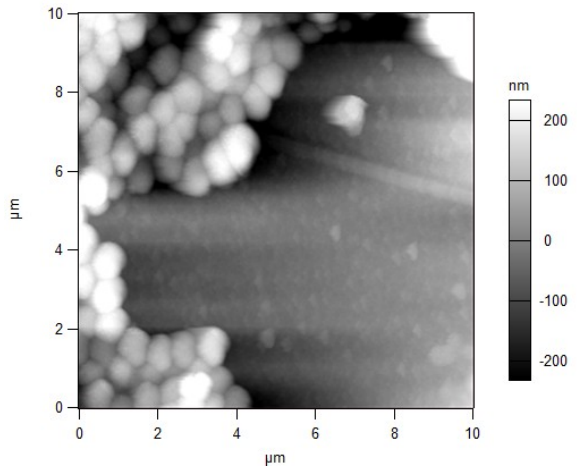

(a) PBS

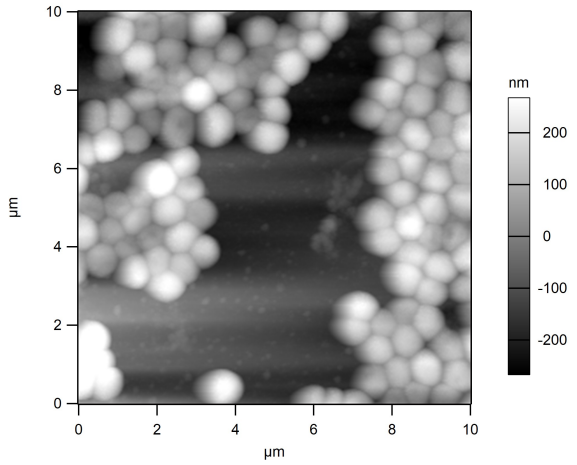

(b) R2A

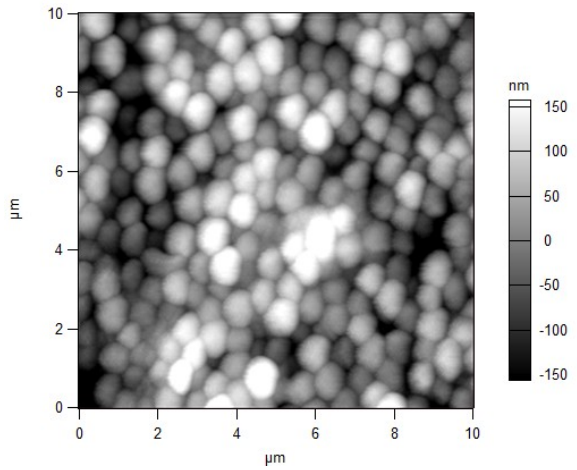

(c) TSB

Figure 3.6: Tapping mode AFM images of Au-coated QCM-D sensor after measurements of *S. aureus* interaction with the surface in three different liquid media, showing the more nutrient dense the media, the higher surface coverage. Bacteria were fixed at $t = 24$ h.

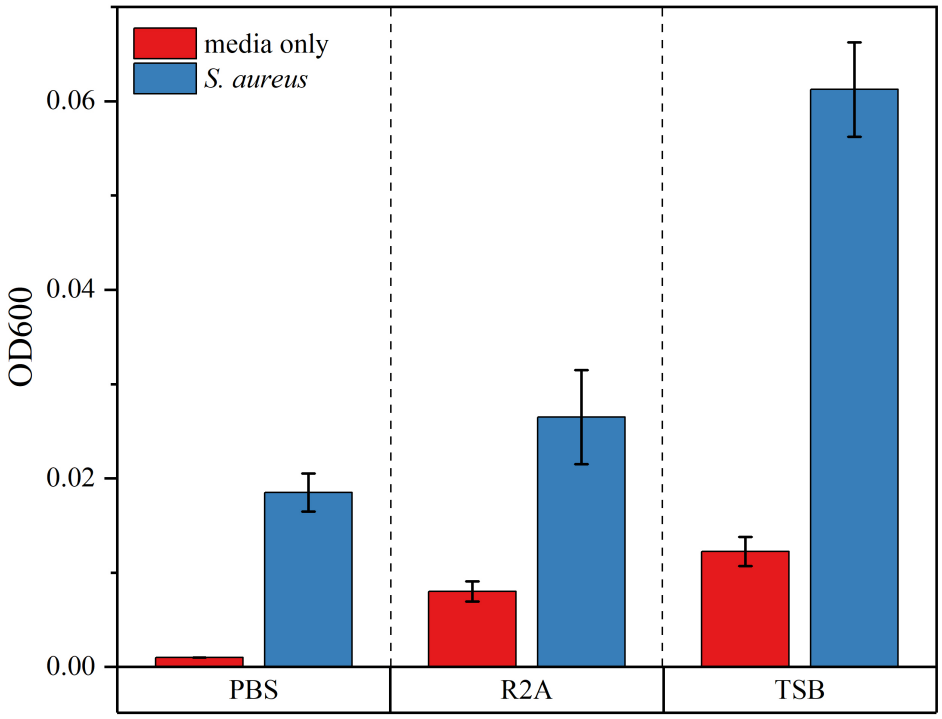

Figure 3.7: Crystal violet biomass assay of *S. aureus* on gold. The experiment was conducted on QCM-D crystal in well plates, with the QCM-D experimental conditions reproduced. The results show that the more nutrient dense the media, the higher biomass. The data represent the mean of at least three measurements at $t = 24$ h. The errors are standard deviations.

extent of surface coverage. At the end of a QCM-D experiment, at $t = 24$ h, the cells were fixed. The results (Fig. 3.6) show that the bacteria in TSB give rise to full coverage of the sensor, and only partial coverage for bacteria suspended in R2A and PBS. This observation aligns with expectations, as the reduction in nutrients reduces the incentive for bacterial attachment.

A crystal-violet based biomass assay was conducted, following an incubation period of 24 h of bacteria in each of the three liquid environments in a well plate (this allowed for a quicker way to obtain data). This staining method is widely employed for quantifying cell biomass and is commonly applied in the investigation of biofilm development. However, the disruptive nature of the CV assay significantly restricts its application in time-dependent studies. Within this method, the biofilm biomass is determined by assessing the absorbance of the stained sample at 570 nm, with higher biofilm masses producing stronger absorbance signals. Variables such as concentrations, volumes and temperature were kept the same as in the QCM-D experiment to facilitate comparison. The results of the assay are seen in Fig. 3.7. As could be expected based

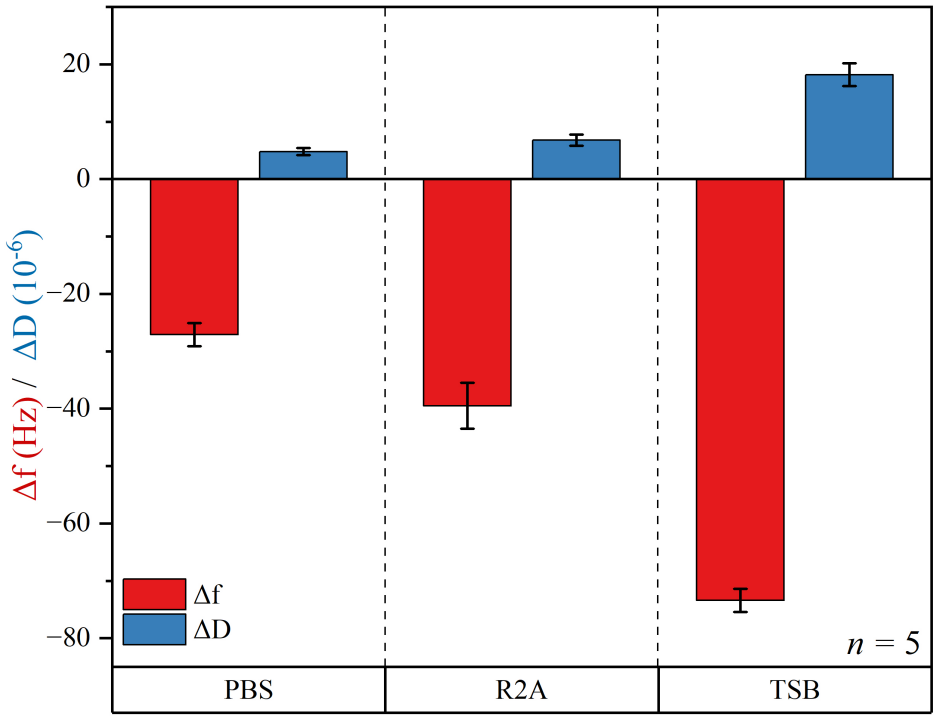

Figure 3.8: Comparison of the average final Δf and ΔD values for *S. aureus* QCM-D experiments. The richer in nutrients the environment, the higher both Δf and ΔD values reached. The data represent the mean of at least three measurements at $t = 24$ h, and the errors are standard deviations.

on the AFM images, the surface-attached biomass was much higher for TSB (OD600 = 0.061). It was intermediate for R2A (0.027), and smallest for PBS (0.019), which is as expected, as the higher the nutrient content, the higher the biomass. Fig. 3.8 shows the maximum dissipation and frequency shifts for each media type. Each data point represents an average of no fewer than three measurements, with error bars denoting standard deviations. The results show that the higher the biomass and surface coverage, the higher the maximum Δf and ΔD values, suggesting that the QCM-D results may be used to indicate extent of deposited mass on the surface.

In summary, the initial experiments of *S. aureus* in PBS confirmed the potential of studying bacteria-surface interactions using QCM-D due to distinct signals compared to the PBS-only reference. However, bacteria suspended in PBS are exposed to starvation and stress, rendering them unsuitable for observing biofilm formation. Furthermore, when bacteria in R2A medium were introduced, a limited interaction with the surface was observed, as indicated by minor changes in frequency and dissipation compared to the media-only reference, suggesting that

R2A was not conducive to studying biofilm formation. The partial coverage of the Au surface by bacteria in R2A at 24 hours seen in AFM images further supports this conclusion. Despite these limitations, intriguing results were observed when bacteria were cultured in TSB. The introduction of bacteria yielded a distinct profile, showing a characteristic peak and a multi-stage interaction with the surface, indicating potential in studying bacterial behaviour using QCM-D in relatively complex growth media. Similar features in literature QCM-D experimental data have been shown to represent the different stages of biofilm formation and changes in cell-surface mode of adhesion. Additionally, AFM imaging revealed full surface coverage by bacteria at 24 hours, indicating the chosen experimental time-frame is suitable for monitoring and characterising bacterial behaviour during biofilm development.

3.2 The viscoelastic and adhesive characteristics of *P. aeruginosa*

This section evaluates the applicability of QCM-D for investigating interactions between a different bacterial species, *P. aeruginosa*, and a Au surface. *P. aeruginosa* is recognised for its strong adaptability and antibiotic resistance, having a rod-shaped form and classified as a Gram-negative bacterium due to its thin peptidoglycan layer encased by an external membrane. In contrast to *S. aureus*, the bacterium is motile, using flagella to move. It flourishes in diverse settings such as soil, water, and within human hosts, positioning it as a frequent opportunistic pathogen and a key subject for research. The cells possess various adhesins, including pili, which facilitate attachment to host tissues and abiotic surfaces. *P. aeruginosa* biofilms are known to be highly organised and structured.

Initially, an experiment with *P. aeruginosa* in PBS buffer was performed to confirm that interactions with the surface are detectable under simple, nutrient-deprived conditions. Further experiments were designed to explore the dynamics of these interactions progressively and in different environmental conditions. Anticipated results should shed light on the viscoelastic characteristics of the bacterial biofilm and its adhesion mechanisms, essential for comprehending the process of biofilm development.

3.2.1 QCM-D monitoring of *P. aeruginosa*

The Δf data for *P. aeruginosa* in the nutrient-free environment of PBS (Fig. 3.9a) show an initial peak which occurs after the cell suspension is introduced into the system due to the system adjusting from the flow to non-flow conditions. This is followed by a steady decrease in Δf up to the value of -18.7 Hz for the 3rd overtone (n = 5: -26.6 Hz, n = 7: -28.1 Hz). The PBS only reference signal similarly shows a gradual decrease in Δf, however, the values reached are $\approx$ -10 Hz for all three overtones. The lower values reached by the bacteria sample suggest the

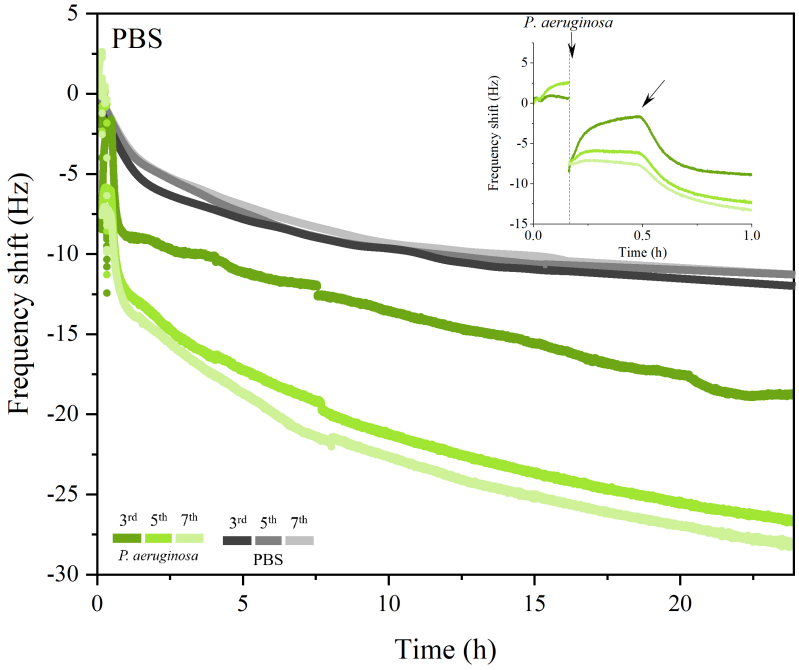

(a) Frequency

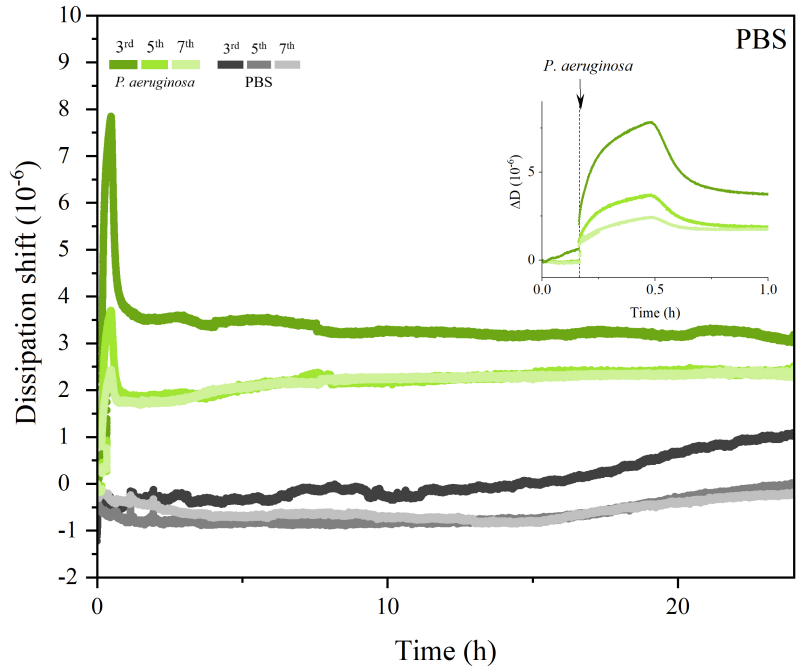

(b) Dissipation

Figure 3.9: Time-dependent frequency, Δf, and dissipation, ΔD, response of gold-coated QCM-D surface to *P. aeruginosa* suspended in PBS. A reference measurement in pure PBS buffer is included.

signal arises due to bacterial interaction with the substrate. Additionally, the observed spacing in the overtones further supports the idea that a layer of cells has formed, as when the softness or thickness increases, a separation of the overtones arises due to the difference in wavelength, and so penetration depth, of the different overtones.

Similarly, the ΔD data (Fig. 3.9b) show an initial peak after the the cell suspension is introduced into the system. This is followed by a stabilisation of the signal throughout the rest of the experimental time-frame to $n = 3$ of 3.1×10^{-6} at $t = 24$ h. The higher overtones gradually increase throughout ($n = 5$: 2.3×10^{-6}, $n = 2.5 \times 10^{-6}$). The PBS reference shows lower ΔD throughout.

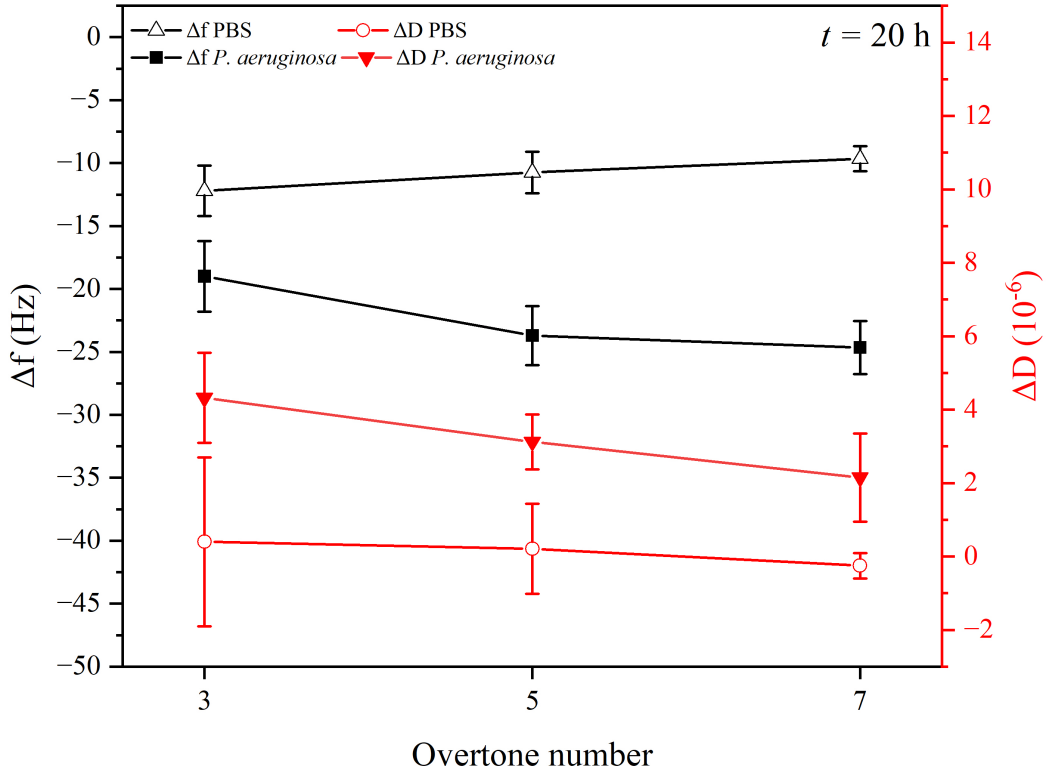

Figure 3.10: Differences in frequency and dissipation at the different overtone numbers for a reference sample (PBS only) and bacterial sample (*P. aeruginosa* in PBS), showing differences for all overtones. The data represent the mean of at least three measurements calculated at the time point $t = 20$ h. The errors are standard deviations.

Fig. 3.10 shows Δf and ΔD values from the three overtones compared to the reference PBS measurement. For all overtones the Δf and ΔD are reproducibly higher than the reference, meaning they reflect bacterial interactions. Both the Δf and ΔD are higher for the lowest

overtone, $n = 3$, in the bacteria results. There is also larger variability, as evidenced by the size of the error bars. This is perhaps occurring due to the stronger interaction of lower overtones with the liquid medium, as they penetrate deeper.[170] The next set of experiments focus on whether *P. aeruginosa* biofilm development can be studied using QCM-D.

3.2.2 Investigating *P. aeruginosa* colonisation across varied growth media

In order to study biofilm formation in *P. aeruginosa*, the conditions of the cells should include nutrients. The following experiment therefore focus on bacteria suspended in growth media. Fig. 3.11 displays the results obtained with R2A broth, which provides minimal nutrient conditions for bacteria. The Δf data reveal an initial steep, stepwise decrease until approximately 1.7 h, followed by a gradual decline, reaching around –56.2 Hz for the 3rd overtone ($n = 5$: -55.1 Hz, $n = 7$: - 57.8 Hz). The close spacing of the responses across the three overtones suggests that the deposited surface layer is relatively rigid. In comparison to the R2A-only baseline, the bacterial experiments consistently show lower Δf values.

The ΔD data (Fig. 3.11b) for the bacterial experiments are remarkably similar to those for the R2A-only reference. One possible explanation is that the inherent viscoelastic properties of the R2A medium dominate the dissipation response, thereby masking any additional damping effects from bacterial adhesion.[147] Alternatively, the bacteria might form a relatively rigid adsorbed layer that does not substantially alter the overall energy dissipation compared to the medium alone. Both interpretations remain hypotheses to be further explored.

In experiments using TSB, a broth with high nutrient density conducive to biofilm formation, the initial decrease in Δf (Fig. 3.12a) was nearly identical for both the bacterial experiments and the TSB-only reference. However, at around 10 h the bacterial experiment exhibits a more rapid drop in Δf , reaching approximately –79.3 Hz for the 3rd overtone $n = 5$: -75.8 Hz, $n = 7$: -72.5 Hz). The corresponding ΔD data (Fig. 3.12b) show an initial swift increase followed by a gradual rise, with final values around 13.0 10^{-6} at 24 h ($n = 5$: 9.8×10^{-6}, $n = 8.3 \times 10^{-6}$). The slight differences in ΔD between the bacterial and TSB-only experiments further support the notion that the viscoelastic contributions of the bacteria are not markedly different from those of the medium itself.

Fig. 3.13 presents comparative plots of Δf and ΔD, with each point representing the mean of at least three measurements and standard deviations indicating experimental variability. Although differences in media composition preclude direct quantitative comparisons, distinct Δf profiles emerge across the experiments.

A study investigating the attachment of *P. aeruginosa* to gold in TSB over a comparable period of 25 hours has been reported.[199] Ivanovna *et al.* observed an initial decline in Δf and

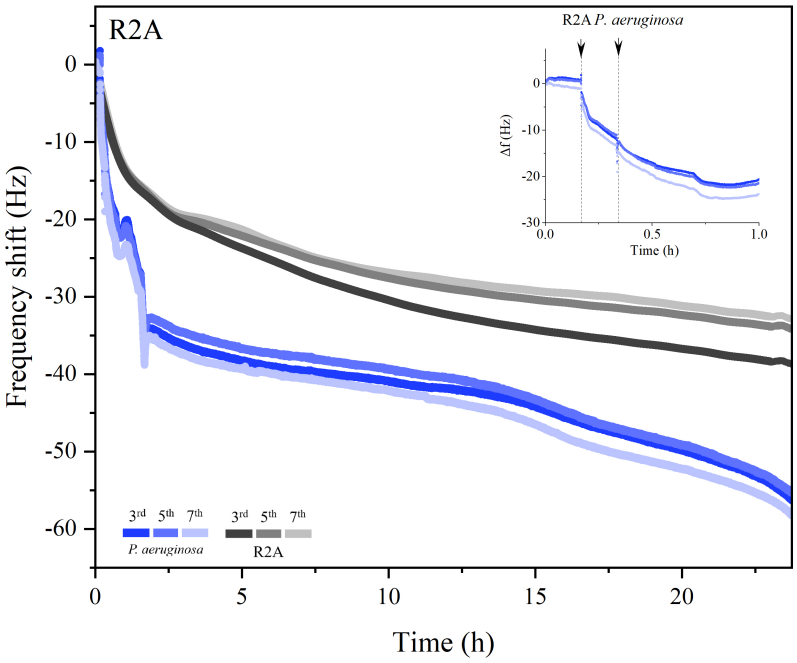

(a) Frequency

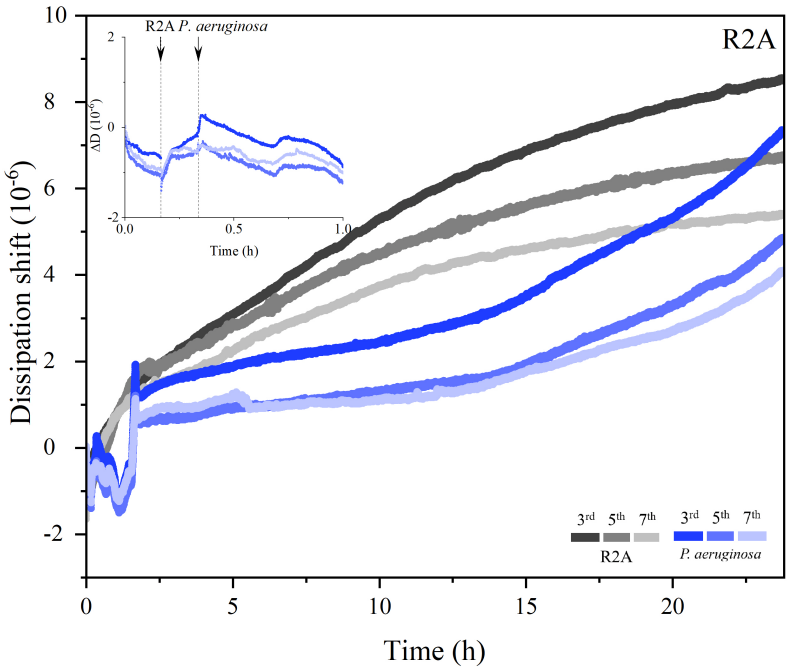

(b) Dissipation

Figure 3.11: Time-dependent frequency, Δf, and dissipation, ΔD, response of gold-coated QCM-D substrate to *P. aeruginosa* suspended in R2A liquid medium. A reference measurement in pure R2A is included.

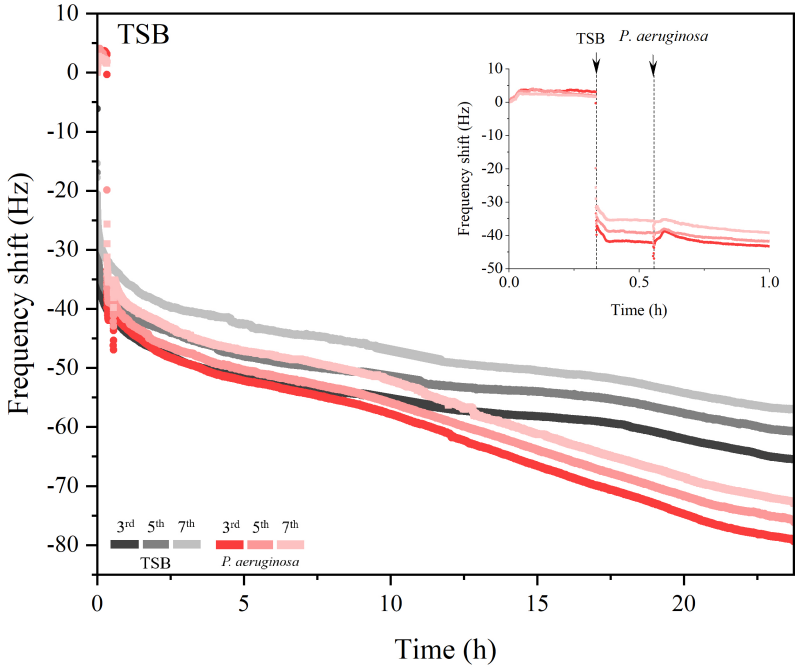

(a) Frequency

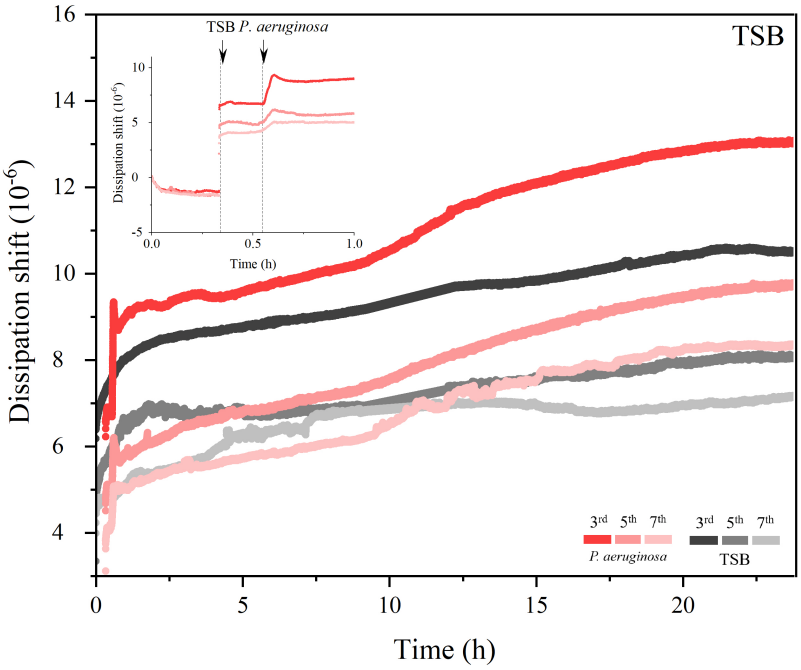

(b) Dissipation

Figure 3.12: Time-dependent frequency, Δf, and dissipation, ΔD, response of gold-coated QCM-D substrate to *P. aeruginosa* in TSB medium. A reference measurement in pure TSB is included.

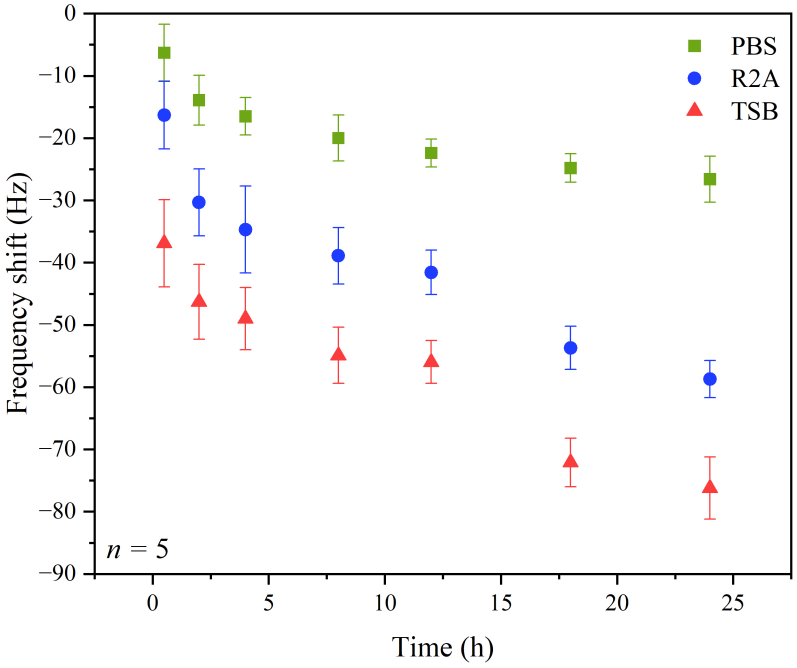

(a) Frequency

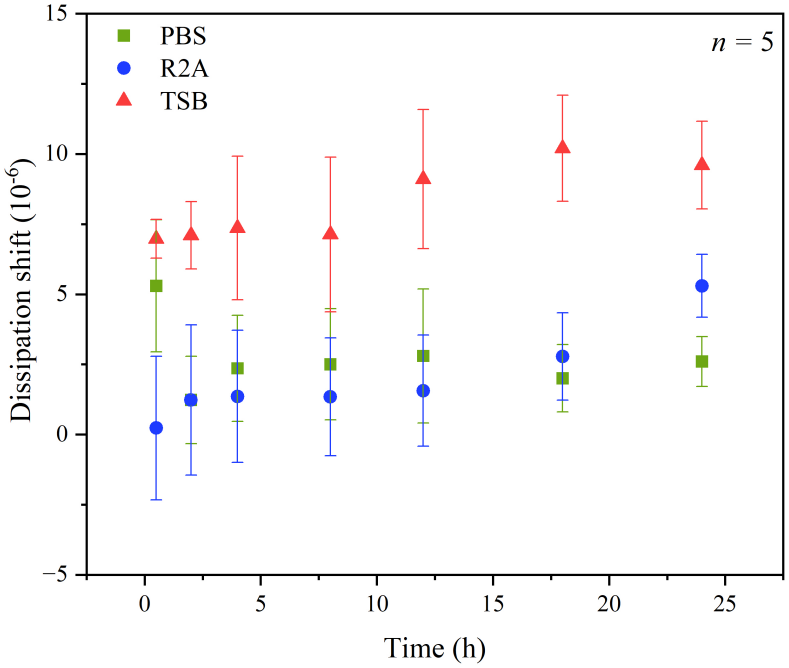

(b) Dissipation

Figure 3.13: Comparison of Δf and ΔD for *P. aeruginosa* in three different growth media displaying emergence of differences over time. The middle, 5th, overtone is chosen for easier visualisation. The data represent the mean of at least three measurements calculated at the time points t = 0.5, 2, 4, 8, 12, 18, 24 h. The errors are standard deviations.

a rise in ΔD between 0.5 and 2 hours, a pattern also seen in the R2A and TSB experiments presented in this section. These early rapid shifts were attributed to a combination of a swift "bulk shift" caused by the change in medium and the rapid attachment of media components and *P. aeruginosa* cells to the surface. Following this initial phase, steady increases in the signals were interpreted as indicative of cellular growth on the surface, which was then followed by a more pronounced decrease in Δf and an increase in ΔD at 11–13 h.

The R2A and TSB data display a striking similarity to these findings, with a consistent drop in Δf observed between 10 and 13 h. Notably, this drop is absent in the nutrient-free PBS results, suggesting that it is closely linked to the presence of nutrients. Since PBS does not support robust biofilm formation, the changes seen in the presence of nutrients are likely associated with biofilm-related processes. One possibility is that the drop in Δf reflects a reorganisation or consolidation of the biofilm matrix, potentially involving alterations in the interactions and cross-linking among extracellular polymeric substances, which subsequently modifies the viscoelastic properties of the adsorbed layer.[200] Alternatively, the change might signify the detachment or redistribution of cells within the biofilm, contributing to the observed sensor response.[201] Further studies are required to elucidate the precise mechanisms underlying these changes.

Following the QCM-D experiments, a measurement of the relative biomass of the surface-attached cells at $t = 24$ h was conducted using a the crystal violet stain. The results seen in Fig. 3.14 show the highest OD600 value of 0.18 for bacteria in TSB, followed by 0.06 for R2S and 0.04 for bacteria in PBS buffer. This means that the nutrient rich conditions of the TSB liquid medium result in the highest amount of surface-associated cells. Low density nutrient medium of R2A gives rise to a markedly lower amount of cells at the sensor surface, followed by PBS resulting in only slightly less than R2A. As could be expected, the higher the nutrient concentration, the higher the biomass at the surface.

An AFM tapping mode image (Fig. 3.15) was obtained for the cells in R2A. (Unfortunately, images were not obtained for the other two media due to experimental difficulty in imaging *P. aeruginosa*.) The image provides further evidence for bacterial attachment to the Au-sensor surface, and shows only partial coverage of the crystal at $t = 24$ h.

In summary, the relative biomass (Fig. 3.14) of the surface associated cells at $t = 24$ h has been shown to increase with nutrient concentration of the media. The final Δf and ΔD values for each of the three liquid media are shown in Fig. 3.16. The greater the nutrient concentration of the media and the greater the biomass, the lower the Δf and the greater the ΔD. This observation, alongside the distinct QCM-D signal profiles of *P. aeruginosa* interaction with gold suggests promise in the use of QCM-D in the study of biofilm development of this organism. However, the uncertainty in the ΔD data appear to be large. This suggests that,

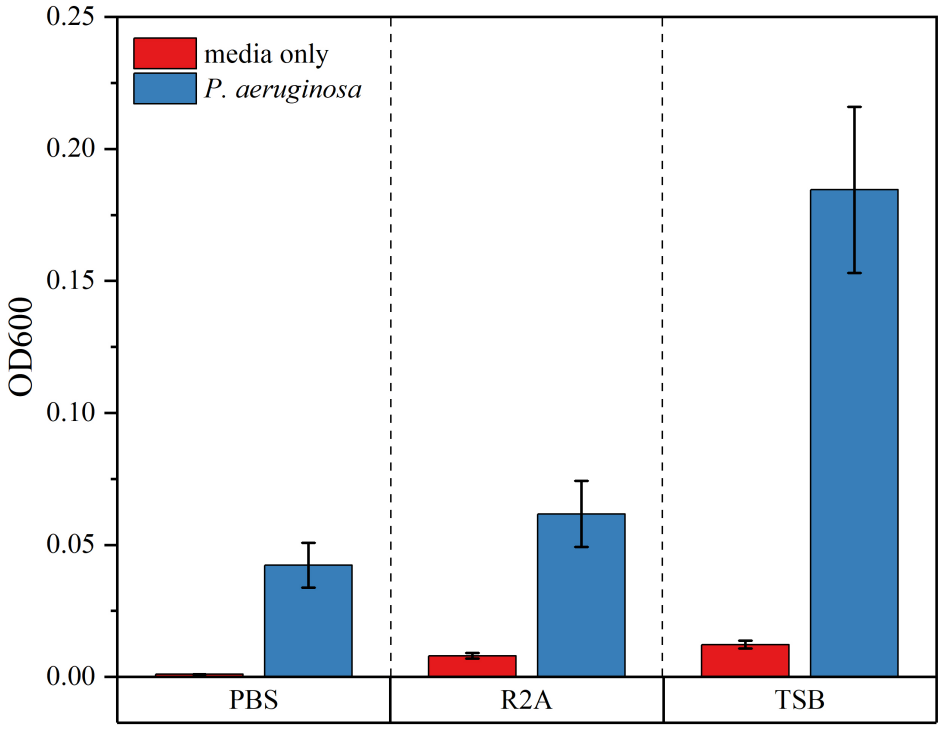

Figure 3.14: Crystal violet biomass assay of *P. aeruginosa* on gold. The experiment was conducted on QCM-D crystal in well plates, with the QCM-D experimental conditions reproduced. The results show that the more nutrient dense the media, the higher biomass. The data represent the mean of at least three measurements at $t = 24$ h. The errors are standard deviations.

overall, although some patterns emerge when looking at the *P. aeruginosa* QCM-D results when combined with biomass estimation, the ΔD component may not be as informative as the Δf signals, which were more distinct from their baselines across the experiments.

3.3 Comparing surface colonisation of *S. aureus* vs. *P. aeruginosa*

This section compares the QCM-D findings for *S. aureus* and *P. aeruginosa*, the responses of two structurally different bacteria,[202] across three different media types (TSB, R2A, PBS), offering insights into the dynamics of biofilm formation under diverse environmental conditions. Differences in the Δf and ΔD signals between the two strains are examined, and the data are visualised in dissipation versus frequency (Df) plots, often referred to as adhesion fingerprints

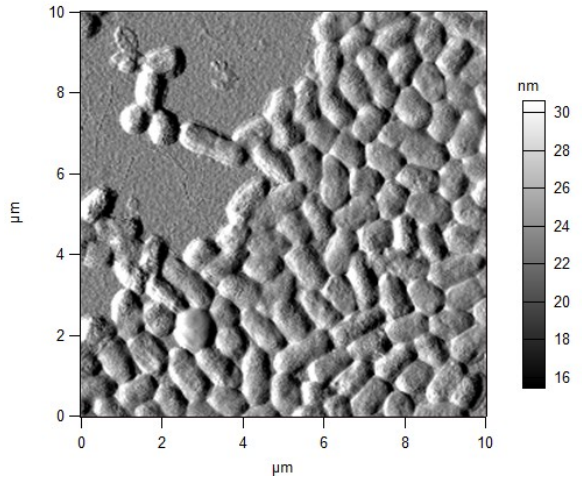

Figure 3.15: Tapping mode AFM images of Au-coated QCM-D sensor after measurements of *P. aeruginosa* interaction with the surface in R2A liquid media, showing partial surface coverage at $t = 24$ h.

[203]. Although the viscoelastic properties of cells are partly determined by their internal organisation, with more structured interiors typically yielding greater stiffness, the *Df* plots in this context capture the overall mechanical behaviour of the adhered film, including contributions from both cellular and extracellular components.[204] Given that only a fraction of cell mass contributes to the frequency shift during adhesion due to the inherently dissipative nature of bacterial cells, these *Df* plots serve as compelling signatures for distinguishing between different bacterial adhesion mechanisms.

In PBS (Fig. 3.17), both the Δf and ΔD responses follow similar trends for the two species. An initially steep decrease in Δf is followed by a more gradual decline, resulting in overlapping values, while ΔD shows an immediate increase that stabilises throughout the experiment—albeit with a slightly higher final ΔD for *S. aureus* (approximately 2×10^{-6}). Although these individual signals do not offer a clear basis for discrimination, the corresponding *Df* plots reveal characteristic adhesion fingerprints for each strain.

The gradient of the *Df* plots provides further insight into the mechanical properties of the biofilm. For *P. aeruginosa*, a relatively shallow slope indicates a more rigid and uniform film, likely resulting from a denser, highly cross-linked EPS network and the stabilising influence of surface appendages such as type IV pili and flagella [83, 193, 205, 206]. In contrast, *S. aureus* relies predominantly on cell wall-associated adhesins and develops a more heterogeneous EPS matrix [207, 208], leading to a steeper *Df* gradient that suggests the biofilm undergoes more dynamic structural changes during the experimental timeframe.

The R2A results (Fig. 3.20) show that initial Δf and ΔD readings for both species are comparable; however, divergence becomes evident over time. *S. aureus* displays increased ΔD

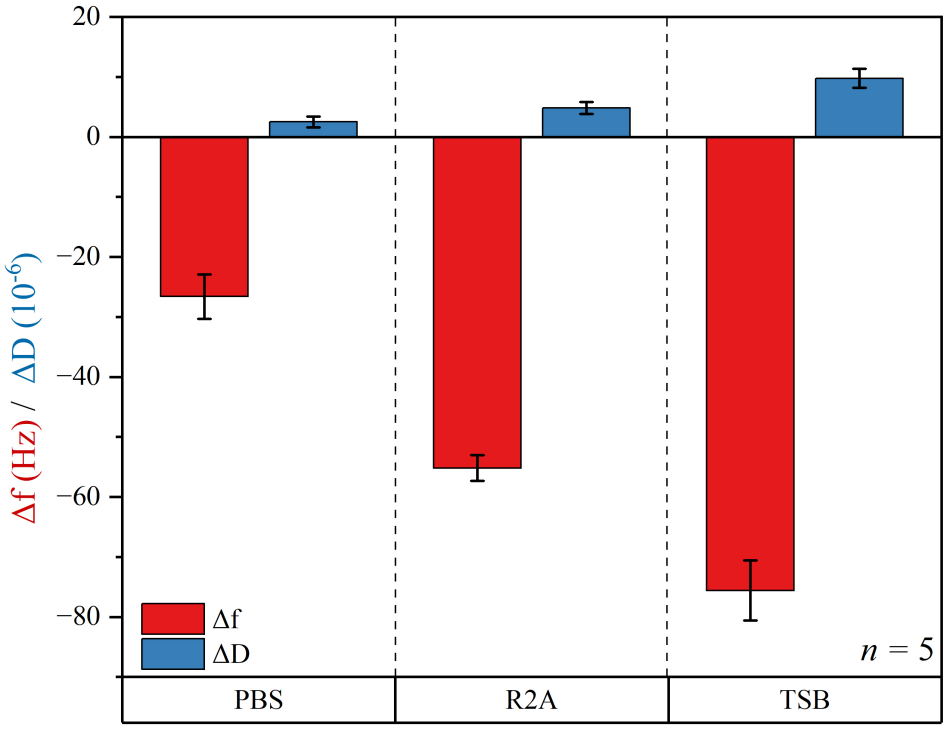

Figure 3.16: Comparison of the average final Δf and ΔD values for *P. aeruginosa* QCM-D experiments. The richer in nutrients the environment, the higher both Δf and ΔD values reached. The data represent the mean of at least three measurements at $t = 24$ h, and the errors are standard deviations.

values, while *P. aeruginosa* exhibits elevated Δf levels. This divergence underscores the importance of prolonged monitoring in distinguishing bacterial behaviours. The related *Df* plot (Fig. 3.22) presents a smaller slope for *P. aeruginosa*, indicative of greater stiffness, and a steady slope for both species suggests that the mass loading is associated with uniform viscoelastic properties over the experimental period.

In TSB, the Δf results reveal a transient positive frequency peak in the *S. aureus* data, a signature of an initial weak/reversible adhesion phase, whereas the final Δf values at $t = 24$ h are similar for both species. The ΔD readings are consistently higher for *S. aureus*, with a characteristic peak at $t = 8$ h that is absent in the *P. aeruginosa* data. The *Df* plots in TSB indicate significant changes in stiffness for the *S. aureus* biofilm, while *P. aeruginosa* maintains a relatively constant, shallower slope, reflecting a stiffer, more uniformly structured film.

Overall, in PBS the nearly identical Δf and ΔD responses suggest that low-nutrient con-

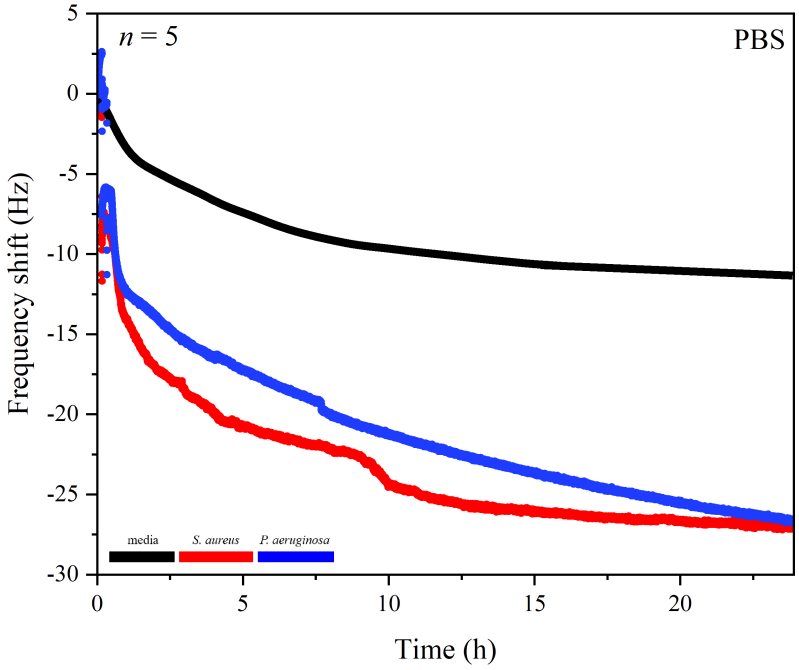

(a) Frequency

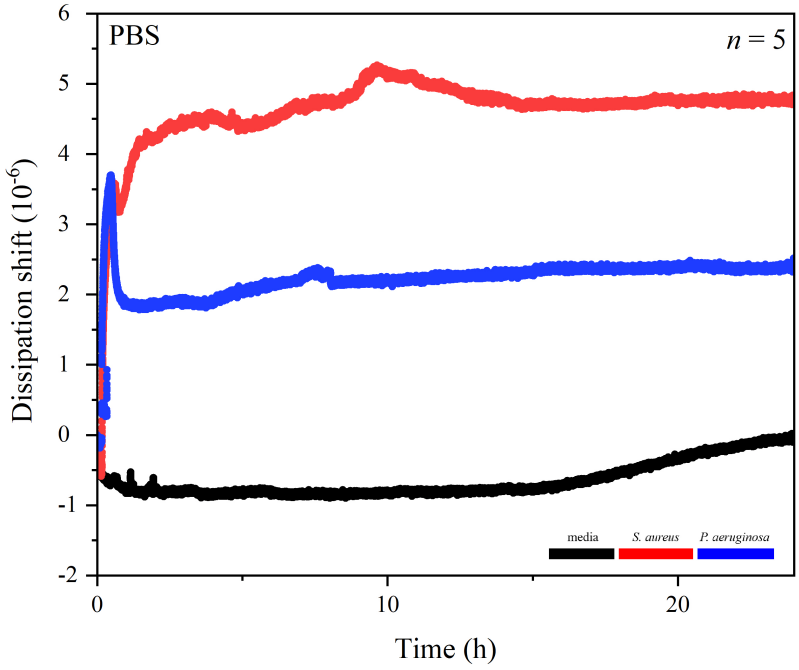

(b) Dissipation

Figure 3.17: Time-dependent frequency, Δf, and dissipation, ΔD, response of gold-coated QCM-D surface to *S. aureus* and *P. aeruginosa* suspended in PBS. A reference measurement in pure PBS buffer is included. Fifth harmonic results included only.

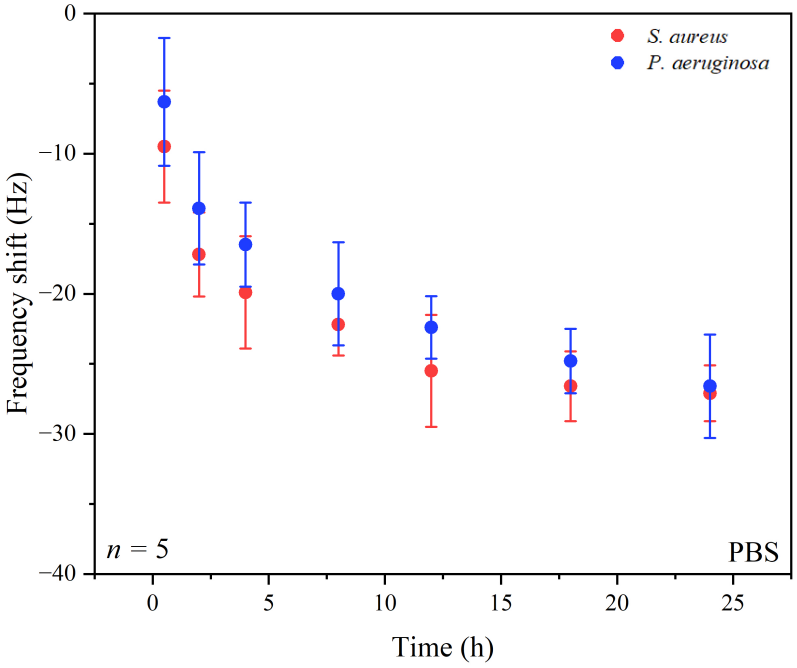

(a) Frequency

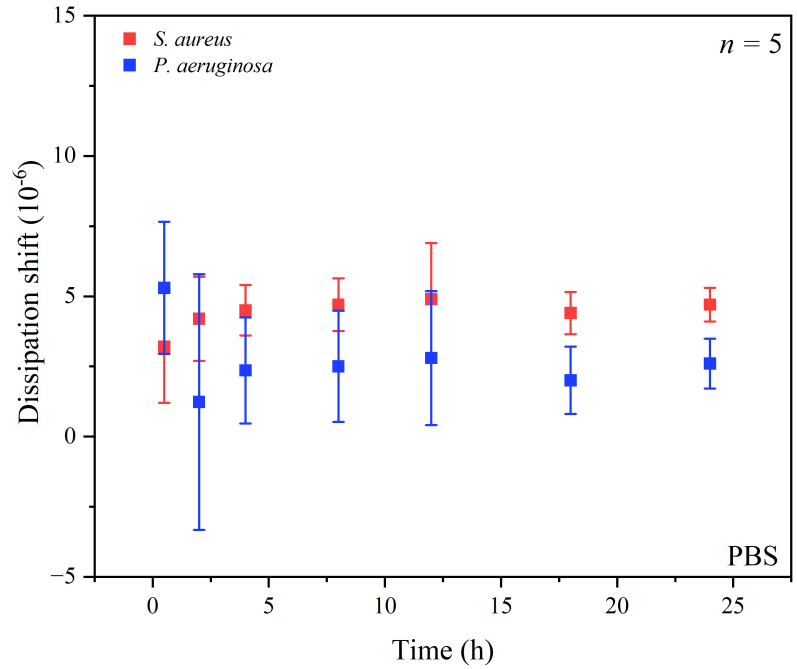

(b) Dissipation

Figure 3.18: Comparison of Δf and ΔD for *S. aureus* and *P. aeruginosa* in PBS over time. The middle, 5th, overtone is chosen for easier visualisation. The data represent the mean of at least three measurements calculated at the time points t = 0.5, 2, 4, 8, 12, 18, 24 h. The errors are standard deviations.

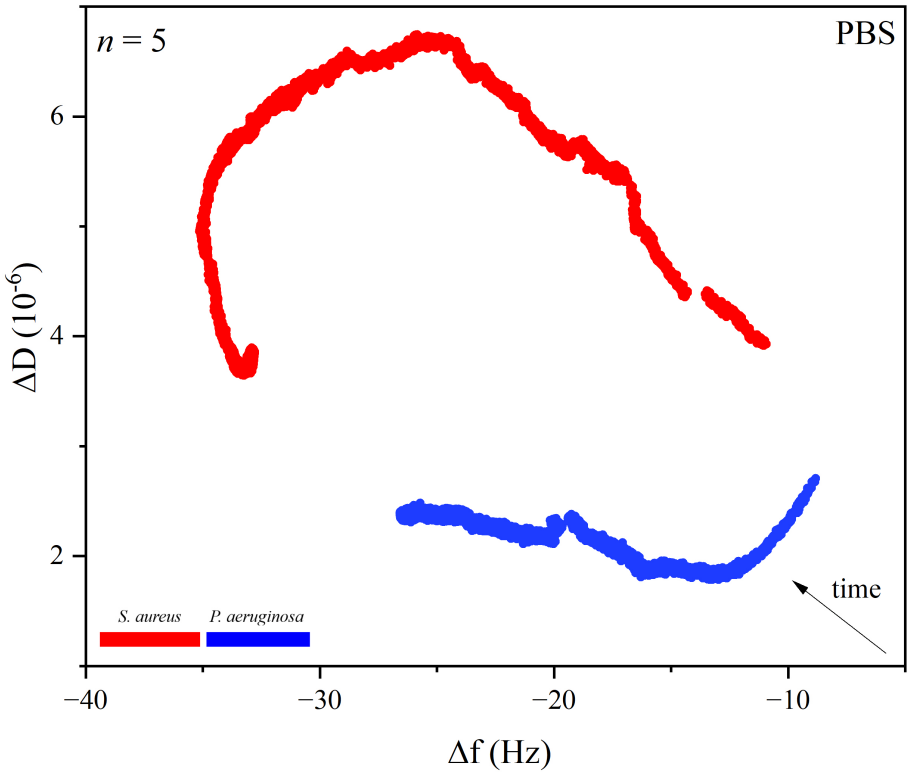

Figure 3.19: Dissipation versus frequency (Df) plots compared between *S. aureus* and *P. aeruginosa* in PBS.

ditions result in limited EPS production and slower growth, minimising differences in biofilm properties. In contrast, richer media such as R2A and TSB reveal divergence in QCM-D responses. Notably, at 8 h in the R2A data, differences begin to emerge, emphasising the value of long-term monitoring. In TSB, reproducible features observed for *S. aureus* that are absent in *P. aeruginosa* indicate that enhanced biofilm component production in nutrient-rich environments accentuates interspecies differences. Across all media, ΔD measurements consistently show that *S. aureus* forms biofilm layers with higher overall viscoelasticity, while *P. aeruginosa* develops stiffer layers. Although some Δf and ΔD values overlap, their combined representation in the Df plots yields distinct curves that serve as characteristic signatures of the unique biofilm formation behaviours under varying nutrient conditions.

QCM-D measurements reveal that *S. aureus* exhibits notably higher energy dissipation than *P. aeruginosa*, which can be attributable to the intrinsic mechanical properties of their cell walls. Increased dissipation in QCM-D reflects greater energy loss during sensor oscillation, a consequence of the viscoelastic nature of the bacterial layer adsorbed on the surface. As a Gram-positive bacterium, *S. aureus* possesses a thick, flexible peptidoglycan layer that de-

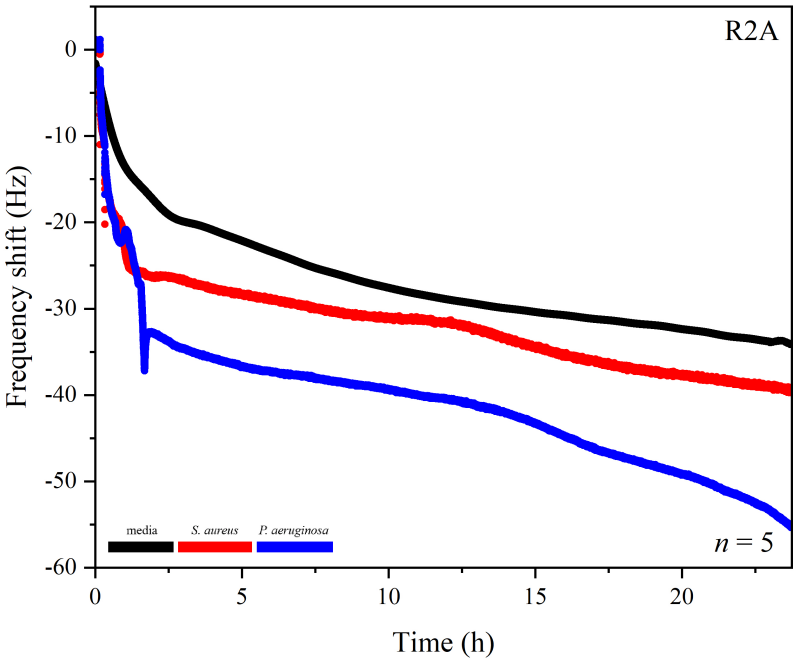

(a) Frequency

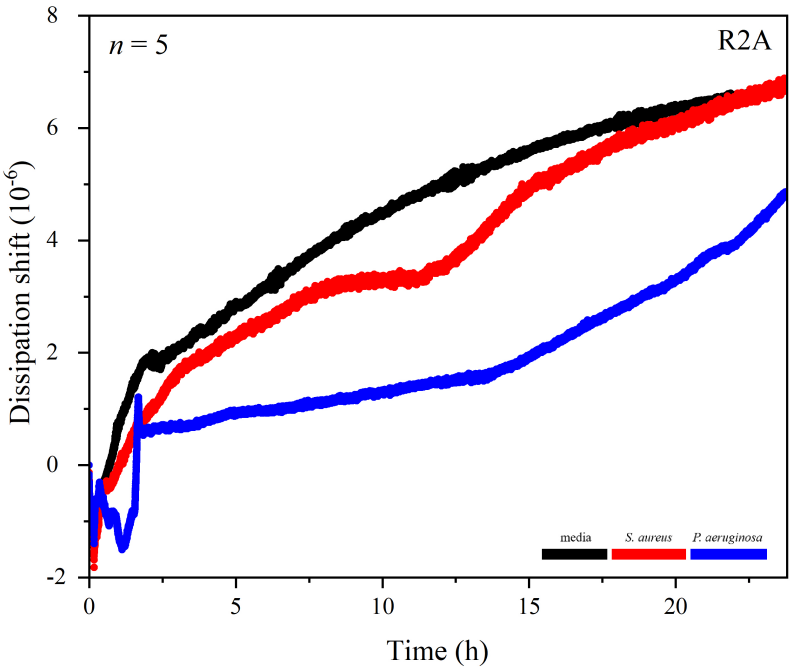

(b) Dissipation

Figure 3.20: Time-dependent frequency, Δf, and dissipation, ΔD, response of gold-coated QCM-D surface to *S. aureus* and *P. aeruginosa* suspended in R2A. A reference measurement in pure PBS buffer is included. Fifth harmonic results included only.

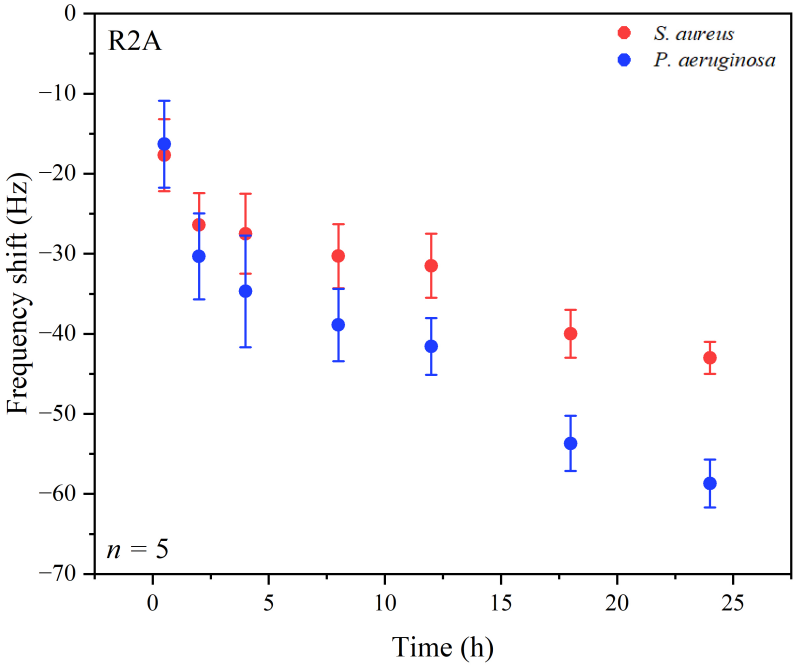

(a) Frequency

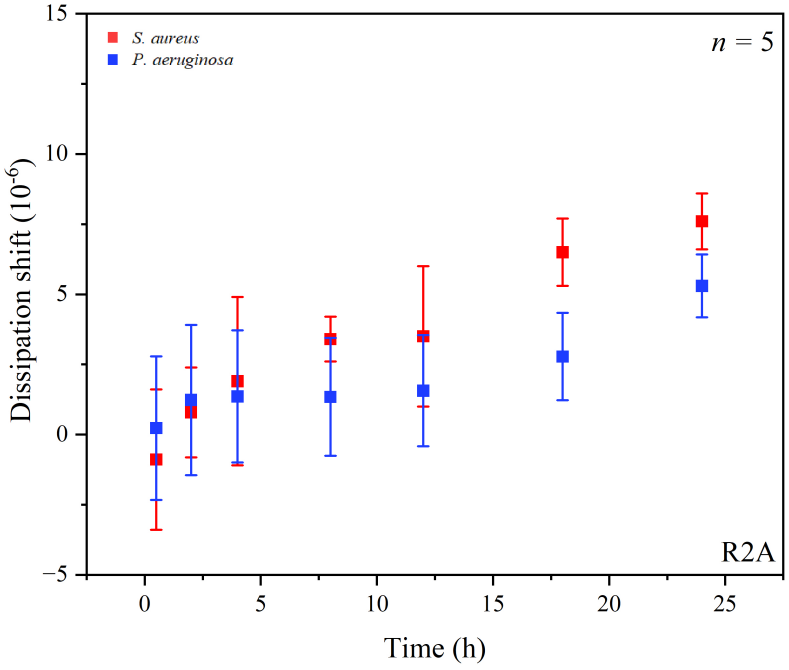

(b) Dissipation

Figure 3.21: Comparison of Δf and ΔD for *S. aureus* and *P. aeruginosa* in R2A over time. The middle, 5th, overtone is chosen for easier visualisation. The data represent the mean of at least three measurements calculated at the time points t = 0.5, 2, 4, 8, 12, 18, 24 h. The errors are standard deviations.

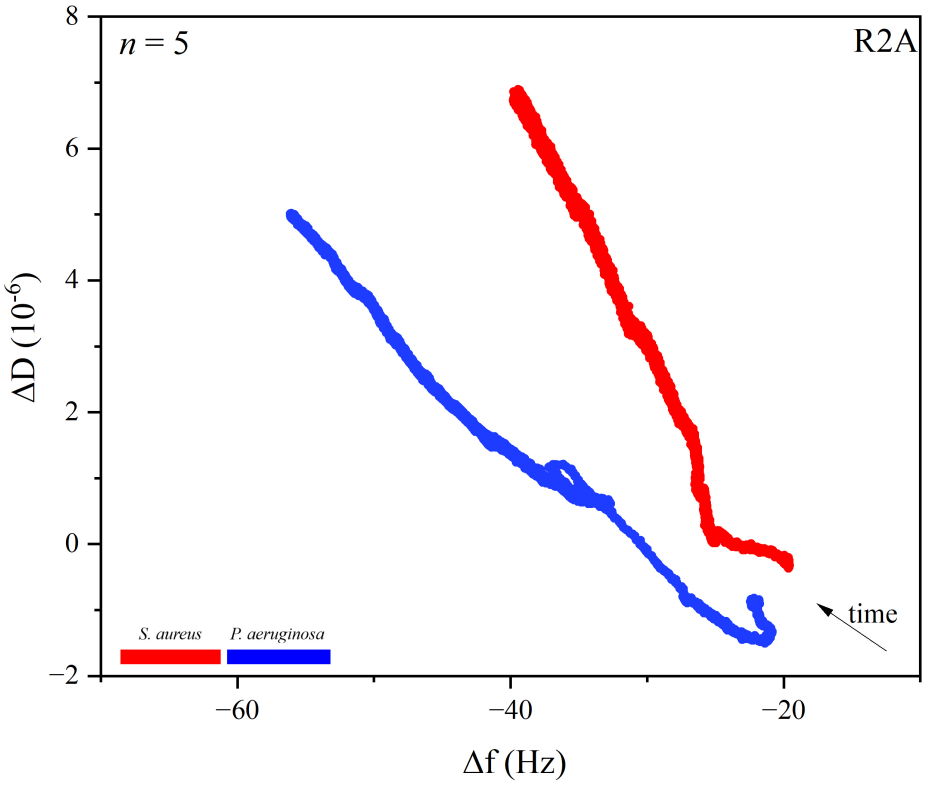

Figure 3.22: Dissipation versus frequency (Df) plots compared between *S. aureus* and *P. aeruginosa* in R2A.

forms significantly under shear stress, resulting in a softer, more compliant film. Atomic force microscopy studies by Touhami et al. [209] and Dufrêne [210] have demonstrated that more deformable bacterial surfaces dissipate greater energy when mechanically perturbed, supporting the observation of higher dissipation shifts for *S. aureus*. In contrast, the Gram-negative *P. aeruginosa* has a much thinner peptidoglycan layer, further reinforced by a rigid outer membrane enriched with lipopolysaccharides [33]. This inherent rigidity limits deformation, producing a stiffer bacterial film that incurs minimal energy loss and, consequently, lower dissipation shifts. Although both species exhibit a similar moderately negative surface charge [211–213], the fundamental differences in their cell wall mechanics primarily govern their adhesive behaviour as observed by QCM-D.

Additionally, *S. aureus*' teichoic acids promote electrostatic interactions with gold, facilitating initial adhesion through the formation of multiple weaker bonds [3, 207]. This enables an early reversible adhesion phase in *S. aureus*, as evidenced by the transient positive frequency peak observed in TSB data, a phenomenon also reported in studies on Gram-positive adhesion dynamics [156, 214]. The reversible phase may lead to suboptimal packing and subsequent

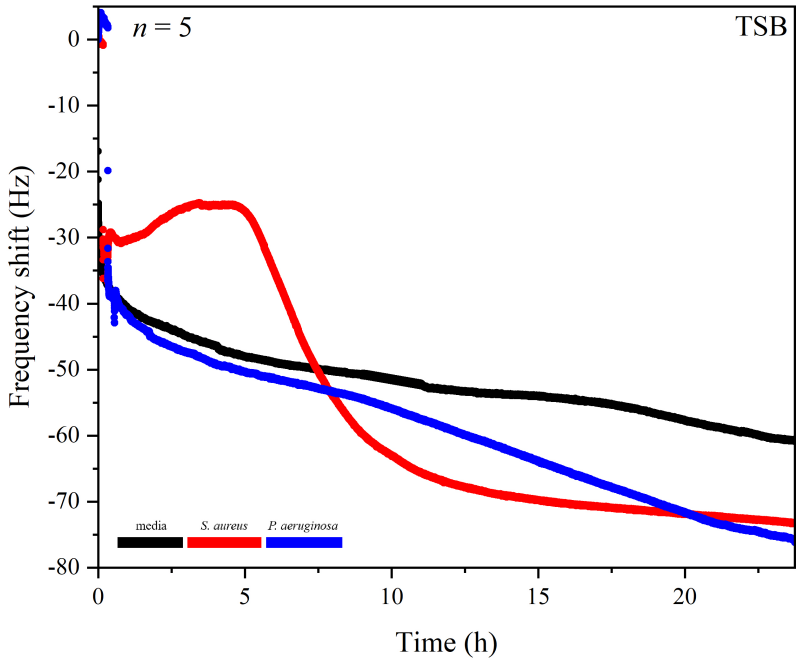

(a) Frequency

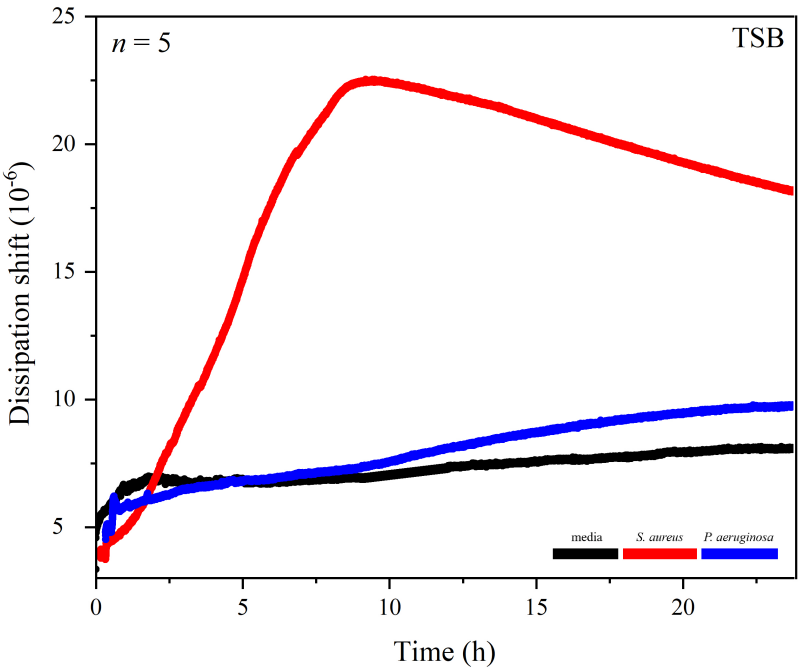

(b) Dissipation

Figure 3.23: Time-dependent frequency, Δf, and dissipation, ΔD, response of gold-coated QCM-D surface to *S. aureus* and *P. aeruginosa* suspended in TSB. A reference measurement in pure PBS buffer is included. Fifth harmonic results included only.

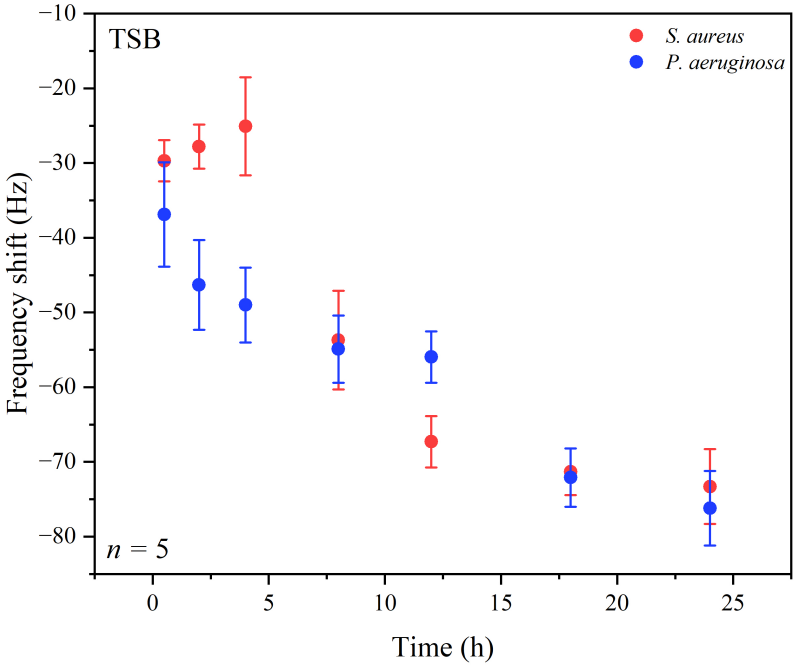

(a) Frequency

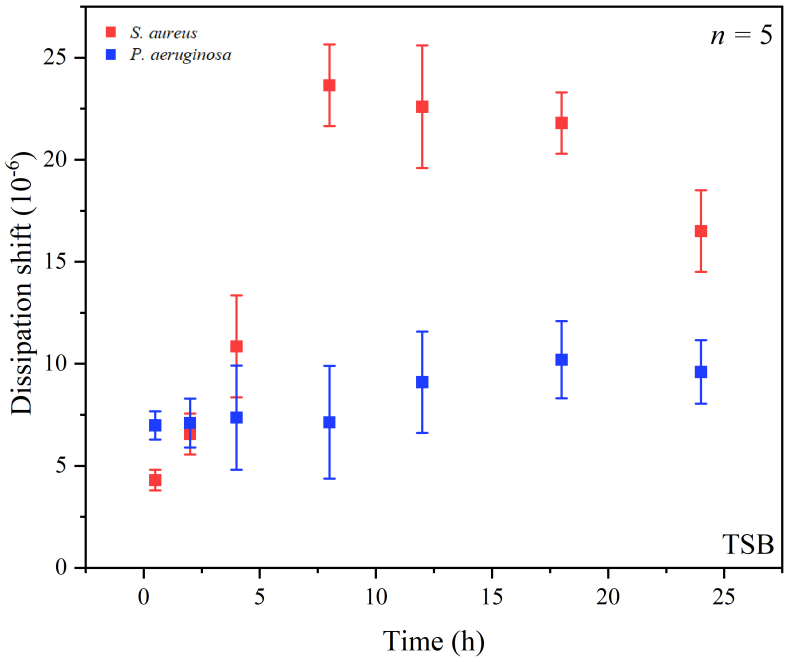

(b) Dissipation

Figure 3.24: Comparison of Δf and ΔD for *S. aureus* and *P. aeruginosa* in TSB over time. The middle, 5th, overtone is chosen for easier visualisation. The data represent the mean of at least three measurements calculated at the time points t = 0.5, 2, 4, 8, 12, 18, 24 h. The errors are standard deviations.

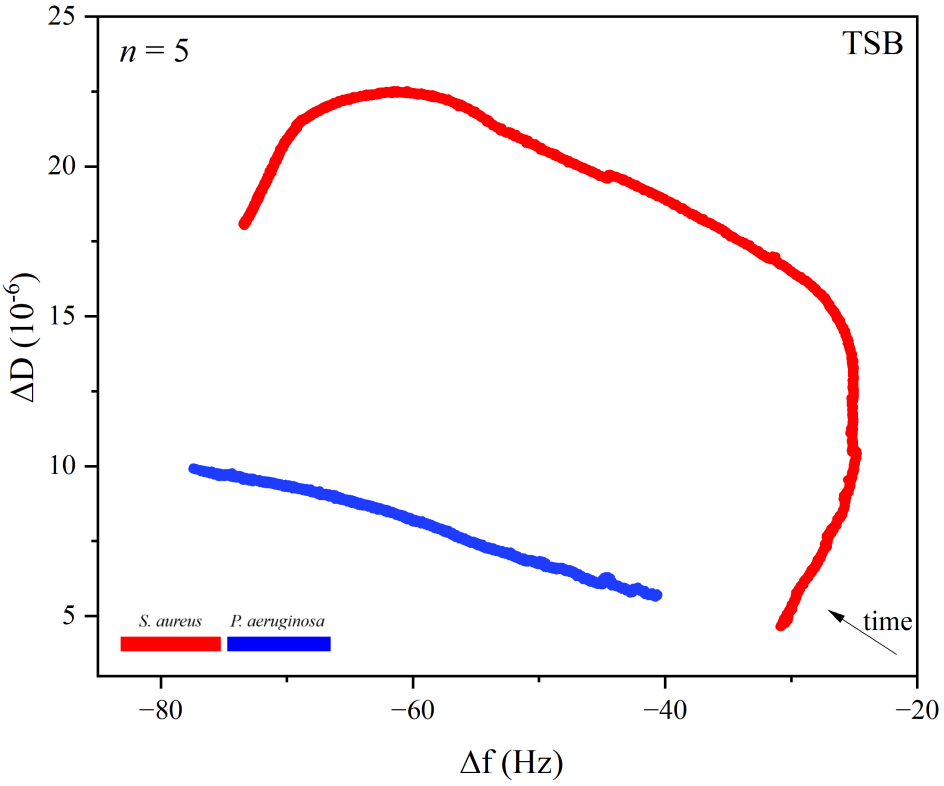

Figure 3.25: Dissipation versus frequency (Df) plots compared between *S. aureus* and *P. aeruginosa* in TSB.

dynamic reorganisation into a multilayered structure, thereby contributing to higher energy dissipation in QCM-D measurements [209, 210]. In contrast, *P. aeruginosa*, being Gram-negative and possessing a much thinner peptidoglycan layer situated between an inner cytoplasmic membrane and a rigid outer membrane enriched with lipopolysaccharides [33], forms stiffer adhesive bonds. The rapid establishment of irreversible adhesion in *P. aeruginosa*, mediated by type IV pili and flagella [28, 206, 215, 216], favours the formation of a well-organised, tightly packed monolayer with minimal deformation, leading to lower dissipation shifts. Type IV pili can actively retract and pull bacteria closer to the surface, effectively propelling the cells down and minimising spacing.[215] Conversely, extensive surface appendages can sometimes sterically hinder close packing[217], thus, this interpretation that *P. aeruginosa* forms a more compact monolayer is one possible explanation consistent with its lower dissipation signal. Alternative interpretations, based on literature, suggest that differences in EPS composition and cross-linking density also contribute significantly to the observed mechanical properties. For instance, a more tightly cross-linked EPS network in *P. aeruginosa*, rich in polysaccharides such as alginate, Pel, and Psl, confers greater rigidity and stability [193, 205, 218, 219], whereas *S. aureus* biofilms may incorporate higher proportions of loosely associated proteins and extracellular DNA, resulting in

a matrix that is less densely cross-linked and more prone to deformation [200, 219]. Collectively, these factors indicate that the higher dissipation observed for *S. aureus* arises not solely from its inherently softer cell wall, but also from the interplay between its EPS composition, lower cross-linking density, and the resultant dynamic structural reorganisation during the early stages of biofilm formation, whereas *P. aeruginosa* forms a more rigid and consistently structured biofilm.

3.3.1 Temperature-dependent surface colonisation of *S. aureus* and *P. aeruginosa*

In this section, the intricate relationships between temperature and surface colonisation behaviour of two prominent bacterial species, *S. aureus* and *P. aeruginosa*, are investigated by QCM-D analysis. Bacterial adhesion processes and biofilm formation can be influenced by temperature variations. By conducting QCM-D studies at different temperatures, we can elucidate how changes in temperature impact the kinetics, viscoelastic properties, and overall stability of bacterial biofilms. An analysis of colonisation at two different temperatures, 25 °C and 37 °C, in the nutrient-dense TSB media that supports biofilm growth is presented. 25 °C is often used to represent room temperature, while 37 °C approximates human body temperature. By studying bacterial behaviour at these two temperatures, we can better simulate the physiological conditions encountered in various environmental and host settings. Through this study, the interactions between temperature and bacterial surface colonisation are sought to be explored, shedding light on the fundamental processes that support biofilm development and its perpetuation.

The QCM-D result for *S. aureus* at two different temperatures can be seen in Fig. 3.26. The Δf data are more negative throughout the experiment. Additionally, the characteristic 5 h peak at 25 °C occurs earlier at $\approx$ 2.5 h, and it less pronounced. The dissipation data, however, are much more similar, indicating comparable viscoelasticity of the two samples. The data seen in Fig. 3.27 show that the QCM-D findings Δf are reproducible, while the ΔD only differ in the beginning of the experiment, at 0.5, 2 and 4 h points, followed by similar result later on.

The results for *P. aeruginosa* differ substantially for the two temperatures. Both sets of data show a two-step progression in the Δf and ΔD signals, where the rate of change of Δf and ΔD increases. However this is much more pronounced and occurs earlier, at $\approx$ 5 h, for the 37 °C sample and at around 10 h at 25 °C. Fig. 3.29 shows the differences in Δf to be reproducible. However, ΔD data show large overlaps in errors, suggesting these data are less reliable in characterising the changes which occur.

The *Df* plots (Fig. 3.30) for the bacteria at the two temperatures show that the characteristic shape of the plot remains, however, changes in the slope arise. The lower temperatures give rise to stiffer layers for both bacteria. However, the difference in temperature has a much

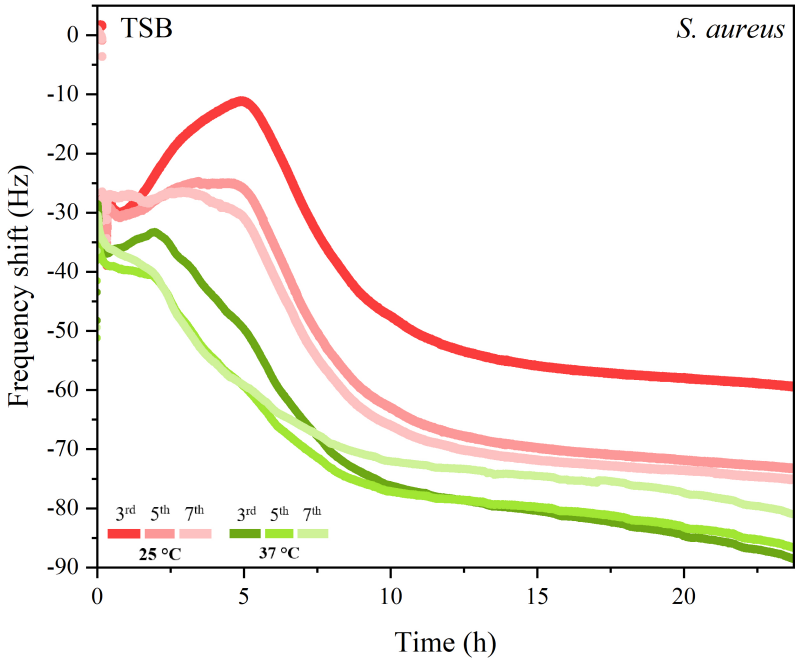

(a) Frequency

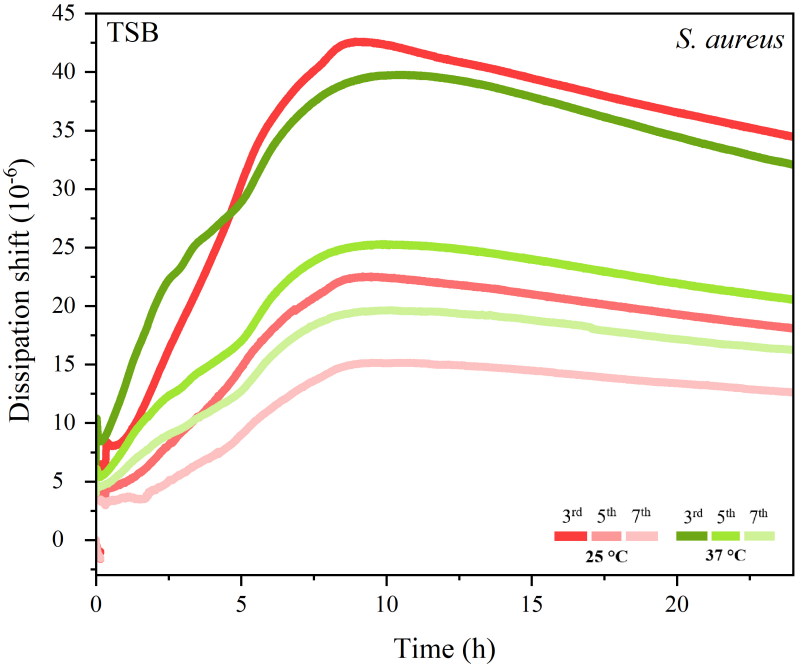

(b) Dissipation

Figure 3.26: Frequency, Δf, and dissipation, ΔD, QCM-D response to *S. aureus* in TSB at 25 °C and 37 °C.

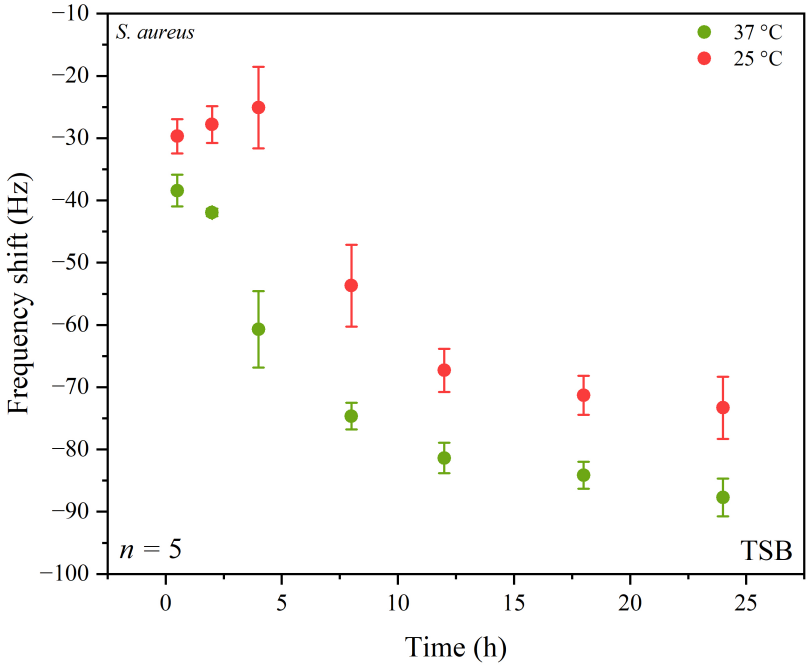

(a) Frequency

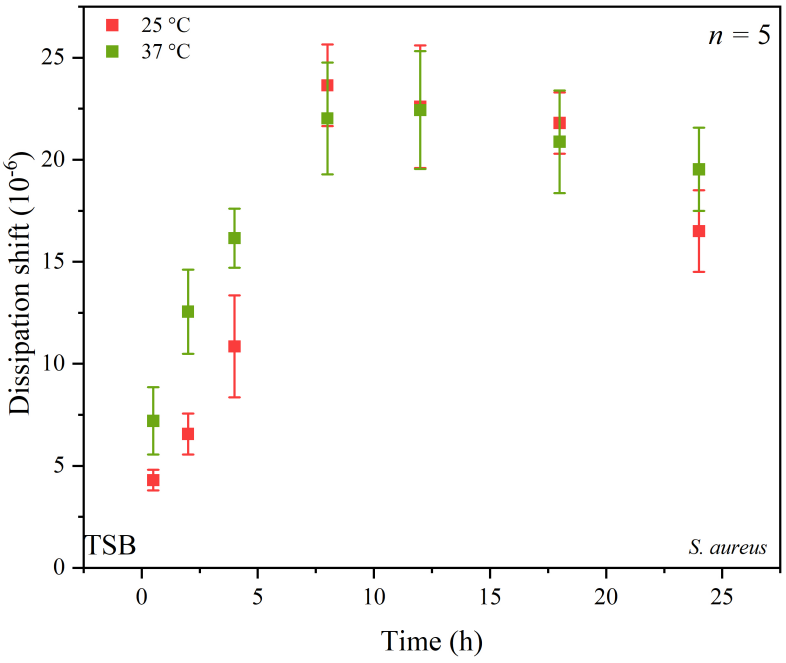

(b) Dissipation

Figure 3.27: Comparison of Δf and ΔD for *S. aureus* in TSB over time at 25 °C and 37 °C. The middle, 5th, overtone is chosen for easier visualisation. The data represent the mean of at least three measurements calculated at the time points t = 0.5, 2, 4, 8, 12, 18, 24 h. The errors are standard deviations.

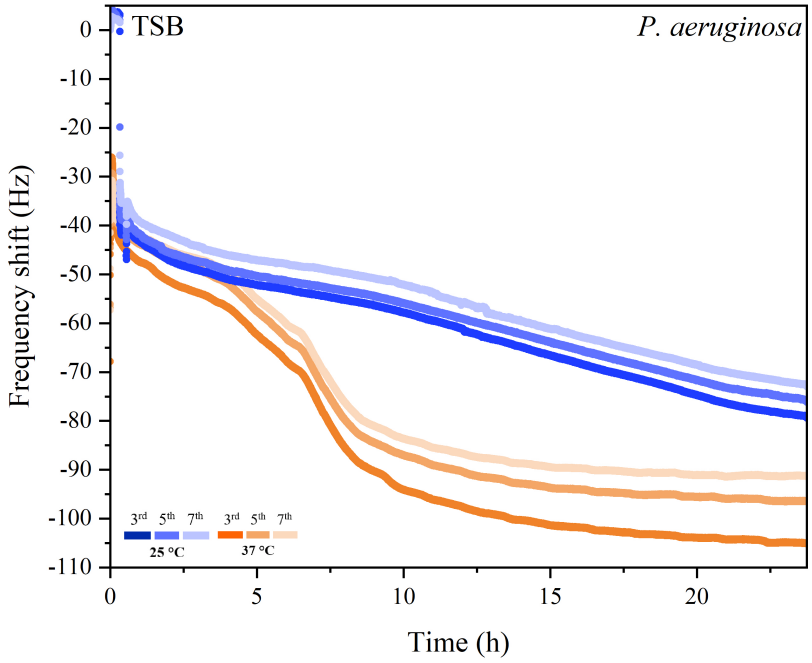

(a) Frequency

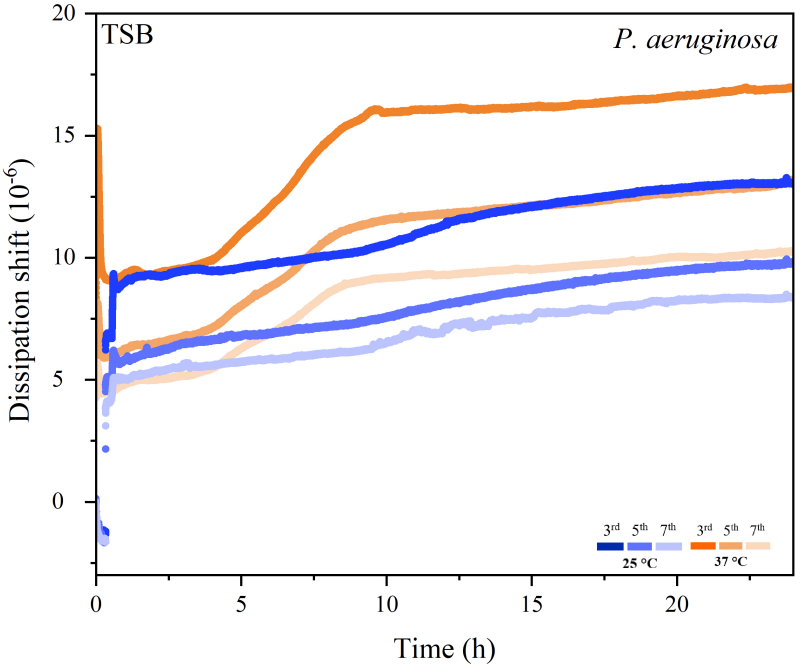

(b) Dissipation

Figure 3.28: Frequency, Δf, and dissipation, ΔD, QCM-D response to *P. aeruginosa* in TSB at 25 °C and 37 °C.

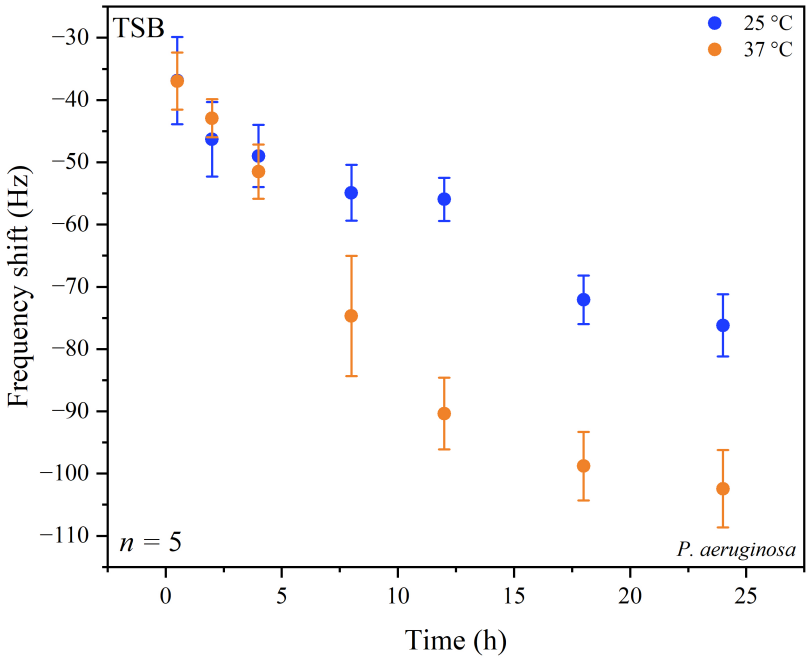

(a) Frequency

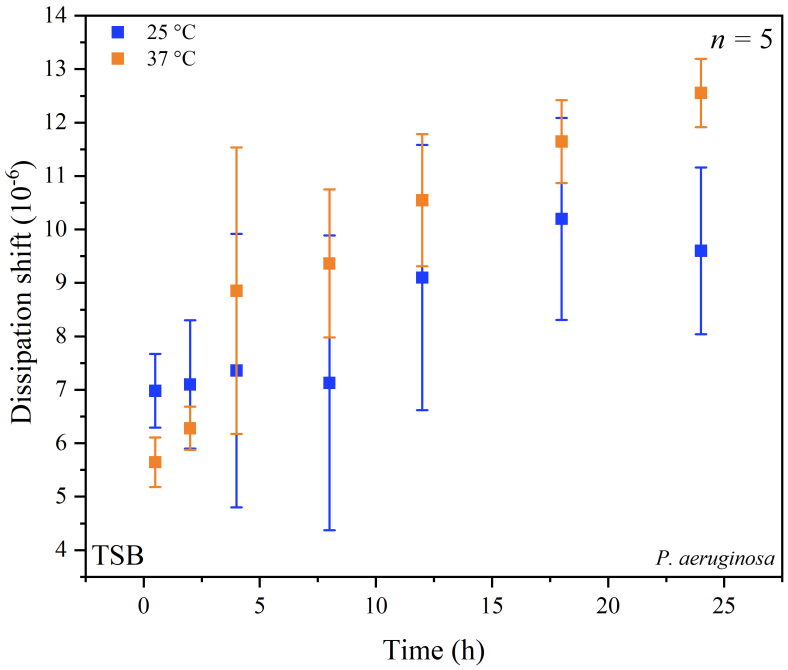

(b) Dissipation

Figure 3.29: Comparison of Δf and ΔD for *P. aeruginosa* in TSB over time at 25 °C and 37 °C. The middle, 5th, overtone is chosen for easier visualisation. The data represent the mean of at least three measurements calculated at the time points t = 0.5, 2, 4, 8, 12, 18, 24 h. The errors are standard deviations.

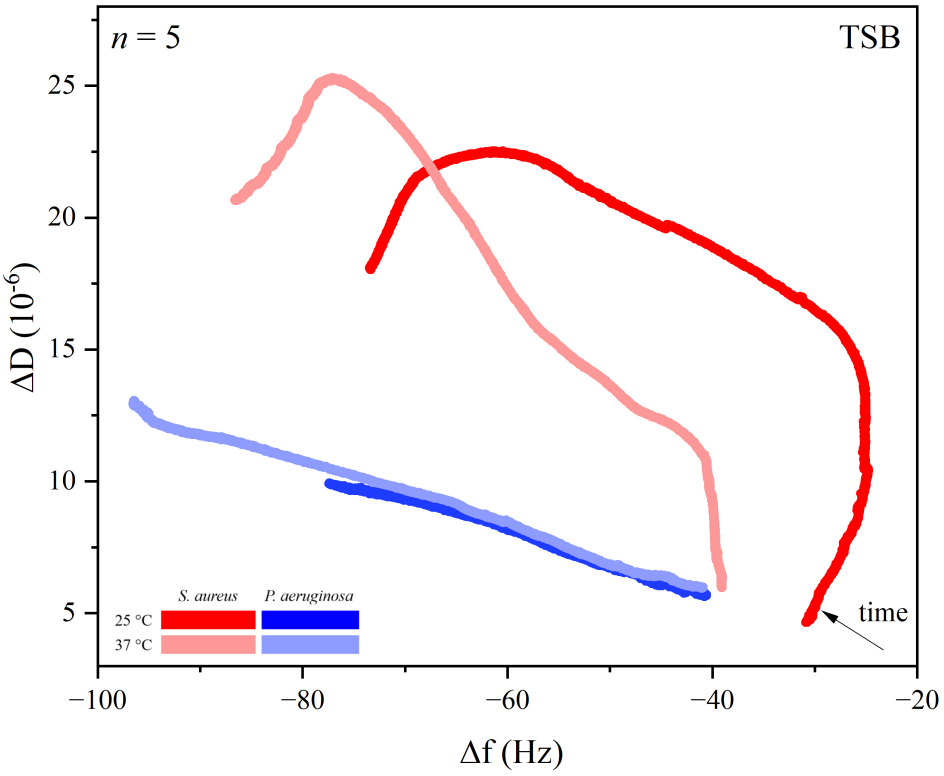

Figure 3.30: Dissipation versus frequency (Df) plots compared between *S. aureus* and *P. aeruginosa* in TSB at 25 °C and 37 °C.

bigger effect on *S. aureus* films, which can be deduced from the much greater differences in slope.

Interestingly, literature studies which explore the impact of temperature on biofilms suggest lower temperatures prompt the formation of more abundant and more stable biofilms, for both *S. aureus*[220] and *P. aeruginosa*.[221, 222] The differences in biofilm properties at varying temperatures can be attributed to the metabolic activities of the bacteria, which are influenced by temperature. At 37 °C, closer to the optimal growth temperature for these pathogens, bacteria might form biofilms more efficiently initially, but these films are less stable and less dense over time compared to those formed at 25 °C. This could be due to higher metabolic rates at 37 °C, leading to faster but less structured biofilm development.

At 25 °C, *S. aureus* displays a pronounced Δf peak at approximately 5 h, which shifts to around 2.5 h at 37 °C and is less marked. This transient peak, observed early in the adhesion process, is a reflection of the initial reversible binding phase. During this phase, the cells appear to reorganise their adhesion contacts, likely coinciding with the upregulation of adhesion molecules and the onset of EPS production, which ultimately leads to more stable, irreversible

binding [223]. In effect, the earlier peak at 37 °C indicates that the initial cell–surface interactions occur more rapidly at the higher temperature, accelerating the transition from reversible to irreversible adhesion, a finding consistent with studies reporting that elevated temperatures enhance metabolic activity and adhesion kinetics.[156, 224]

Despite these temperature-dependent differences in early adhesion kinetics, the overall dissipation data remain similar at both temperatures, with only minor variations during the initial stages (0.5, 2, and 4 h). This suggests that, although the rate of adhesion is accelerated at 37 °C, the viscoelastic properties of the mature biofilms converge over time. Furthermore, Df plots reveal that both *S. aureus* and *P. aeruginosa* form stiffer biofilm layers at lower temperatures. Notably, the differences are more pronounced for *S. aureus*, implying that at 25 °C the biofilms are denser and potentially more stable. This observation aligns with literature indicating that lower temperatures can promote the development of more abundant and stable biofilms.[156, 223]

Fig. 3.28 illustrates that *P. aeruginosa* exhibits a distinct two-step decrease in Δf at both 25 °C and 37 °C. This biphasic response is interpreted as reflecting a reorganisation or consolidation of the biofilm matrix, possibly due to changes in the interactions and cross-linking among EPS, and may also indicate the detachment or redistribution of cells within the developing biofilm. Notably, at 37 °C, the decrease in Δf occurs significantly earlier (around 5 h) compared to approximately 10 h at 25 °C, suggesting that elevated temperature accelerates the onset of irreversible adhesion and biofilm maturation.

The more rapid progression at 37 °C is likely linked to enhanced metabolic activity and faster EPS production, as documented by studies showing that higher temperatures facilitate quicker biofilm formation in *P. aeruginosa* [193, 218]. The dissipation data similarly display a two-step progression that is more pronounced at 37 °C, although larger error bars indicate some variability in the viscoelastic measurements. These observations imply that at elevated temperatures, *P. aeruginosa* transitions more swiftly through the various stages of adhesion and biofilm consolidation, forming a stiffer, more organised biofilm layer in a shorter timeframe. These temperature-dependent differences emphasise how environmental conditions modulate the biofilm formation process - a key theme in understanding the dynamic process of surface colonisation.

3.4 The viscoelastic and adhesive characteristics of green fluorescent protein labelled *S. aureus*

SH1000-GFP is a strain of *S. aureus* that has been genetically modified to express the Green Fluorescent Protein (GFP). The GFP, originally derived from the jellyfish *Aequorea victoria*, is

a widely used molecular marker due to its ability to fluoresce green under blue and near UV illumination, allowing easy visualisation and tracking of biological processes. In SH1000-GFP, the gene encoding GFP has been inserted into a plasmid, which is a small, circular piece of DNA that replicates independently of the bacterial chromosome. Studies have demonstrated that the introduction of the GFP plasmid into SH1000 has not adversely affected its growth kinetics, meaning that the SH1000-GFP strain grows comparably to the non-GFP SH1000 strain.[107] This characteristic makes SH1000-GFP particularly useful for studying biofilms, as the fluorescent labelling allows researchers to monitor biofilm formation and development in real time, providing valuable insights into the behaviour and properties of *S. aureus* in various environments.[225, 226]

Bacteria labelled with GFP containing plasmids present a powerful tool for visualising cells, facilitating the elucidation of attachment dynamics, spatial distribution, and biofilm formation on various substrates. GFP-labelled bacteria have clear advantages over traditional staining methods. Unlike staining techniques which often require cell fixation and can disrupt bacterial physiology, GFP labelling enables the observation of live bacteria within their natural environment, capturing dynamic processes such as cell division, motility, and interaction with host cells. Additionally, GFP-labelled bacteria offer enhanced specificity, as the fluorescent protein is genetically encoded and selectively expressed within the target bacterial strain, minimising background noise and facilitating precise localisation studies. In the context of biofilm studies, it is essential to consider the limitations of staining methods such as the commonly used live bacteria stain, SYTO9™. SYTO9™ may not penetrate biofilms evenly, resulting in uneven staining and potentially misleading imaging outcomes. Moreover, using higher concentrations of SYTO9™ to overcome these limitations can lead to toxicity, altering bacterial behaviour and confounding experimental results.[227] These drawbacks highlight the need to explore alternative imaging methods like GFP labelling, which not only offer superior specificity and real-time visualisation but also mitigate the challenges associated with staining techniques, particularly in biofilm imaging and high-throughput screening assays.

GFP-labelled SH1000-GFP strain was used because of its availability. However, its use also enables the QCM-D to be put to test in the comparison of two different commonly studied strains of *S. aureus*: SH1000-GFP and the strained studied previous sections, ATCC 6538™. ATCC 6538™ is a well-established strain in microbiological research, often used as a standard for testing disinfectants and studying the evolution of antimicrobial resistance due to its historical isolation prior to widespread antibiotic use.[228, 229] It is characterised by its typical microbial and pathological traits representative of most *S. aureus* strains, making it a reliable model for generalisable studies. SH1000 is derived from the 8325-4 strain with a repaired rsbU gene, which restores normal stress response. This restoration influences the expression of various virulence factors, which has made it a valuable strain for studying the regulatory mechanisms underlying these processes. [230] Comparing these two strains is valuable due to their distinct genetic

backgrounds and phenotypic traits. Mainly, SH1000's engineered auxotrophy for menadione (vitamin K_3) and hemin (iron-containing porphyrin with chlorine) differentiate it from ATCC 6538™, which does not share these auxotrophic requirements. No literature examples have been found of direct discussion of differences between the two strains, however studies use both strains in larger studies as examples of Gram-positive bacteria[231] as well as using SH1000-GFP for its fluorescent ability in imaging.[232]

The focus in this section on the bacterial behaviour in TSB is motivated by the interest in biofilm formation. TSB provides a nutrient rich environment conducive to robust biofilm development, offering an ideal environment for studying the intricate interplay between the bacterial adhesion, colonisation, and biofilm maturation processes. This section incorporates data from QCM-D experiments, biomass assays and fluorescent microscopy imaging. Through this multifaceted approach, the mechanisms underlying bacterial adhesion and biofilm development are elucidated, shedding light on the complexities of bacterial behaviour.

3.4.1 QCM-D monitoring of GFP-labelled *S. aureus*

The QCM-D frequency response to TSB (without cells), seen in Fig. 3.31a shows that, following an initial 20 minute signal stabilisation in PBS only, the frequency to gradually decreases throughout to reach -65.6 Hz at 24 h for the 3rd overtone (n = 5: -60.8 Hz, n = 7: -57.1 Hz). The green curves corresponding to the frequency response to SH1000-GFP in TSB is markedly different to the TSB-only reference. The signal is initially stabilised in PBS and then in TSB, for 10 minutes each. The presence of cells results in a peak at $\approx$ 4 h, followed by a swift decrease in frequency to ultimately almost double the value of the 3rd overtone to -127.6 Hz (n = 5: -121.3 Hz, n = 7: -117.7 Hz). This shows that the results have contributions from both cells and medium interactions. Importantly, the frequency response with cells displays a characteristic profile. The absence of the peak in the TSB-only sample confirms that this feature is exclusively due to bacterial interaction.

Similarly, the dissipation data seen in Fig. 3.31b yields much higher values for SH1000-GFP compared with the TSB-only reference measurement. Following the PBS only 10 min baseline, the culture media result shows a rapid increase and stabilisation within $\approx$ 1 h to reach n = 3 of 10.5 $\times$ 10^{-6} at 24 h (n = 5: 8.1 $\times$ 10^{-6} , n = 7: 7.1 $\times$ 10^{-6}). The cell sample, however shows a stepwise increase up to 15 h, followed by a gradual decrease, which has been previously attributed to increased stiffness of arising from the reorganisation of the bacterial cytoskeleton and/or readjustment of the surface proteins towards establishing a stronger adhesive contact.[175, 189] The higher dissipation values reached (n = 3: 37.9 $\times$ 10^{-6}, n = 5: 23.9 $\times$ 10^{-6}, n = 7: 19.9 $\times$ 10^{-6}) reveal the higher viscoelasticity of the layer arising due to cell interaction with the Au surface.

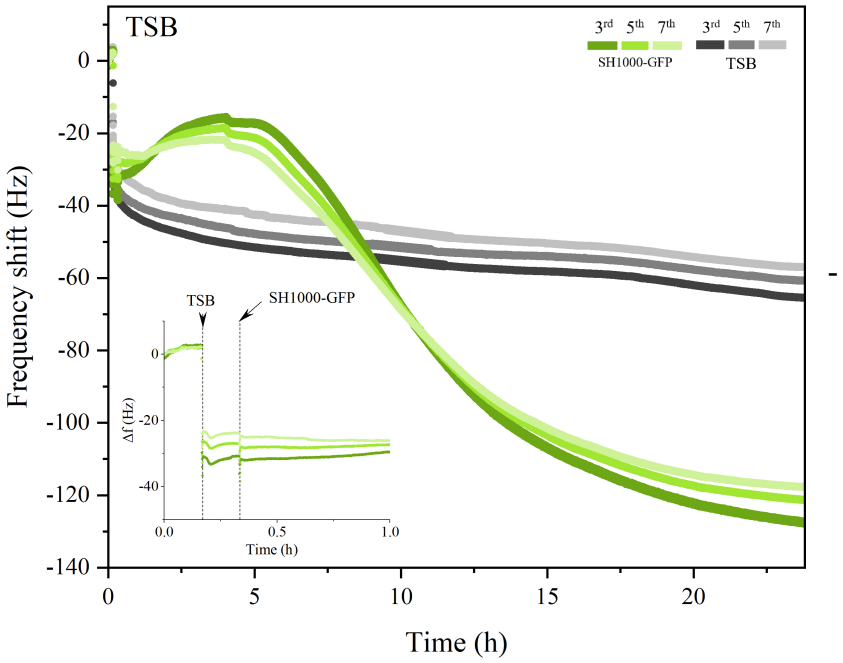

(a) Frequency

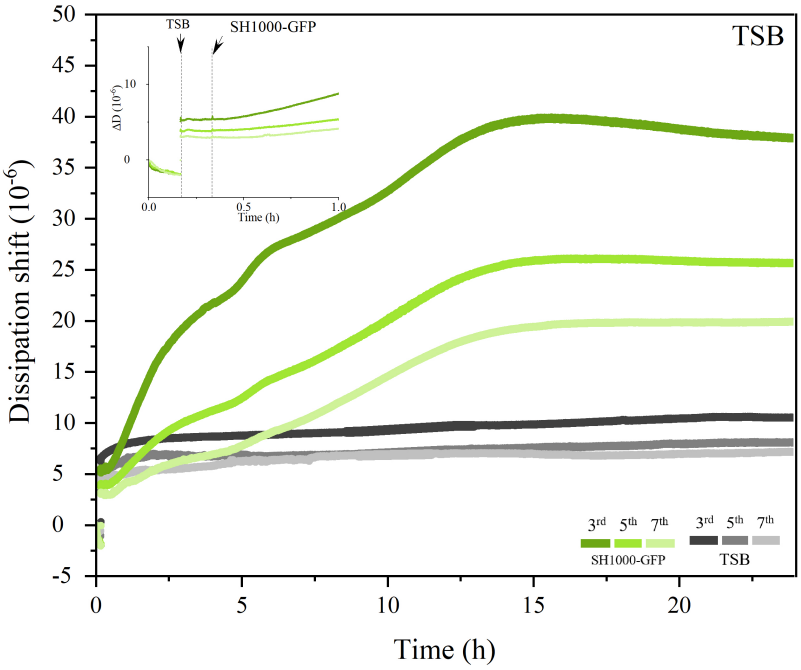

(b) Dissipation

Figure 3.31: Time-dependent frequency, Δf, and dissipation, ΔD, response of gold-coated QCM-D substrate to SH1000-GFP *S. aureus* in TSB medium. A reference measurement in pure is TSB included.

3.4.2 Comparing surface colonisation of two *S. aureus* strains

Fig. 3.32 shows the reproducibility of the QCM-D data acquired for the SH1000-GFP strain, and allow for comparison with ATCC 6538™. The Δf data are initially be similar. The distinctive positive peak is present in each sample, and the values are comparable. However, there is a divergence in the results which can be seen at the 12 h mark, where Δf decreases more rapidly for the SH1000-GFP cells, giving rise to much lower final Δf values. Similarly, the dissipation data are similar at first, up to 4 h, at which point the dissipation reached is lower for the SH1000-GFP cells. Following this, the dissipation reaches similar values at $t = 12$h, followed by a steeper decline in the ATCC 6538™strain to ultimately reach lower values at $t = 24$ h.

The results for the two *S. aureus* strains are alike in shape, which conveys similarities in how the cells interact with the surface. The averaged data show a very similar Δf progression up to 8 h, including the ≈ 5 h peak. The ΔD data are also close in magnitude throughout the experiment. This is contrast with the comparative plot of *S. aureus* and *P. aeruginosa* (Fig. 2.1), which shows distinct behaviours in both Δf and ΔD in both shape and magnitude.

Fig. 3.33 shows the dissipation change versus the frequency shifts during *S. aureus* interaction with Au. Initially, the slopes are similar as the Δf becomes more positive. As the frequency starts decreasing, two distinct evolutions with time are observed. The slope is lower for the SH1000-GFP cells, indicating a stiffer cell layer or a more organised cytoskeleton. Both experiments show a curve which corresponds to the decrease in dissipation during the later stages of the experiment, however it is much more pronounced in the non-fluorescent cells.

The findings from the crystal violet assay (Fig. 3.34) serve as a means to assess the degree of bacterial colonisation on a substrate, and has been used to compare between differing bacterial strains.[233] The OD measurement obtained reflects the quantity of biomass adhered to the surface. The outcomes indicate a substantial contrast, with approximately three times as much surface-attached biomass observed for the GFP-labelled cells. This suggests that SH1000-GFP forms denser or more extensive biofilms, possibly due to its genetic modifications and nutrient requirements. This also shows that, in this instance, the lower the frequency, the higher the relative biomass. The difference in biomass suggests that SH1000-GFP more readily colonised the QCM-D disc. However, similar dissipation results point to a similar viscoelasticity of the samples. The similar viscoelasticity observed despite differences in biomass indicates variations in biofilm structure, such as cell packing density or EPS composition.

Some differences arise between the two *S. aureus* strains, chiefly in magnitude, rather than behaviour. The differences in their genetic background might result in variations in the expression of genes involved in cell wall synthesis, biofilm formation, metabolic differences and stress responses, leading to distinct phenotypic outcomes. For examples, SH1000-GFP's auxotrophy for menadione, an important co-factor in oxidative stress management, might lead to increased

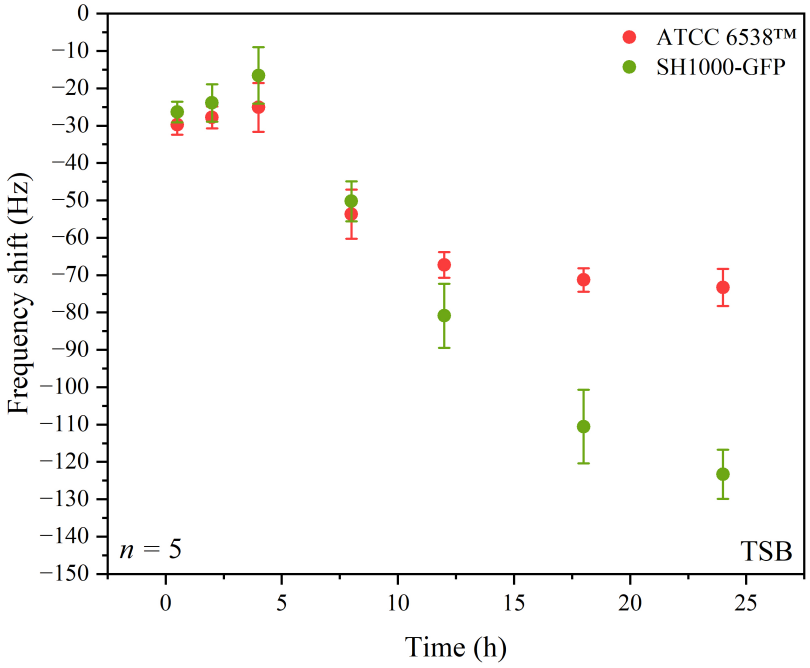

(a) Frequency

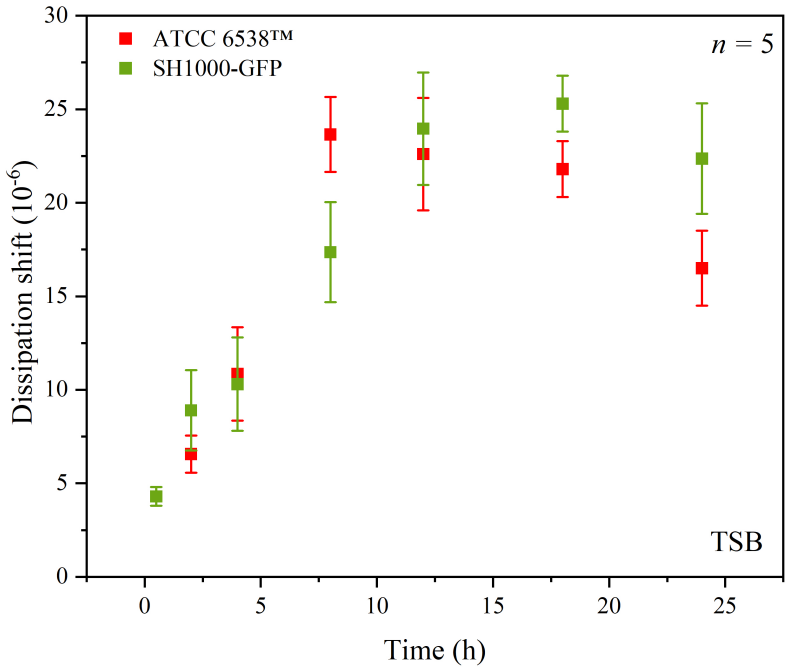

(b) Dissipation

Figure 3.32: Comparison of Δf and ΔD for ATCC 6538™and SH1000-GFP in TSB over time. The middle, 5th, overtone is chosen for easier visualisation. The data represent the mean of at least three measurements calculated at the time points t = 0.5, 2, 4, 8, 12, 18, 24 h. The errors are standard deviations.

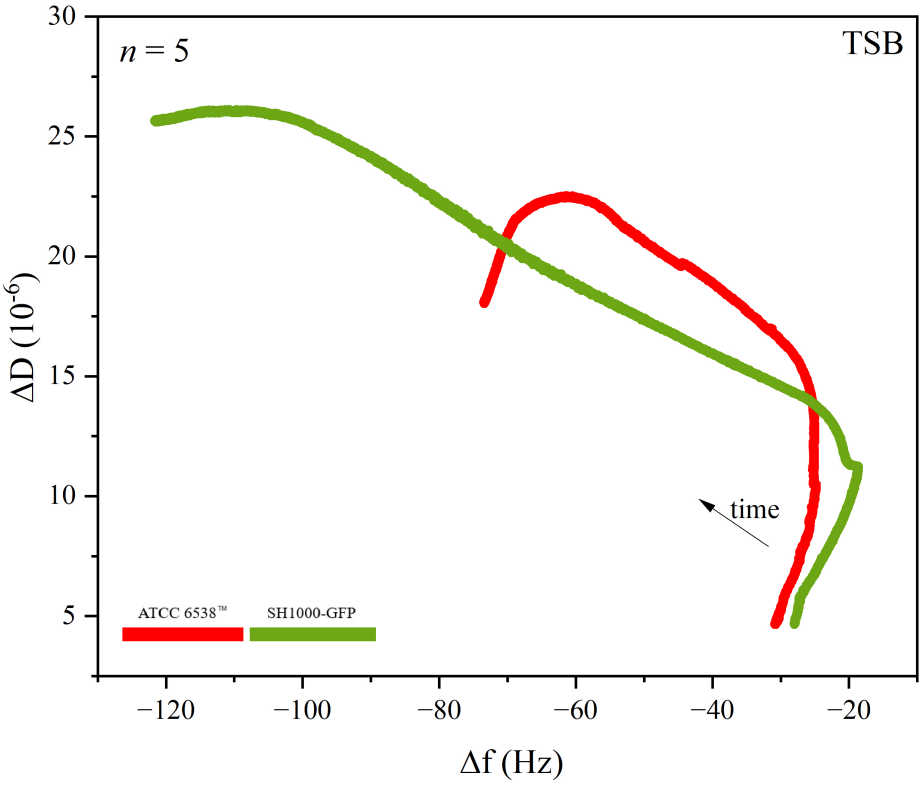

Figure 3.33: Dissipation versus frequency (Df) plots compared between ATCC6538™and SH1000-GFP in TSB.

sensitivity to oxidative stress, affecting its biofilm formation and stability. Hemin is a source of iron, essential for many cellular processes. SH1000-GFP's need for hemin supplementation might impact its ability to manage iron-related stress, influencing biofilm formation and bacterial adhesion properties. In the absence of menadione and hemin in TSB, SH1000-GFP might be expected to exhibit slower growth rates or lower biomass production compared to its growth in supplemented media. This, however, is in contrast with the differences observed in the crystal violet biomass assay, where SH1000-GFP showed higher biomass amounts compared to ATCC 6538™. Additionally, the characteristic profile of SH1000-GFP, shows a more pronounced frequency peak and higher dissipation values, suggests that they are actively engaging with the surface. A possible reason for this is that the lack of menadione and hemin lead to stress responses that promotes biofilm formation at a cost of ideal architecture. The cells are expected to prioritise survival mechanisms, leading to biofilms with different structural properties compared to those formed in the presence of these nutrients. This could mean their biofilm is less stable or differently structured compared to the non-auxotrophic ATCC 6538™. The differences in viscoelastic properties of the biofilms as indicated by QCM-D data could be due to the resulting variations in biofilm composition, such as the ratio of cells to EPS or the organisation of the

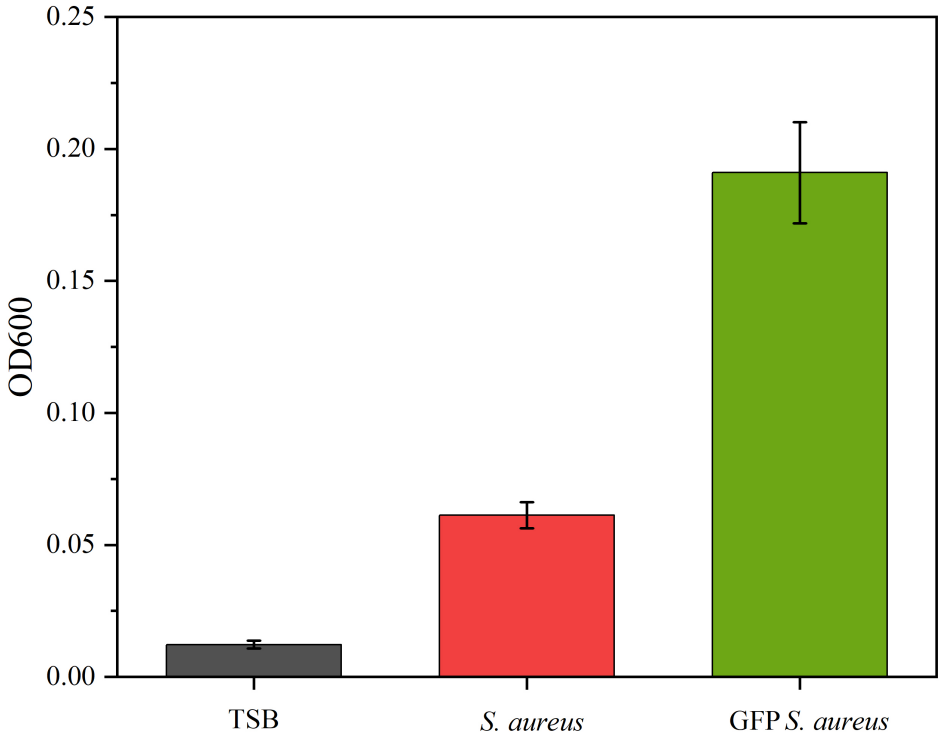

Figure 3.34: Crystal violet biomass assay of two *S. aureus* strains, ATCC 6538™and SH1000-GFP, on gold. The experiment was conducted on QCM-D crystal in well plates, with the QCM-D experimental conditions reproduced. The data represent the mean of at least three measurements at $t = 24$ h. The errors are standard deviations.

bacterial cells within the biofilm matrix.

3.4.3 Fluorescence microscopy imaging of GFP-labelled *S. aureus* on gold

An invaluable advantage of utilising a GFP-labelled, SH1000-GFP, strain is the ease of conducting fluorescent microscopy imaging of cells adhered to a surface. The images depicted in Fig. 3.35 exhibit cells attached to the Au sensor at $t = 30$ min. This choice ensures that bacterial attachment processes have advanced sufficiently to be observable. By capturing images at this juncture it becomes possible to observe the initial interactions between bacteria and the substrate, thereby gaining insights into cell-surface distribution just before the commencement of bacterial proliferation. The visualisation of surface-associated cells at this nascent stage serves as confirmation of the discrepancy observed in the QCM-D data between the cell sample and the media-only reference being attributable to bacterial interaction with the sensor. The findings unequivocally indicate cell attachment at 30 min. Notably, a distinct propensity for group

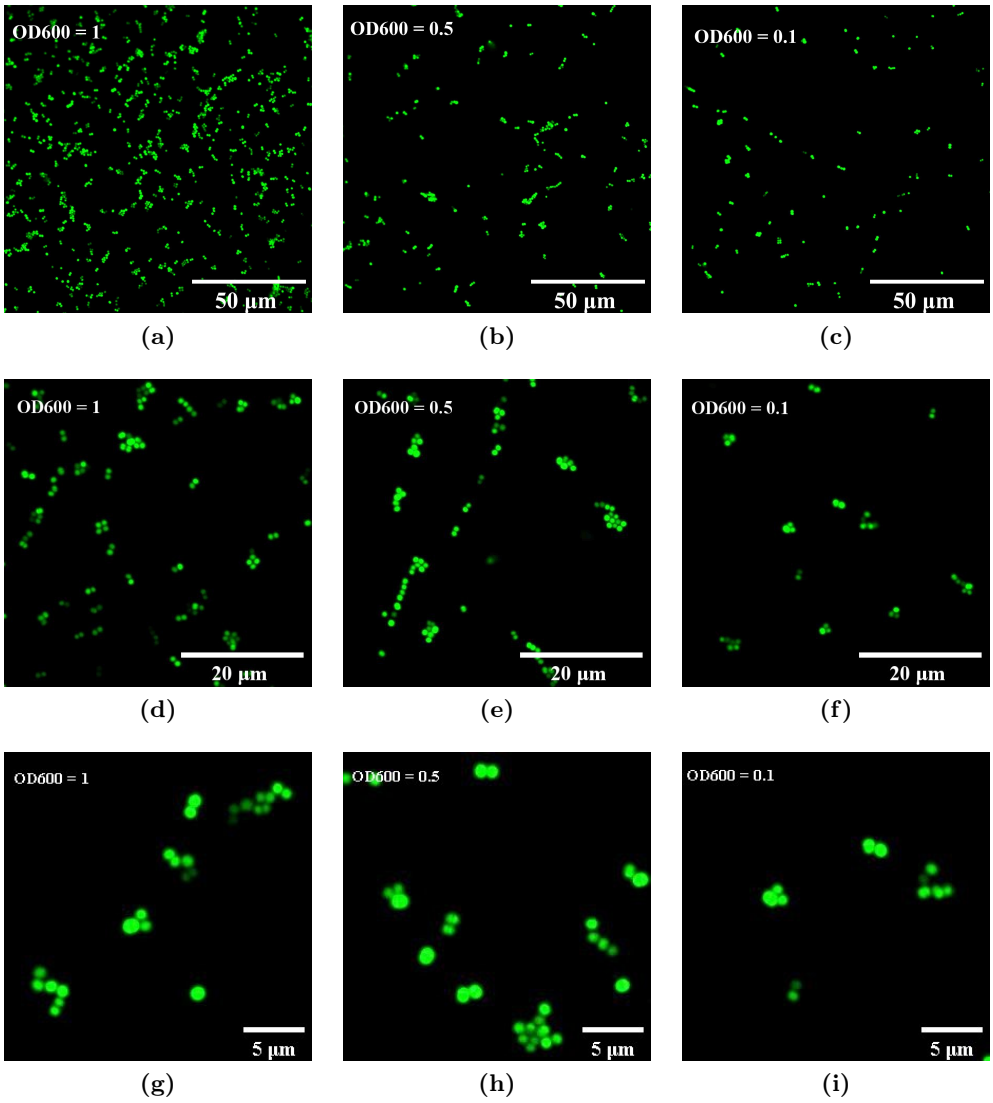

Figure 3.35: Fluorescence microscopy images of GFP *S. aureus* after 30 minutes of incubation on gold in TSB. OD600 = 1. Results can be seen in (a), (d) & (g), OD600 = 0.5 in (b), (e) & (h), OD600 = 0.1 in column (c), (f) & (i). Sizes of images are as follows: 135 μm × 135 μm for (a)-(c), 50 μm × 50 μm for (d)-(f) and 25 μm × 25 μm (g)-(i).

attachment is evident, with individual cells absent. This effect can also be seen in the higher (OD600 = 1) and lower cell concentration (OD600 = 0.1) images. Although the higher the cell concentration, the more surface-attached cells can be seen, group attachment is ubiquitous across the varying conditions. This shows the propensity for group attachment, and therefore intercellular communication, occurs even at the earliest stages of biofilm formation.

Bacteria often preferentially attach to surfaces as groups or clusters rather than as individual cells. This phenomenon, known as microcolony formation, can enhance bacterial adhesion by facilitating cooperative interactions and the accumulation of EPS. Bacteria within a group may engage in quorum sensing or other forms of cell-to-cell communication, coordinating their attachment behaviours and gene expression patterns. This communication can lead to synchronised adhesion events and the formation of structured bacterial communities of attached bacteria. Grouped attachment of cells is often an early step in biofilm formation, where initial bacterial adhesion events pave the way for subsequent growth and maturation of the biofilm structure. Observing microcolonies at the 30-minute mark suggests that the bacteria are initiating the biofilm formation process.

3.5 Impact of quorum sensing inhibitor on *S. aureus*

Biofilms are regulated by quorum sensing, a process by which microorganisms communicate and coordinate their behaviour in response to population density. This communication occurs through the production and detection of signalling molecules known as autoinducers. As the concentration of these molecules increases with cell density, they bind to specific receptors that trigger changes in gene expression. This leads to the production of EPS' that form the structural matrix of the biofilm, providing a protective environment for the bacterial community.

Central to the pathogenicity of *S. aureus* is the accessory gene regulator (*agr*) system, a quorum sensing mechanism that modulates the expression of numerous virulence factors. The *agr* system, through its autoinducing peptides (AIPs) and the response regulator AgrA, coordinates the expression of toxins, enzymes, and other virulence genes that contribute to the bacterium's ability to cause infections. This system also plays a crucial role in biofilm formation and dispersal, making it a critical target for anti-virulence strategies.

Savirin (short for (Staphylococcus aureus virulence inhibitor) (Fig. 3.36) is a small synthetic molecule identified as a selective *agr*-QS inhibitor[234]. Mechanistically, savirin binds to AgrA's DNA-binding domain, blocking its transcriptional activity. By preventing AgrA from activating target promoters, savirin effectively shuts down *agr*-mediated QS, halting the upregulation of *agr*-controlled genes. Unlike antibiotics, savirin doesn't significantly affect *S. aureus* growth in exponential phase, instead, it renders the bacteria less virulent by keeping the QS system

inactive. This targeted mode of action means *S. aureus* behaves as if in a perpetual "low cell density" state even at high population, which can impact biofilm formation and structure.

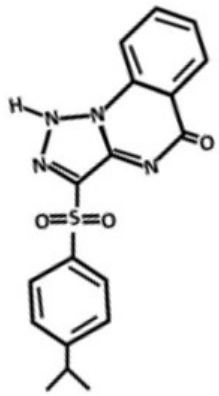

Figure 3.36: The chemical structure of savirin (3-(4-propan-2-ylphenyl) sulfonyl-1H-triazolo [1,5-a] quinazolin-5-one).

Savirin has shown significant potential in preventing and treating biofilm-related *S. aureus* infections. In rodent models of skin and subcutaneous infections, savirin was effective in reducing bacterial load and biofilm formation without exhibiting toxicity at concentrations of 5 μg/mL. Despite these promising results, the exact molecular mechanisms by which savirin exerts its effects remain unclear. It is hypothesised that savirin's inhibition of the *agr* system leads to a broader downregulation of genes associated with biofilm formation and virulence.

The antibiofilm efficacy of savirin has been evaluated using various in vitro assays, consistently demonstrating its ability to disrupt biofilm formation and maintenance; however, information on its efficacy in continuous, non-invasive observation of biofilm dynamics is lacking. Techniques such as QCM-D offer a valuable approach to assess the time-resolved impact of savirin on biofilm formation and stability. Current studies highlight savirin's potential as a quorum sensing inhibitor and antibiofilm agent, but further research is needed to fully elucidate its mechanism of action. Future investigations should focus on employing non-disruptive methods like QCM-D to gain deeper insights into the temporal aspects of biofilm inhibition by savirin, paving the way for more effective anti-biofilm strategies against *S. aureus*.

A single QCM-D study that examined the impact of a QSI (4-nitropyridine-N-oxide (4-NPO)) on bacterial adhesion was identified. This chemical, attached to surfaces, was utilised to neutralise bacterial charge and reduce bacterial deposition. However, it was observed that the quorum-sensing abilities of 4-NPO were unlikely to influence the outcome due to the bacteria's low density in this study (OD600 of 0.01).[234] Another study involved a QSI-antibiotic combination, applied at the end of the experiment, to established biofilms.[199] There were no studies found that employed QCM-D to track QSI during the development of biofilms, indicating that

the research discussed here introduces a unique method for using QCM-D to explore biofilm dynamics.

To examine the effects of savirin on biofilm formation, this quorum sensing inhibitor should be added to the bacterial inoculum right before the start of the QCM-D experiment. The outcomes can be compared with earlier data obtained without savirin, serving as a control. Should savirin affect the biofilm, changes in both frequency and dissipation will be observed by QCM-D. A disruption in the biofilm structure by savirin will be indicated by changes in frequency and dissipation, suggesting a reduction in mass due to biofilm detachment and changes in viscoelastic properties, which implies alterations in the rigidity of the biofilm. The experiments were carried out in TSB to promote quick surface colonisation and biofilm development, using a GFP-tagged SH1000-GFP *S. aureus* strain for both fluorescence microscopy and QCM-D monitoring. To assess the impact of savirin, it was added post-preparation of the cell culture, just before initiating the QCM-D experiments. Continuous monitoring for 24 hours using QCM-D and initial adhesion evaluation via fluorescence imaging was carried out to elucidate the effectiveness of savirin in hindering biofilm formation.

3.5.1 QCM-D monitoring of quorum sensing inhibitor effect on bacterial colonisation

To investigate savirin's effect on biofilm development, QCM-D was used to monitor *S. aureus* attachment and biofilm growth on a gold surface, with and without savirin. Without savirin (Fig. 3.31), the QCM-D profile showed a pattern of biofilm maturation characteristic to *S. aureus*. An initial Δf peak as bacteria attached reversibly then a rapid Δf drop as they attached irreversibly, as well a gradual, sustained increase in dissipation as the biofilm matrix accumulated. The *Df* plot for untreated samples was predominantly a roughly linear trajectory with a steady rise in ΔD after the first few hours, consistent with continuous deposition of EPS and a gradual stiffening of the biofilm matrix as the biofilm becomes more rigid as it grows.

The *agr* quorum-sensing system of *S. aureus* typically activates in late exponential phase (around 5–7 hours of growth)[156]. This activation coincides with a critical shift in biofilm development. The transition from initial reversible attachment to a more stable, irreversible stage. In the QCM-D experiments without savirin, a clear frequency inflection is observed at approximately 5 hours, marking the switch from weak to strong adhesion. Notably, in the presence of savirin, a similar Δf peak is delayed until around 7 hours, indicating that the onset of irreversible attachment is postponed[235]. The timeline of the *S. aureus* TSB experiment suggests that around 5 h, the bacteria transition from a reversible adhesion phase to an EPS-secreting, irreversible biofilm growth phase. This is supported by the disappearance of the transient Δf peak and the start of a steady mass increase (frequency decline) thereafter. It is at this juncture that quorum sensing *agr* would typically activate, orchestrating biofilm maturation genes[156].

Consequently, savirin delays or disrupts this transition, the treated cells remain longer in a state of early adhesion or less cohesive biofilm, as evidenced by the later and smaller frequency shifts observed. Savirin likely keeps the bacteria in an earlier, microcolony, stage for longer, preventing the normal QS-driven maturation.

In contrast, savirin-treated samples exhibited markedly different QCM-D dynamics (Fig. 3.37 and Fig. 3.38). The presence of savirin led to higher ΔD values at certain time points, even for similar Δf, indicating a more viscoelastic) biofilm layer. Notably, two pronounced dissipation peaks were observed (around $\approx$ 6.5 hours and $\approx$ 17 hours) in savirin-treated biofilms. These peaks occurred slightly after corresponding drops in frequency, meaning that after the initial cell attachment phases, the biofilm's mechanical properties underwent major changes. The first peak ($\approx$ 6.5 h) suggests that as cells initially attached in the presence of savirin, they formed a very soft, loosely attached layer (high ΔD) compared to control. The second ΔD peak ($\approx$ 17 h) and the subsequent decline in dissipation imply that the biofilm became more rigid again later in development. One interpretation is that, with quorum sensing inhibited, the bacteria initially fail to produce a well-structured matrix, resulting in a flimsy, hydrated layer (hence high dissipation). Over time, however, the cells may adapt by reinforcing their attachment (e.g. strengthening cell-surface contacts or cell wall structure), which increases the stiffness of the cell layer and lowers dissipation after 17 h. In essence, QS inhibition by savirin disrupts the normal progression of biofilm mechanical properties, leading to a biofilm that is initially more fluid-like and later comprised of possibly stress-adapted, harder cells rather than a robust EPS-rich matrix.

The *Df* plots (Fig. 3.39) further highlight these differences. For untreated *S. aureus*, the *Df* plot showed a smooth upward slope, indicative of coupled mass increase and dissipation, typical of a growing biofilm accumulating biomass and EPS. With savirin, however, the slope and shape of this trajectory changed significantly. Instead of a steady rise, savirin-treated fingerprints had inflection points and a steeper slope at early times (high ΔD for a given Δf), reflecting that each unit of attached biomass introduced disproportionately high dissipation. This suggests that the attached cells with savirin contribute less to rigid structure, due to inhibited QS-regulated matrix production, and more to a viscous, damping layer. Only later does the fingerprint trend indicate increased rigidity. Such changes imply that quorum sensing inhibition alters not only the quantity of biofilm formed but its material characteristics, savirin drives the biofilm to develop along a different physical path, likely with less EPS and more cellular adjustment. These findings align with the idea that disrupting *agr*-mediated signalling can weaken the biofilm's structural integrity, making it less resilient and more prone to mechanical perturbation[236, 237].

Fluorescent images (Fig. 3.40) taken 30 minutes after inoculation, at same bacterial concentration AS QCM-D experiments, show significantly greater surface coverage by *S. aureus* in the presence of savirin compared to the untreated samples. Noticeably fewer bacteria are

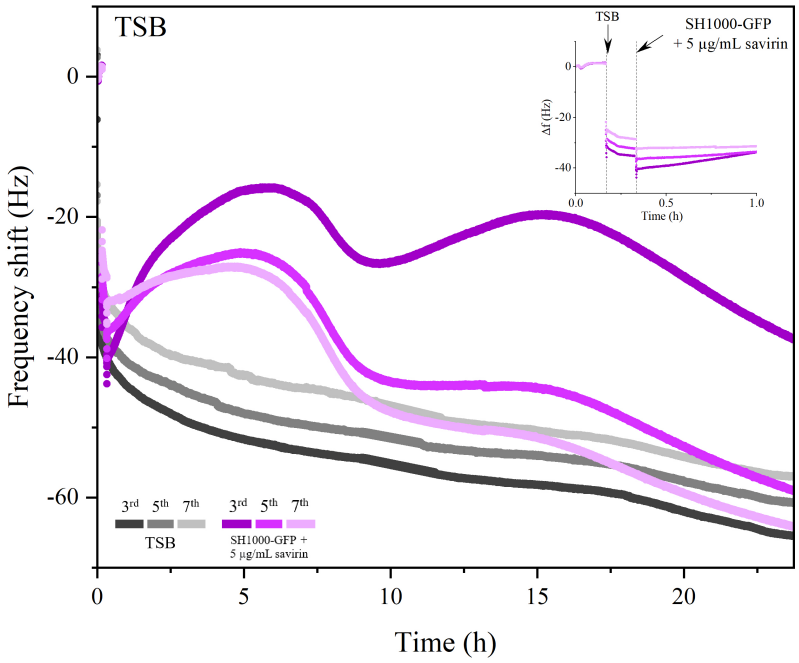

(a) Frequency

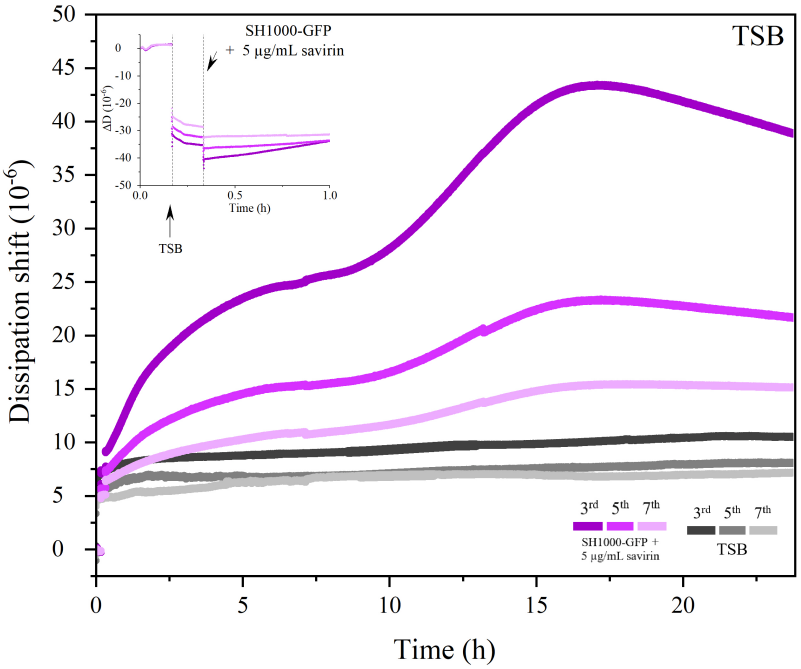

(b) Dissipation

Figure 3.37: Time-dependent frequency, Δf, and dissipation, ΔD, response of gold-coated QCM-D substrate to SH1000-GFP *S. aureus* and quorum sensing inhibitor, savirin (5 μg/mL), in TSB medium. A reference measurement in pure TSB is included.

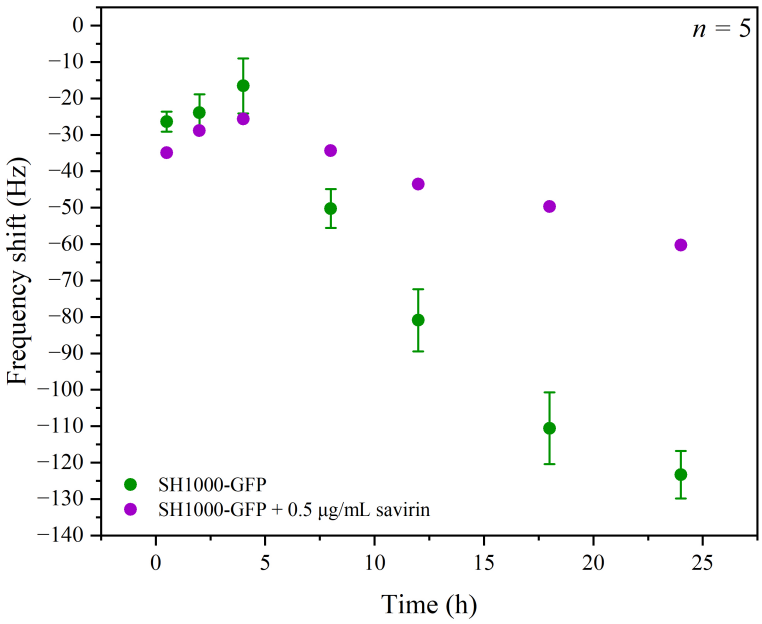

(a) Frequency

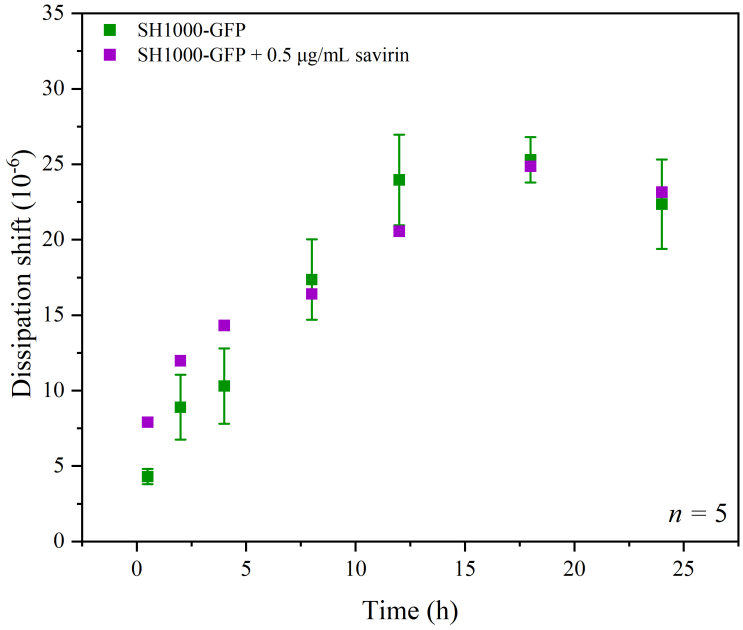

(b) Dissipation

Figure 3.38: Comparison of Δf and ΔD for SH1000-GFP and SH1000-GFP with savirin (5 μg/mL) in TSB over time. The middle, 5th, overtone is chosen for easier visualisation. The data without savirin represent the mean of at least three measurements calculated at the time points t = 0.5, 2, 4, 8, 12, 18, 24 h. The errors are standard deviations. The data with savirin are the average of two measurements.

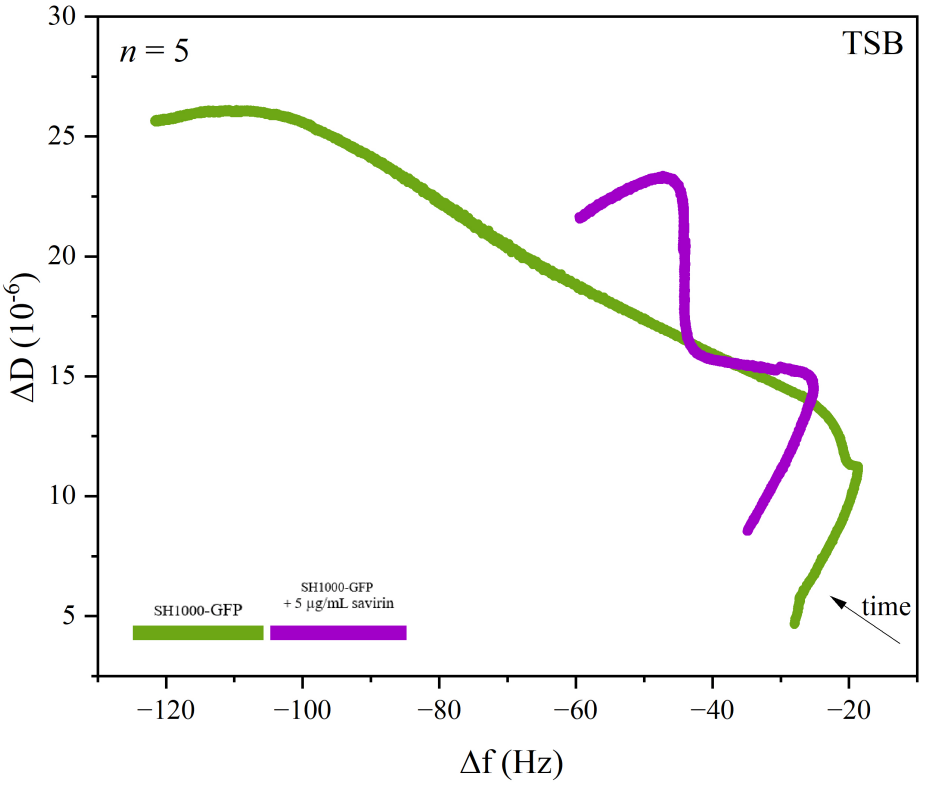

Figure 3.39: Dissipation versus frequency (Df) plots compared between SH1000-GFP and SH1000-GFP with savirin (5 μg/mL) in TSB.

attached to the surface when savirin is absent, indicating that savirin actually enhances early cell adhesion. In fact, this is the case for all tested inoculum densities (Fig. 3.43 and Fig. 3.42) as savirin-treated samples consistently exhibit higher initial adhesion than their untreated counterparts. This counterintuitive increase in early attachment likely results from the delayed quorum-sensing response: at low cell densities when *agr* would not yet be fully activated, savirin's suppression of *agr* prolongs the production of adhesion factors (and postpones detachment signals), allowing more bacteria to stick to the surface initially. *agr* mutants often show enhanced biofilm formation in static assays[238]. The crystal violet biofilm assay (Fig. 3.41) supports this trend as well, showing greater attached biomass in savirin-treated samples during the initial adhesion phase, relative to controls, consistent with the microscopy observations.

Notably, once the bacterial population grows and quorum-sensing cues would normally kick in, the untreated biofilms transition into a robust, multilayered state with abundant matrix, whereas the savirin-treated biofilms remain as a flatter, monolayer-like cell layer with delayed and limited matrix development[156, 195]. Ultimately, although more cells may adhere initially with savirin, the biofilm they form is less cohesive: it lacks the extensive EPS scaffolding and

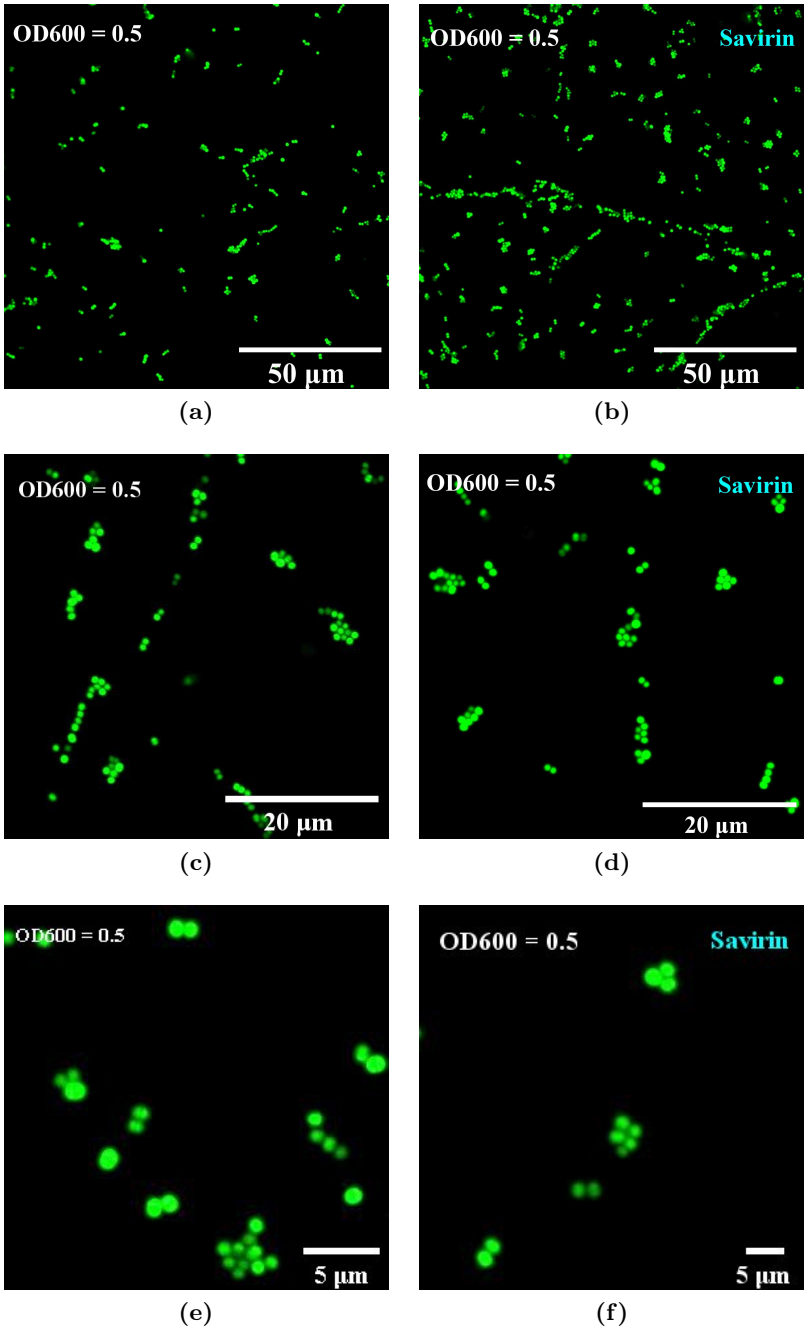

Figure 3.40: Fluorescence microscopy images of SH1000-GFP *S. aureus* at OD600 = 0.5 after 30 minutes of incubation on gold in TSB. Right hand side images ((b), (d), (f)) show results for bacterial attachment in the presence of savirin (5 μg / mL). For comparison, left hand side images ((a), (c), (e)) show images of bacteria attaching in the absence of savirin. Sizes of images are as follows: 135 μm × 135 μm for (a)-(b), 50 μm × 50 μm (c)-(d) and 25 μm × 25 μm for (e)-(f).

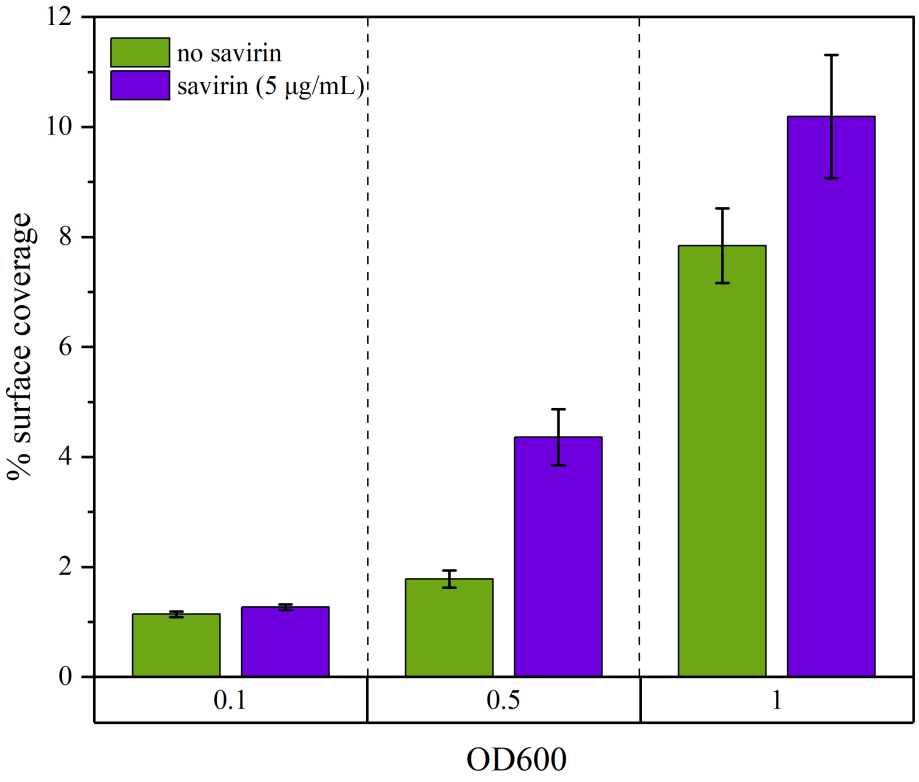

Figure 3.41: Percentage coverage of the Au surface by SH100-GFP with and without savirin calculated for the 135 μm $\times$ 135 μm images. The results are the means of at least 3 images, and the error bars are standard deviations.

channel architecture of a typical *S. aureus* biofilm, rendering it more fragile and easier to disrupt[239, 240]. Thus, savirin's impact can be seen as shifting the biofilm profile, front-loading cell attachment at early times, but markedly hindering the later maturation and structural reinforcement of the biofilm. This dual effect, enhanced initial adhesion but impeded biofilm development, is crucial for accurately understanding savirin's antibiofilm activity. The combination of techniques demonstrates that quorum sensing inhibition by savirin not only changes the molecular regulation of biofilm components but also has measurable physical consequences: faster initial colonisation and an unstable biofilm. These findings are in line with other studies reporting that savirin-treated *S. aureus* shows diminished biofilm accumulation and gene expression changes in biofilm-related pathways. For example, Pant *et al* found savirin exposure down-regulated key biofilm genes[237]. Such genetic effects would translate to less production of extracellular polysaccharides and adhesins, corroborating the reduced matrix formation seen in the experiments.

Several mechanisms help explain the delayed biofilm maturation observed with savirin treat-

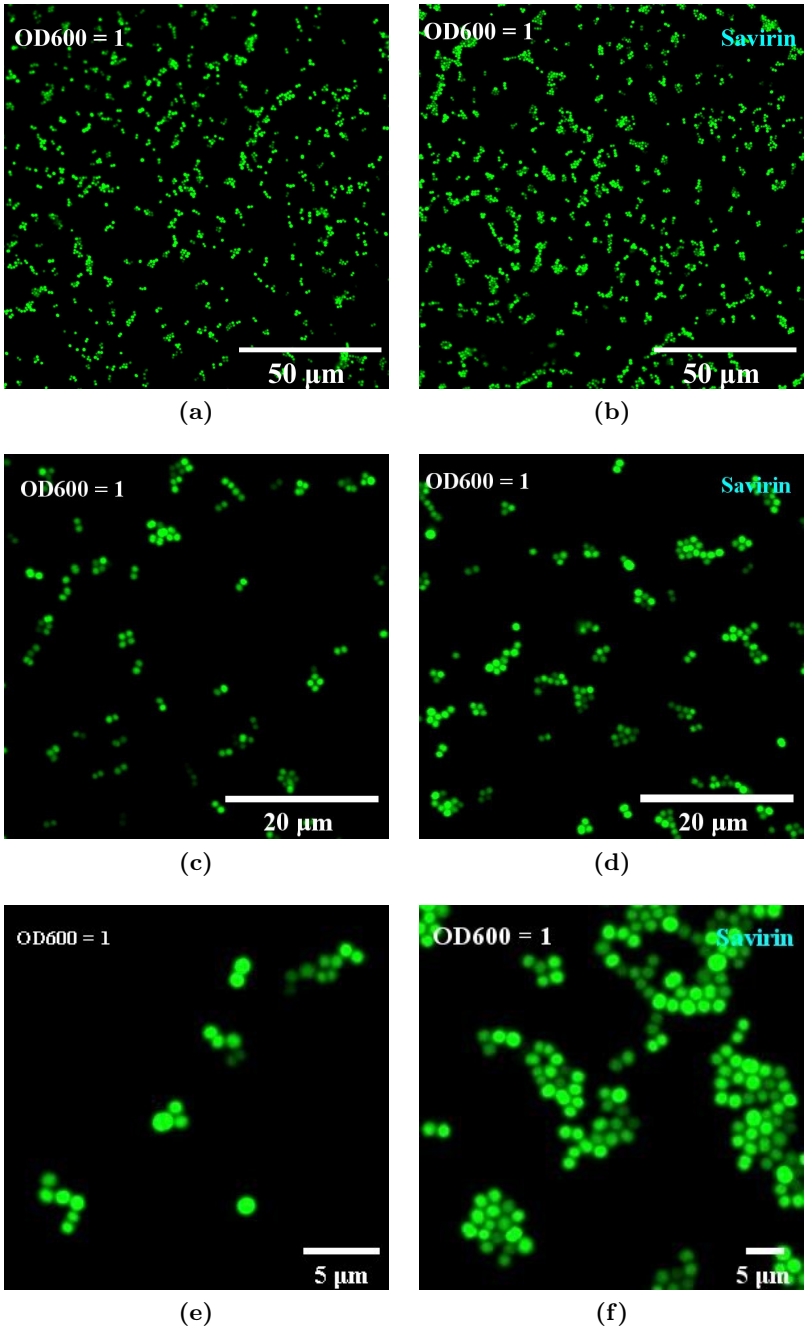

Figure 3.42: Fluorescence microscopy images of SH1000-GFP *S. aureus* at OD600 = 1.0 after 30 minutes of incubation on gold in TSB. Right hand side images ((b), (d), (f)) show results for bacterial attachment in the presence of savirin (5 μg / mL). For comparison, left hand side images ((a), (c), (e)) show images of bacteria attaching in the absence of savirin. Sizes of images are as follows: 135 μm × 135 μm for (a)-(b), 50 μm × 50 μm (c)-(d) and 25 μm × 25 μm for (e)-(f).

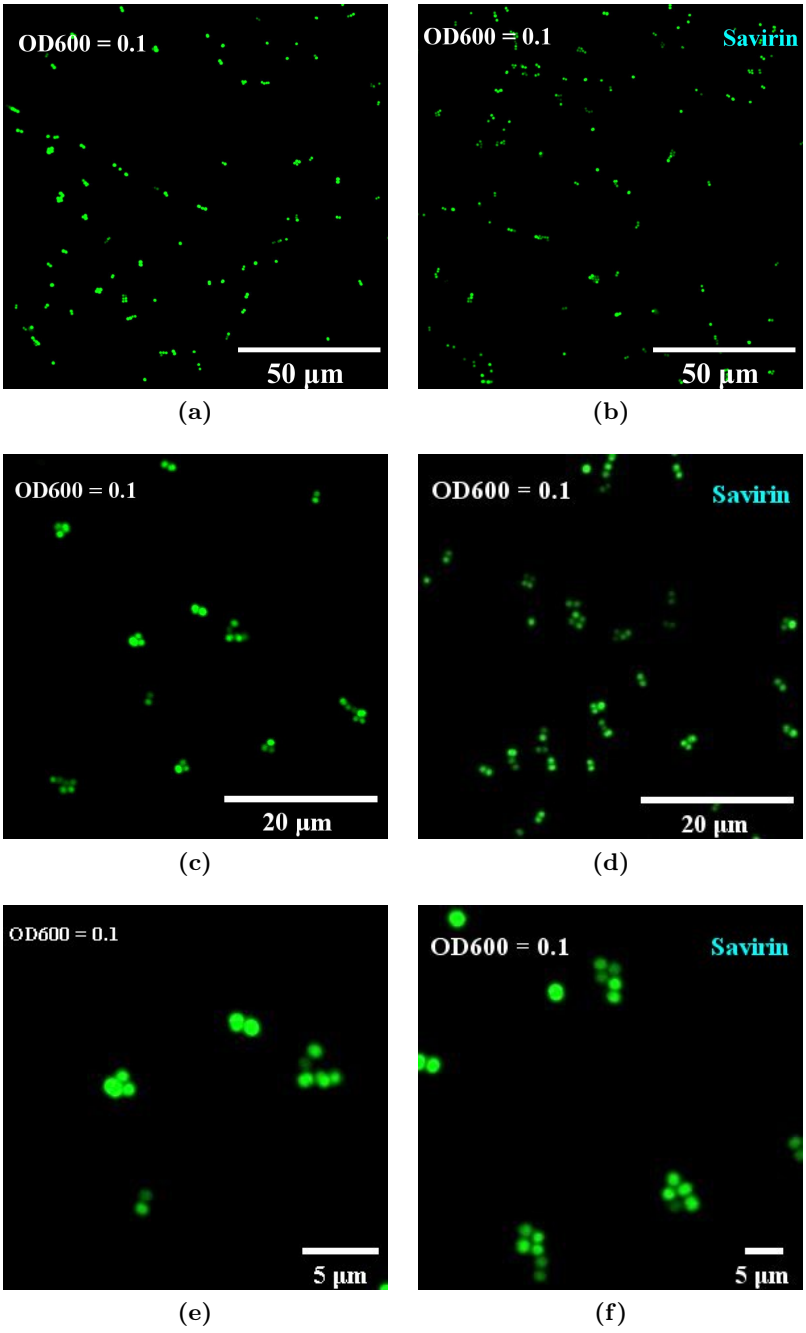

Figure 3.43: Fluorescence microscopy images of GFP *S. aureus* at OD600 = 0.1 after 30 minutes of incubation on gold in TSB. Right hand side images ((b), (d), (f)) show results for bacterial attachment in the presence of savirin (5 μg / mL). For comparison, left hand side images ((a), (c), (e)) show images of bacteria attaching in the absence of savirin. Sizes of images are as follows: 135 μm $\times$ 135 μm for (a)-(b), 50 μm $\times$ 50 μm (c)-(d) and 25 μm $\times$ 25 μm for (e)-(f).

ment. First, inhibition of *agr* by savirin prevents the upregulation of secreted proteases (such as aureolysin) that are normally induced at high cell density and facilitate biofilm restructuring by degrading cell-surface adhesins and matrix proteins [156, 241]. Blocking these proteases allows *S. aureus* to retain its adhesins for a longer period, thereby prolonging the reversible adhesion phase. Additionally, the absence of *agr* signalling results in a marked reduction in phenol, soluble modulins, which normally act as surfactants to promote micro, channel formation but also cause cell detachment [156, 241]. Without these surfactants, savirin-treated biofilms tend to form as flatter, denser layers with delayed maturation. Studies on *agr* mutants of staphylococci have also shown increased autolysin activity and enhanced extracellular DNA release, which further reinforce initial attachment [238]. Consequently, savirin-treated *S. aureus* displays a prolonged reversible adhesion phase with higher early cell adhesion, as corroborated by fluorescence microscopy and crystal violet assays, yet ultimately forms a less mature, more fragile biofilm.

Compensatory responses through global regulators such as Rot, SigB and SarA also play a role. When *agr* is inhibited, Rot remains elevated and continues to repress protease expression while promoting adhesin production [156]. Similarly, SigB and SarA may upregulate alternative adhesion pathways to partially compensate for the loss of *agr* signalling [156, 241]. QCM-D data support these observations as savirin-treated samples exhibit a delayed positive Δf peak and an extended period of low dissipation compared with untreated samples, reflecting the postponed transition from reversible to irreversible adhesion.

Overall, the data illustrate that targeting quorum sensing with savirin profoundly affects *S. aureus* biofilm formation. By locking the bacteria in a QS-inhibited state, biofilm maturation is stunted, the microorganisms cannot seamlessly transition from initial attachment to a robust, EPS-rich community structure. Instead, savirin-treated biofilms remain in a delayed state: cells initially attach, but then go onto form a biofilm with abnormal mechanical properties. Importantly, these alterations could make biofilms more vulnerable. A loosely connected, viscoelastic biofilm is likely easier to remove or penetrate with antibiotics, and any cells that do detach, due to the unstable matrix, might be more susceptible to host immune clearance[236]. This aligns with the concept of antivirulence strategies. By disarming the bacteria's coordination, they are made less resilient and easier to eradicate[237].

From a therapeutic perspective, using savirin or similar AgrA inhibitors could be a promising adjunct to conventional treatments. They would hinder biofilm establishment on medical implants or tissues by preventing *S. aureus* from mounting its organised, protected community. The timing of QS inhibition is likely crucial. The findings suggest that applying savirin early, during initial attachment, has significant effects on biofilm outcome. In practice, this could mean prophylactic or early post-infection administration of QS inhibitors might curb biofilm development before it becomes entrenched[237]. On the other hand, established biofilms might

be less affected by QS blockers alone, since the bacteria in mature biofilms often already have an inactive *agr* as part of their natural cycle[236]. Nonetheless, even in those cases, savirin could prevent re-activation of dispersal, potentially locking bacteria in a state that makes them more susceptible when the biofilm is intentionally disrupted by mechanical or chemical means.

In summary, savirin's inhibition of *agr* directly alters the timeline and molecular composition of *S. aureus* biofilm development. By delaying the usual 5–7 hour *agr* activation, savirin postpones the transition from reversible to irreversible adhesion, as evidenced by the delayed positive Δf peak and extended low-dissipation phase in the QCM-D profiles. Although alternative regulators eventually induce EPS production and other matrix components, this compensatory response is slower, resulting in a prolonged early adhesion phase, with greater initial cell attachment. As a result, the biofilm formed under savirin's influence remains thinner and less structurally developed than an untreated biofilm, likely due to its reduced matrix accumulation and modified viscoelastic properties. QS inhibition leaves the biofilm "fingerprint" distinctly different from that of a normal biofilm, with evidence of impaired matrix build-up and increased initial adhesion, in line with a biofilm of potentially lower stability that lacks the extensive, gel-like EPS network of the control biofilm. These findings underscore savirin's potential as an anti-virulence and anti-biofilm agent.

3.6 Conclusions

The QCM-D technique proved to be a powerful tool for probing bacterial surface adhesion and biofilm formation, offering real-time insight into viscoelastic properties and attachment dynamics of *S. aureus* and *P. aeruginosa*. Notably, distinct QCM-D signal patterns were detectable even in nutrient-rich media, underscoring the sensitivity and robustness of this method for biofilm studies. The reproducibility of the measurements across multiple runs further confirmed that QCM-D can reliably capture the adhesion behaviour of bacteria over extended periods.

Environmental factors, especially nutrient availability and temperature, had a pronounced impact on bacterial adhesion and biofilm development. In nutrient-rich TSB, both *S. aureus* and *P. aeruginosa* exhibited substantial biofilm formation, evidenced by large negative frequency shifts and increased energy dissipation in QCM-D data (indicative of viscoelastic film deposition) as well as higher biomass accumulation and surface coverage in complementary assays. In contrast, under nutrient-limited conditions (e.g. R2A medium or PBS buffer), the QCM-D showed markedly smaller shifts, correlating with minimal biofilm build-up. These findings align with literature showing that rich media foster robust biofilms while starvation conditions limit extracellular matrix production[216]. Temperature similarly influenced colonisation: at 37 °C (human body temperature) both species adhered and formed biofilm faster, whereas at 25 °C biofilms developed more slowly but ultimately became denser and potentially more stable.

Such temperature-dependent differences highlight the importance of environmental adaptation in biofilm physiology[221], with implications for understanding infections in cooler external environments versus warm host conditions.

Clear differences emerged between the biofilm formation strategies of *S. aureus* and *P. aeruginosa*. *S. aureus* tended to form thicker, more viscoelastic biofilms, as reflected by larger dissipation (energy loss) signals and characteristic frequency "peaks" in QCM-D indicating a transition from reversible to irreversible attachment. This reversible-to-irreversible transition, essentially the point at which initial weakly attached cells firmly anchor and begin producing matrix, is a dynamic feature of *S. aureus* biofilms. Its observation in QCM-D data underscores how *S. aureus* biofilm development proceeds in stages, consistent with reports that *S. aureus* first establishes a foundational cell layer before robust matrix accumulation. *P. aeruginosa*, on the other hand, formed biofilms that were mechanically stiffer (lower dissipation) and showed a more gradual attachment profile without the pronounced QCM-D frequency inflection seen for *S. aureus*. These differences can be attributed to biological factors: *P. aeruginosa* employs motility appendages (flagella and type IV pili) during early surface colonisation, which influence its adhesion dynamics. Indeed, flagellar-mediated attachment is known to be important in *P. aeruginosa* initial biofilm establishment[216]. *S. aureus*, lacking such flagellar motility, often relies on surface adhesins and rapid cell-cell aggregation, leading to clumpier microcolonies. This propensity for *S. aureus* to cluster was confirmed by microscopy in this study and is consistent across different *S. aureus* strains, as discussed below. Overall, the two species exhibit distinct colonisation strategies, *S. aureus* rapidly accumulates into multilayered, soft biofilms, whereas *P. aeruginosa* produces thinner but more rigid biofilms. This reflects their fundamental Gram-positive vs. Gram-negative structural and behavioural differences[202]. These findings are in line with prior observations that biofilm architecture and mechanics vary significantly between species, influenced by factors like exopolymer composition and motility mechanisms[216].

Experiments using a GFP-labelled *S. aureus* strain (SH1000-GFP) provided additional insights and validation. Fluorescence microscopy of SH1000-GFP biofilms allowed direct visualization of cell distribution on surfaces, revealing that *S. aureus* cells preferentially attach in groups, microcolonies, even at early time points, rather than as isolated single cells. This corroborates the QCM-D indications of rapid mass accumulation and also reflects *S. aureus*' natural tendency to form clumps via intercellular adhesion. Importantly, when comparing the GFP-tagged SH1000 to the standard *S. aureus* ATCC 6538™ strain, consistent biofilm formation behaviour and QCM-D profiles were observed between them. This suggests that the adhesion and biofilm phenomena observed are robust across different *S. aureus* genetic backgrounds, and that the GFP tag (and associated genetic differences of SH1000) did not alter the fundamental adhesion dynamics. The use of SH1000-GFP thus not only enabled correlated optical/QCM-D analysis but also confirmed that the findings for *S. aureus* are broadly applicable, adding confidence to their biological relevance.

QS inhibition experiments with savirin highlighted the role of QS in *S. aureus* biofilm development. *S. aureus* samples grown with savirin showed noticeably altered QCM-D responses compared to controls. In the presence of savirin, the characteristic frequency peak signalling the transition to irreversible adhesion was delayed or diminished, and the overall biofilm-induced frequency shift was reduced, indicating a thinner, less-developed biofilm matrix. Interestingly, these differences were not evident in the very early stages of attachment, initial adhesion (within the first few hours) was similar with or without savirin, as also confirmed by fluorescence microscopy which showed comparable early cell coverage. Only after the point when *S. aureus* would normally activate the Agr QS system (around 5–7 hours into biofilm growth) did the savirin-treated samples diverge. This timing coincides with the known activation window of the *agr* regulon in *S. aureu*s, which controls production of many virulence and dispersal factors[234]. The results therefore strongly suggest that savirin's inhibition of *agr* delayed the typical biofilm maturation sequence. By preventing the QS-mediated shift to aggressive biofilm growth and eventual dispersal, savirin kept *S. aureus* in a prolonged state of initial attachment, resulting in a sparser, less viscous biofilm. This interpretation is supported by prior studies showing that chemically blocking *agr* can render *S. aureus* less virulent and trap it in a biofilm state that is more susceptible to host clearance or treatment[234, 237]. In the experiments, the "signature" of a savirin-influenced biofilm was a distinct QCM-D profile: an extended low-dissipation (rigid) phase with sustained frequency decrease (cells attached but not producing much soft matrix), followed by only a modest rise in dissipation later. These observations align with the idea that QS inhibition curtailed the normal production of expansive EPS matrix and delayed the point of irreversible adhesion. Consequently, the savirin-treated biofilms remained thinner and mechanically different from typical *S. aureus* biofilms, potentially of lower stability due to the reduced EPS "glue." Such differences underscore that targeting quorum-sensing can indeed modulate biofilm development. In summary, the savirin results pinpoint the timescale at which *agr*-mediated processes become critical in *S. aureus* biofilm formation, a valuable insight for timing interventions. They also highlight savirin's potential as an anti-biofilm agent that interferes with the regulatory pathways of biofilm maturation rather than killing bacteria outright, an approach which could mitigate resistance development[234].

Overall, Chapter 3 demonstrated how biological and environmental factors influence bacterial adhesion and biofilm formation, using QCM-D supported by microscopy and assays. *S. aureus* and *P. aeruginosa* were shown to have markedly different adhesion behaviours, yet both responded to changes in nutrients, temperature, and quorum signals in logical ways consistent with their biology. These conclusions are aligned with existing literature on biofilm development and physiology. Comparing the QCM-D findings with prior studies, for example, noting that *P. aeruginosa* motility aids surface colonisation or that *S. aureus agr* system timing dictates biofilm progression, ensures that the interpretations are grounded in known mechanisms. In short, *S. aureus* tends to form thick, soft biofilms controlled by its quorum-sensing timeline,

whereas *P. aeruginosa* forms thinner, stiff biofilms influenced by motility and nutrient conditions. Both species' adhesion processes can be modulated by external factors, and these findings collectively advance our biophysical understanding of how initial surface attachment transitions into mature biofilm architecture. The insights gained here set the stage for deeper biophysical analysis (Chapter 4) and broader implications discussed in the overall conclusions (Chapter 5).

Chapter 4

Silica colloid particle deposition on gold

4.1 Introduction

The process of bacterial attachment to surfaces is a multifaceted phenomenon influenced by a complex interplay of biological and physical interactions which are not yet fully understood. Researchers often refer to bacteria as "biocolloids" or "living colloids" and frequently approximate bacterial behaviour to that of colloidal particles in both theoretical and experimental contexts to elucidate their properties.[242–245] Such approximations can provide valuable insights into bacterial adhesion mechanisms and aid in the analysis of early adhesion data. van Loosdrecht et al.[246] highlight the physicochemical principles that liken bacteria to colloids in various environments. Hermansson [172] applies the DLVO theory to microbial adhesion, showing similarities with colloidal interactions. Bos *et al.*[247] provide an analysis of microbial adhesion mechanisms, comparing them to colloidal particles. Flemming and Wingender[193] discuss colloid-like behaviour of bacteria within biofilms, emphasising the role of EPS. In Chapter 3, the experiments aimed at characterising the process of biofilm formation. This chapter extends that discussion by exploring whether bacterial behaviour can be approximated to colloids, thereby enhancing our understanding of bacterial adhesion and aiding the analysis of early bacterial adhesion data.

Comparing bacterial surface attachment to a colloidal model may illuminate the onset and extent of biological processes during the initial stages of bacterial adhesion to substrates. The QCM-D has been extensively used in bacterial adhesion studies and, given its sensitivity to mass changes and energy dissipation, it provides a robust basis for comparing bacteria-surface interactions with colloid-surface interactions.

To carry out a comparison of the adsorption of bacteria with a colloidal system, a series of colloidal particle deposition experiments were conducted using silica colloids of spherical shape and a size (1 μm) comparable to that of SH1000-GFP *S. aureus* cells. The SH1000-GFP strain was selected for comparison as it allows facile fluorescent imaging, enabling surface distribution comparison. The colloid data included optical microscopy images for particle distribution insight, along with QCM-D frequency and dissipation data. The results were compared to bac-

terial adhesion data carried out in buffer only, to eliminate any effects of compounds present in growth media. The comparison between cells and colloids was made to determine whether bacterial cells behave like independent "biocolloid" spheres or whether biological interactions cause significant deviations from typical colloid absorption behaviour. In summary, this chapter aims to elucidate the similarities and differences between bacterial adhesion and colloidal particle behaviour using QCM-D as a primary analytical tool, in order to advance understanding of the early stages of bacterial surface attachment and the underlying mechanisms governing these interactions.

4.2 Experimental methods

The aim of the colloid studies is the comparison of the bahaviour of silica colloids to the SH1000-GFP fluorescence images and QCM-D data, seen in Section 3.4. The experimental methods for the colloid experiments therefore aimed at replicating the conditions of the bacterial studies. The colloid specific information is therefore outlined below, whereas more details applicable to all experiments described in this thesis are available in Chapter 2.

4.2.1 Colloid suspension preparation

The colloids used in the deposition studies are 1 μm silicon dioxide particles (Sigma Aldrich). The solvent used in all suspensions was 0.1 M NaCl. The colloid concentrations used were aligned with SH1000-GFP OD600 values from earlier fluorescence imaging, AFM, and QCM-D studies. This involved translating OD600 values into estimated bacterial concentrations based on a standard curve depicted in Fig. 4.1. The curve was constructed by obtaining colony forming units (CFU) for a range of OD600 SH1000-GFP *S. aureus* concentrations in TSB, maintaining conditions consistent with the QCM-D and imaging studies conducted during this project. The colloid concentrations were selected to equate to the bacterial concentrations at a 1:1 ratio. These concentrations are detailed in Table 4.1.

SH1000-GFP *S. aureus* OD600	0.1	0.5	1.0
Silica colloid wt.%	0.25	1.25	2.50

Table 4.1: GFP *S. aureus* OD600 values and corresponding silica particle (1 μm) weight percent. The values represent a 1:1 bacterial cell to particle ratio.

4.2.2 Optical microscopy imaging of colloid deposition

Colloidal suspensions for the three concentrations of interest were prepared. The substrate used was gold, to replicate QCM-D experimental conditions. 80 μL of a given suspension was placed

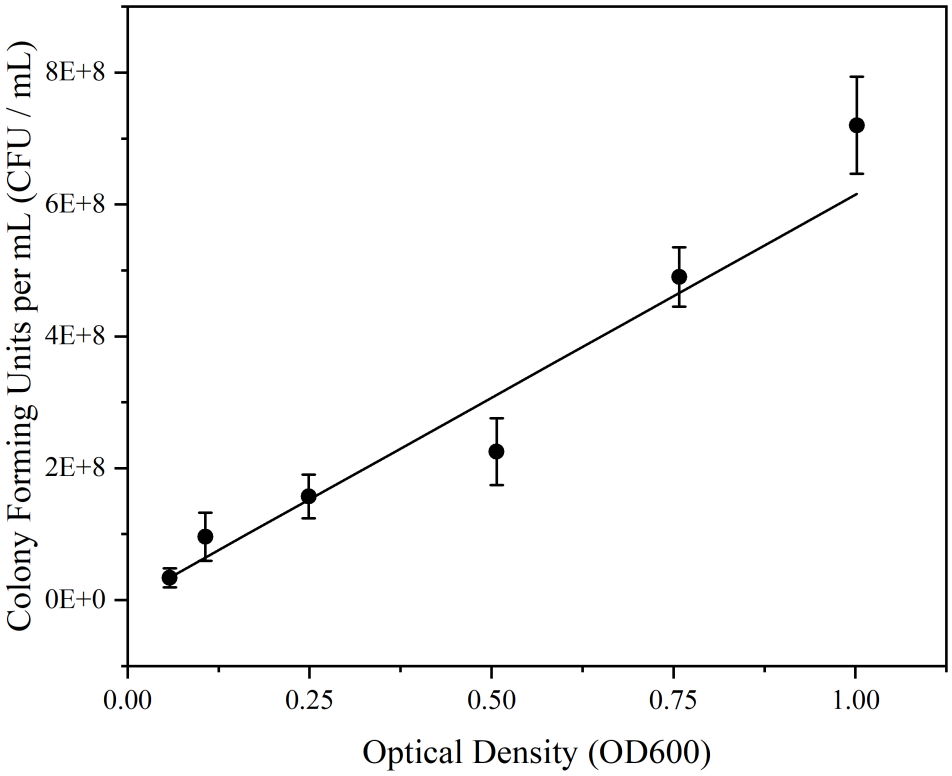

Figure 4.1: Bacterial calibration curve derived from the enumeration of colony forming units per mL across a range of OD600 values for SH1000-GFP *S. aureus* in TSB. Each data point represents the average of three independent measurements.

onto a cleaned (as described in Section 2.2.1), gold QCM crystal. The liquid was contained on the crystal using a small rubber ring, and a glass slide was placed on top to prevent evaporation. Images were taken immediately using Nikon ME600 optical microscope and a Pixelink PL-A742 machine vision camera. A 20 × magnification objective (Nikon) was used. Contrast was optimised using Fiji software.

4.2.3 QCM-D monitoring of colloid deposition

The QCM-D protocol followed the method outlined in Section 2.2.1. Two different types of QCM-D experiments were carried out. The initial experiment consisted of the sequential loading of the three colloid samples of varying concentrations (Table 4.1). The experiment began with flowing through pure solvent (0.1 % NaCl) for 20 minutes, a timescale which allows for the stabilisation of the frequency and dissipation signals. Next, the colloidal suspension of the lowest concentration (0.25 %) was added to the chamber, displacing the solvent. Data were collected for an hour, following by the flow of the intermediate concentration (1.25 %). The

data were again recorded for an hour, followed by the loading of the highest concentration (2.50 %). After an hour pure solvent was flowed through the system, and data were recorded for a final 30 minutes. Next, a series of three QCM-D experiments was conducted, where the deposition process was observed for 24 hours for each of the three colloidal concentrations separately. Similarly, a baseline measurement with the solvent was established over the initial 20 minutes.

4.3 Optical microscopy imaging of silica colloid deposition

Ionic strength played a crucial role in forming silica dispersions suitable for deposition using the QCM flow chamber. For 0.25 wt.% silica suspensions, optical microscopy revealed no deposition when colloids were suspended in either pure water or a high salt concentration (1 M NaCl) solvent. However, deposition on a gold surface was observed in 0.1 M NaCl colloidal suspensions. Consequently, the ionic strength of the solvent in all subsequent silica colloid deposition studies was maintained at 0.1 M NaCl (1 nm Debye-Hückel screening length). The concentration's impact on the deposition process can be understood through the size of the electrical double layer: as ionic strength increases, the Debye length shortens, resulting in a thinner double layer. This allows particles to approach the surface closely enough for attractive van der Waals forces to dominate, leading to deposition.[29]

To investigate silica colloid deposition and understand the effects of distribution and concentration, three experiments were conducted where silica suspensions of different concentrations were left to deposit onto gold surfaces for 30 minutes. Optical microscope images taken at $t =$ 30 min. Initially, a series of images up to 3 h were obtained for all three concentrations. Since no further deposition was observed after $\approx$ 20 min, images taken at t = 30 min were chosen to represent the final colloid distribution on gold. This also enables comparison with fluorescent microscopy images presented in Chapter 3, which were also captured at $t = 30$ min.

Fig. 4.2 presents the results of colloid deposition experiments for various particle concentrations. Predictably, the higher the colloid concentration, the greater the surface coverage. The lower two concentrations display a seemingly random distribution of particles on the surface. At the higher 2.50 wt.% concentration, full surface coverage is achieved, with areas where the colloids start to stack on top of each other. In contrast, no 3D structures are observed in the two lower concentration results.

Fig. 4.3 was created to demonstrate the disparity in particle distribution between colloids and bacterial cells. The image shows that no individual SH100-GFP cells are present on the surface, even with the low coverage observed. In contrast, only about 23.5% of colloids were in contact with other colloidal particles. This straightforward comparison suggests that bacterial communication, or quorum sensing, occurs, leading to group attachments during the very early

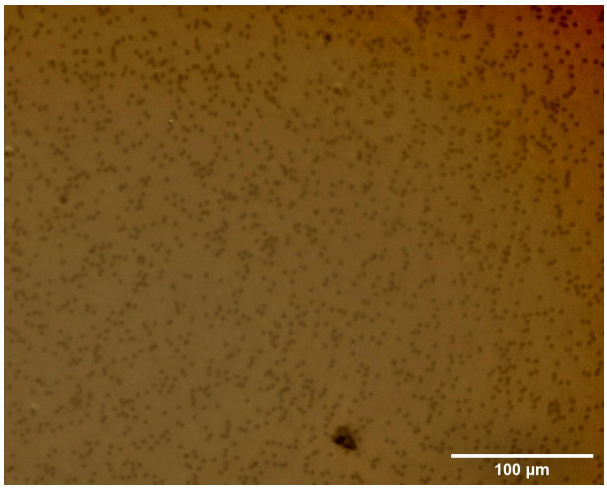

(a) 0.25 wt.%

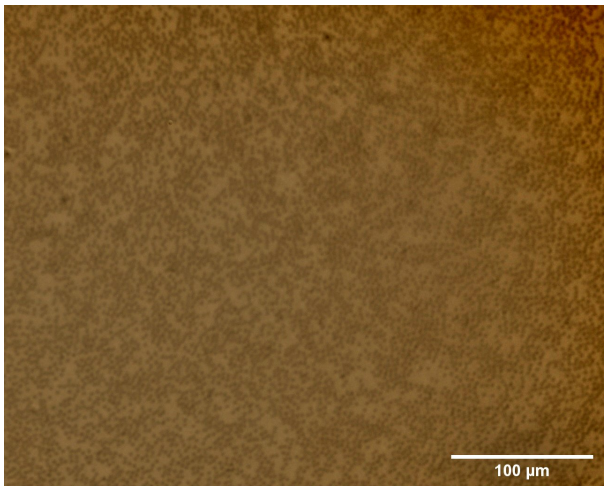

(b) 1.25 wt.%

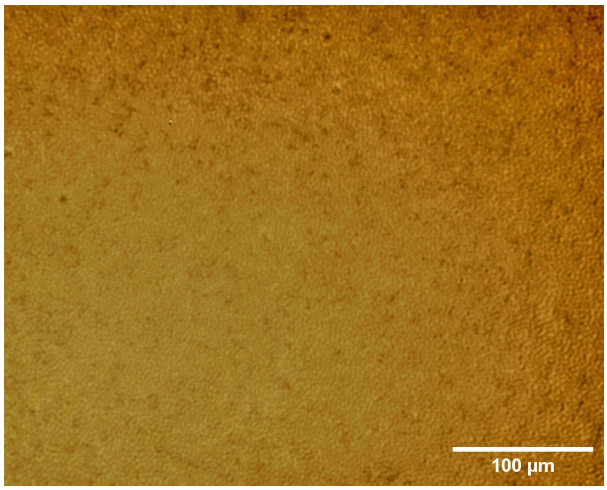

(c) 2.50 wt.%

Figure 4.2: Optical microscopy images of 1 µm silica particle deposition on a gold substrate. The colloidal silica concentrations used are 0.25 (*a*), 1.25 (*b*) and 2.5 (*c*) wt.%. 0.1 M NaCl was used as solvent in all suspensions. Images are taken 30 minutes after the silica suspension is added to the substrate.

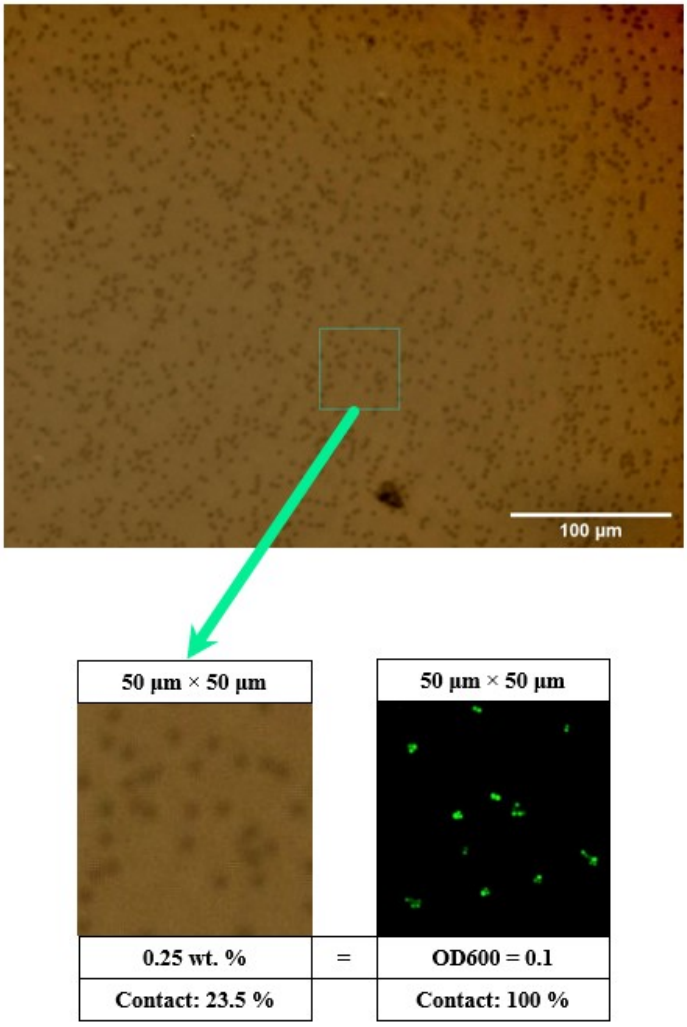

Figure 4.3: Comparison of optical microscopy image of colloid deposition on Au at 0.25 wt.% and the bacterial deposition on Au at the equivalent concentration of OD600 of 0.5. Both images were captured at 30 minutes following start of incubation/deposition. The percentage of particles in contact with neighbouring particles is indicated, with 100% of cells in contact, and only 23.5 % of colloids in contact.

stages of biofilm formation, specifically the attachment of planktonic cells to substrates.

Established literature on *S. aureus* growth kinetics indicates that only limited cell division occurs within a 30-minute period, given that the doubling time in TSB at 37 °C is typically 40–60 minutes [235]. To minimise bacterial growth during the adhesion assay, the incubation was limited to 30 minutes, roughly one generation time for *S. aureus* in rich media. Thus, at most a single cell division could occur. The fluorescent images (Fig. 3.40) show clusters of >4–8 cells even at this early time, which cannot be explained by one division of a single bacterium. Instead, it indicates that bacteria tend to arrive or aggregate in groups (perhaps due to slight clustering in the inoculum or rapid surface proliferation). In contrast, the inert silica colloids

remained monodispersed (individual particles) in their images, confirming that the observed bacterial clumps are a result of biological aggregation, not measurement artifact. Moreover, fluorescence imaging consistently shows nearly 100% of cells in close contact, compared to only 23.5% contact observed for inert beads. This marked difference suggests that the extensive cell–cell interactions are not solely due to cell division, but are predominantly the result of active aggregation processes, such as those mediated by quorum sensing. While time-lapse imaging or quantitative cell counts were not performed in the present study, these techniques could be utilised in future work to further elucidate cell division dynamics during the pre-imaging period.

4.4 QCM-D monitoring of silica colloid deposition

4.4.1 Stepwise deposition experiment

A preliminary 4-hour experiment was initially carried out, which is of a significantly shorter duration than the 24-hour bacterial experiments discussed in Chapter 3. This initial QCM-D colloid experiment examined three colloidal suspensions introduced into the QCM-D chamber sequentially. The normalised changes in frequency (Δf) and dissipation (ΔD) of a Au-coated QCM-D electrode in response to colloid deposition were plotted for harmonics $n = 1, 3, 5$, and 7.

The findings, illustrated in Fig. 4.4, show minor peaks in the first overtone of both frequency and dissipation just before each new sample is introduced into the chamber. These peaks are experimental artefacts caused by the initial introduction of the new sample solution into the loop, which leads to slight temperature fluctuations in the system. The experiment started with a solvent-only baseline until $t = 20$ min, at which point the first and lowest silica concentration colloids (0.25 wt.%) were injected. The sensor shows a significant negative Δf for the first overtone and a gradual gradual increase for $n = 3$, 5, and 7.

One hour after the initial dispersion was introduced, a second colloidal sample with a concentration of 1.25 wt.% was added to the QCM-D chamber at $t = 1$ h 20 min. The system exhibited a further negative Δf for the first overtone and a further positive shift for the other overtones. This pattern of a stepwise decrease for the first overtone and increases for $n = 3$, 5, and 7 was observed again when the final sample with the highest concentration (2.50 wt.%) was introduced at $t = 2$ h 20 min. The final Δf values for $n = 1$, 3, 5, and 7 were -320, 20, 15, and 30 Hz, respectively.

In general, the variations in ΔD exhibit a consistent pattern across all four overtones. There is a gradual increase in ΔD as each colloidal suspension sample is introduced sequentially. This process involves an initial sharp rise, followed by stabilisation at each stage. As the overtone number increases, the overall magnitude of ΔD decreases throughout the experiment. The final values are 475, 285, 105, and 30×10^{-6} Hz for $n = 1$, 3, 5, and 7, respectively.

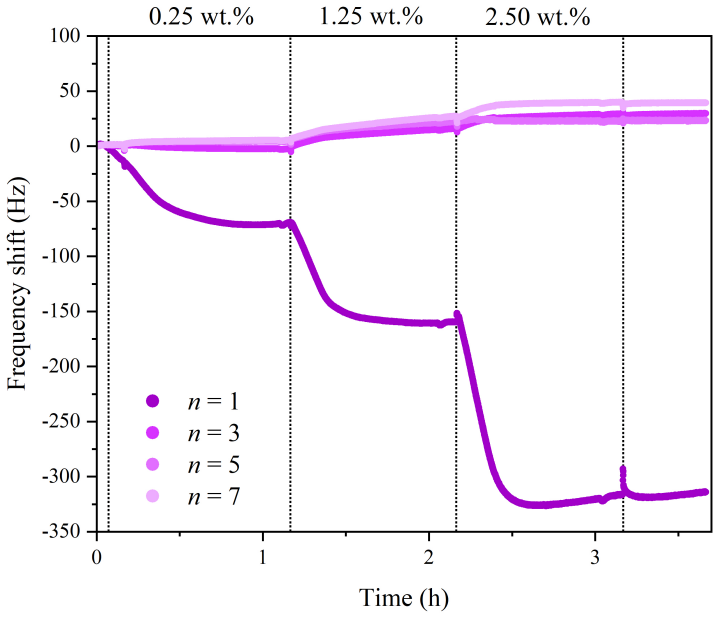

(a) Frequency

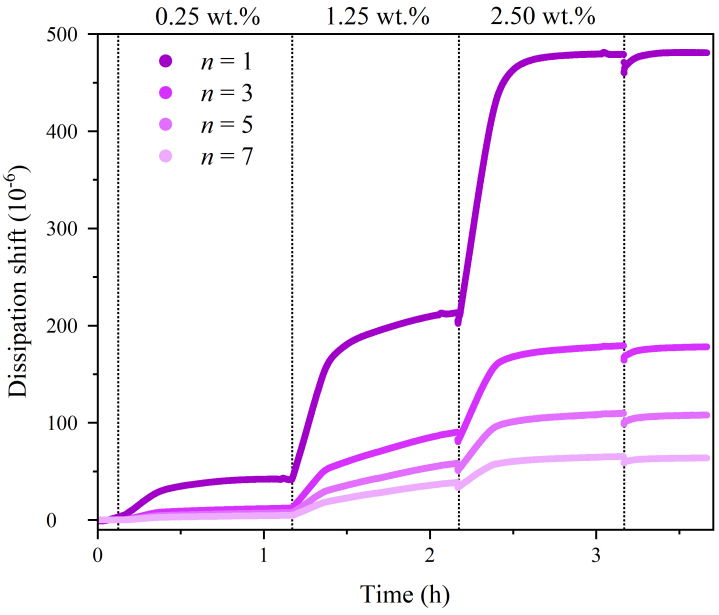

(b) Dissipation

Figure 4.4: Normalised frequency (a) and dissipation (b) QCM-D data for the sequential deposition of silica colloid suspensions at 3 different concentrations to a gold surface. The experiment began with a solvent only (0.1 M NaCl) baseline. The lowest concentration (0.25 wt.%) colloid suspension is added at $t = 20$ min. The subsequent suspension (1.25 wt.%) is flowed through at $t = 1$ h 20 min. Finally, the highest concentration suspension (2.50 wt.%) is flowed through at $t = 2$ h 20 min. The experiment is concluded with a solvent wash at $t = 3$ h 20 min, with data collected for a final 30 min.

The observed positive Δf in $n = 3$, 5, and 7 was unexpected, as the Sauerbrey equation (Eq. 1.1) predicts that increased mass loading should lead to a negative frequency shift. At 5 MHz (fundamental), the shear wave penetrates the entire deposited layer, averaging the response, whereas at higher overtones (15 MHz, 25 MHz, etc.), the effective penetration depth is shallower, making those signals respond to the near-surface viscoelasticity. Thus, the fundamental frequency provides an integrated, whole-film measurement, while overtones can display phenomena like the positive shifts from coupled resonance in regions of the film that are not rigidly coupled.[148] Notably, the fundamental frequency ($n = 1$) exhibits the expected behaviour, reflecting the overall mass loading over time and providing an integrated measure of the entire film's viscoelastic properties. In contrast, higher overtones ($n = 3$, 5, 7), which possess shorter acoustic wavelengths, are more sensitive to local viscoelastic responses and structural heterogeneities within the deposited layer. This indicates that while the fundamental frequency captures changes over a larger spatial and temporal scale (i.e. the complete mass and rigidity of the film), the overtones respond more acutely to localised variations near the sensor surface.

Optical microscopy images captured 30 minutes after the onset of colloid deposition (Fig. 4.2) confirm that colloids are deposited on the surface early in the experiment and that higher concentrations result in greater surface coverage. Under these conditions, an increased mass deposition would normally result in more negative Δf values. However, the detection of positive Δf values in the higher overtones suggests that factors beyond simple mass loading, such as local viscoelastic effects or decoupling of parts of the film from the sensor oscillation, are influencing the response. Individual deposition experiments were conducted to verify that this phenomenon is reproducible.

4.4.2 Individual deposition experiments

A series of QCM-D experiments were conducted to confirm the positive Δf shift for all harmonics above the fundamental frequency. This experiment spanned a significantly longer duration of 24 hours. Particle suspensions were introduced again at $t = 20$ minutes after which data collection continued for 24 hours. The outcomes of these experiments are presented in Fig. 4.5.

The frequency outcomes for $n = 3$, 5, and 7 in the experiment with the lowest concentration, as shown in Fig. 4.5a, indicate a gradual decline in Δf over the course of the experiment, ending at -16, -7, and 1 Hz, respectively. This pattern aligns with mass deposition as predicted by conventional mass loading theory. In contrast, $n = 1$ exhibits markedly different behaviour, beginning with a sharp drop to around -50 Hz, followed by a stepwise increase from negative to a positive Δf value of approximately 18 Hz by the experiment's conclusion. These notable variations observed in $n = 1$ are unexpected, given that deposition was observed to cease after $\approx$ 30 min, as discussed in Section 4.3, indicating that these fluctuations are not due to mass

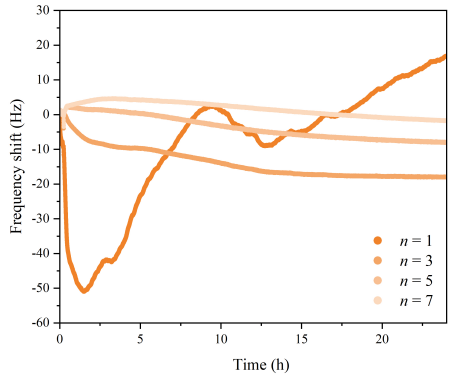

(a) Frequency: 0.25 wt.%

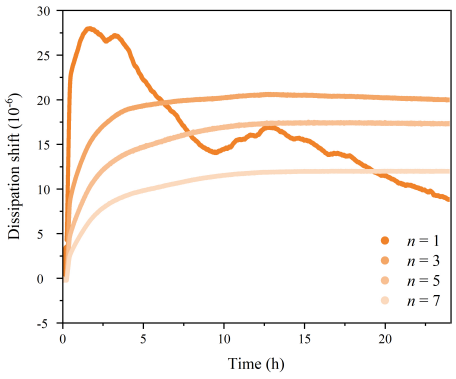

(b) Dissipation: 0.25 wt.%

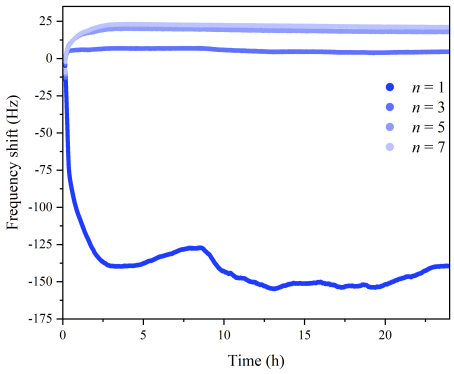

(c) Frequency: 1.25 wt.%

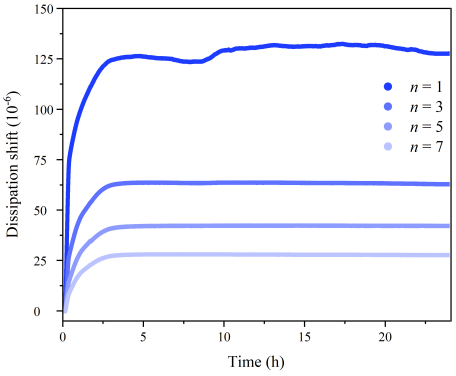

(d) Dissipation: 1.25 wt.%

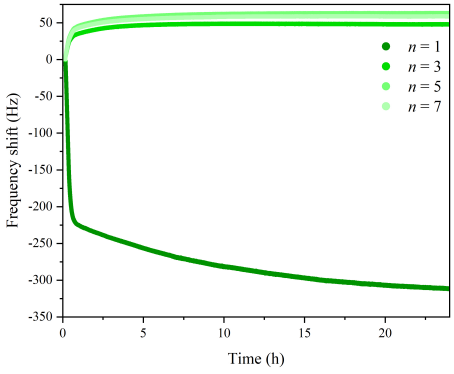

(e) Frequency: 2.50 wt.%

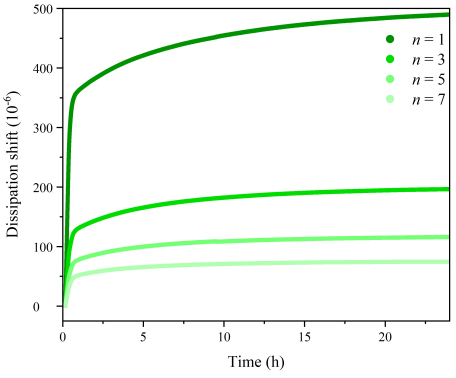

(f) Dissipation: 2.50 wt.%

Figure 4.5: Normalised frequency and dissipation QCM-D data for the deposition of colloidal silica particles on gold. A series of three experiments were carried out at a range of particle concentrations: 0.25, 1.25 and 2.50 wt.%. All experiments began with a solvent baseline, followed by the introduction of the particles at $t = 20$ min.

changes.

The results at higher concentrations depicted in Figs 4.5c and 4.5e exhibit similar overall behaviour across all four overtones, contrasting with the 0.25 wt.% results. In both experiments, $n = 1$ shows a sharp decline in Δf (up to -136 and -223 Hz, respectively), followed by a more gradual decrease (up to -152 and -309 Hz, respectively). Interestingly, both experiments indicate that $n = 3$, 5, and 7 experience an increase in Δf, which then stabilises for the remainder of the experiment, as seen in the previous sequential experiment. The final Δf values for 1.25 wt.% are 1, 18, and 22 Hz in ascending order of overtone. For 2.50 wt.%, the final values are 46, 59, and 54 Hz.

This positive Δf is atypical in conventional QCM-D data analysis, as it would usually suggest a mass loss. The primary distinction between 1.25 wt.% and 2.50 wt.% lies in the magnitude of Δf, with higher values observed in the experiment with the highest concentration. Another notable difference is in the behaviour of the first overtone, which exhibits a rapid initial decrease in both experiments but shows some fluctuations for 1.25 wt.% thereafter, while 2.50 wt.% demonstrates a smooth, gradual decrease throughout. Examining the Δf results for all three concentrations reveals that higher colloid concentrations correspond to higher Δf values (final $n = 5$ Δf in order of increasing wt.%: -7, 18, and 46 Hz). Additionally, it can be observed that lower colloid concentrations result in more pronounced fluctuations for $n = 1$.

Despite this, all three outcomes exhibit a similar overall pattern regarding overtone ordering, which remains consistent across the experiments. Specifically, $n = 1$ reaches negative values, followed by $n = 3$ through 7, which show progressively higher Δf values. Although conventionally omitted from QCM-D data analysis due to its higher sensitivity to environmental noise and artefacts, the behaviour of the first overtone is noteworthy. It consistently shows a large, negative Δf in all three experiments, unlike the other three overtones.

The ΔD in all three experiments exhibit a similar trend: a rapid initial increase followed by a plateau. Higher concentrations lead to quicker stabilisation. An exception is observed for $n = 1$ in the 0.25 wt.% experiment, where the dissipation initially rises to 28×10^{-6} at 1.6 h, then decreases stepwise instead of stabilising. This behaviour is reflected in the corresponding frequency plot, which is also unique to the 0.25 wt.% experiment. Despite the shape similarity, all three plots display the same overtone ordering, with lower overtones reaching higher ΔD values. There appears to be a concentration effect on ΔD; higher colloid concentrations result in higher ΔD values (final ΔD in increasing wt.%: 18, 40, and 100 for n = 5).

The elevated ΔD values observed, along with the significant variation in values across different overtones, suggest that the data are not suitable for straightforward Sauerbrey analysis. Numerous similarities can be identified between the previously discussed stepwise deposition ex-

periments (Fig. 4.4) and this much longer timescale experiment, where the three concentrations are examined individually. Once again, the Δf values are positive and increase in magnitude with higher colloid concentration, except for $n = 1$, which exhibits large, negative Δf values. Similarly, the ΔD behaviour is mirrored, both in terms of overtone ordering and magnitude increase with colloid concentration.

When comparing the individual and stepwise results, a significant difference is observed at the lowest concentration of 0.25 wt.%. Specifically, the behaviour for $n = 1$ in Fig. 4.4a with only the 0.25 wt.% sample present in the QCM-D chamber (from $t = 20$ min to $t = 1$ h 20 min) shows an initial decrease followed by a stabilisation in Δf, which contrasts with the fluctuating result for the same overtone seen in Fig. 4.5a. The stabilisation observed in the stepwise experiment aligns with the optical imaging observations (Section 4.3), indicating that colloid deposition completes after roughly 20 min. This contrasts with the fluctuations observed over the 24-hour duration of the individual experiment, suggesting that these fluctuations were due to instability introduced over the extended timescale of the experiment.

In summary, the findings validate that the positive Δf observed at $n = 3$, 5, and 7, and the negative Δf observed at $n = 1$, are consistent and genuine effects that cannot be accounted for by traditional mass loading theory. Furthermore, significant dissipation excludes the data from the Sauerbrey analysis domain, which necessitates the deposited mass to be both thin and rigid.

4.4.3 Overtone analysis

This deviation from expected behaviour points to a phenomenon that involves not just mass deposition but also the mechanical properties of the particle-surface interface, potentially explained by the coupled-resonator model.

A review of existing QCM-D experiments highlighted earlier research examining micrometre-sized particles adhering to QCM crystal surfaces. Positive frequency shifts observed in these systems can be interpreted as a force balance related to the stiffness of the sphere/crystal contact. According to traditional Sauerbrey models, such positive frequency shifts would be impossible under the conventional QCM-D interpretation as a mass balance. Dybwad was the first to report coupled-resonator effects for QCM measurements of individual gold particles in air, noting an increase in the resonant frequency of the resonator.[248] Dybwad concluded that a secondary resonator (gold particle) provides "inertial loading" to the quartz resonator if its resonance frequency is higher than that of the crystal, resulting in a decrease in the resonance frequency for the coupled-resonator. Conversely, a weakly bonded particle provides "elastic loading" to the quartz resonator if the resonance frequency of the particles is lower, leading to an overall increase in the resonant frequency of the coupled-resonator.

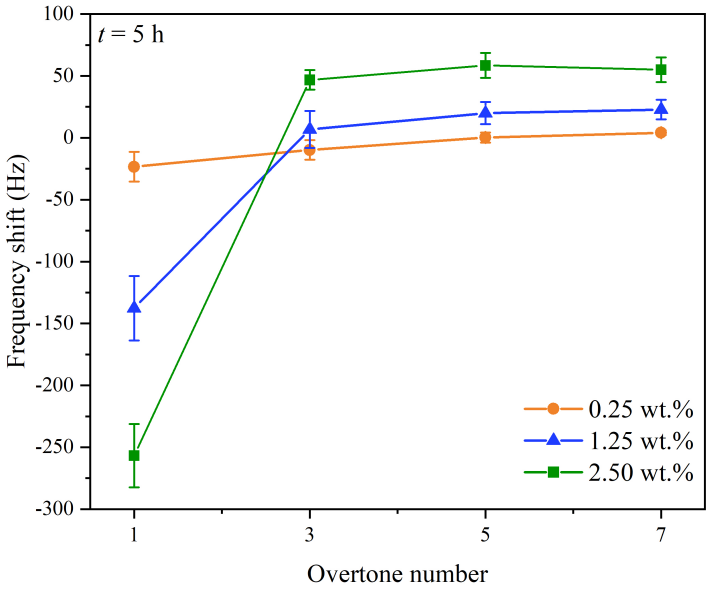

(a) Frequency

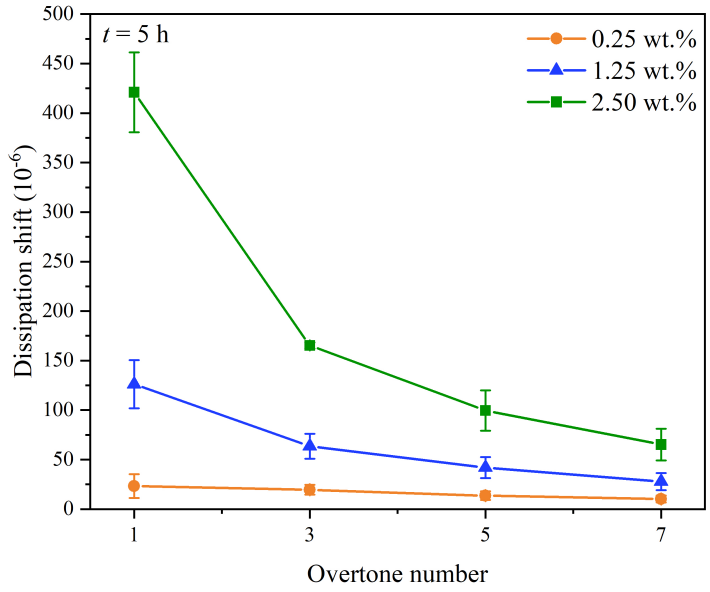

(b) Dissipation

Figure 4.6: Time-averaged Δf (a) and ΔD (b) values plotted against the overtone order. The values are taken from the individual deposition experiments at $t = 5$ h. The data points are the means of at least three measurements, and the errors are standard deviations.

The coupled resonance theory, as described by Pomorska *et al*,[190] is instrumental in understanding the interaction between colloidal particles or bacteria and a QCM-D sensor. This theory is essential for analysing adhesion properties and the viscoelastic behaviour of the bonds formed between particles and the sensor surface. The coupled resonance model is derived from the principles outlined in the study of coupled oscillators, where the adhered particles form a resonating system with the QCM sensor. This model, initially proposed by Dybwad[248] and further developed by D'Amour *et al*[249], describes how particles bound to the surface form a composite resonator with the crystal. The model accounts for the interactions between the resonance frequencies of the sensor and the particles, leading to distinct behaviour depending on the size and attachment strength of the particles.

The following equations, adapted from Pomorska *et al*[190], are central to understanding the coupled resonance model:

Coupled Resonance:

This equation is derived from the coupled resonance model, which was initially proposed by Dybwad[248] and further developed by D'Amour *et al*[249]. It explains the coupled resonance phenomenon between the QCM-D sensor and the attached particles. The term inside the parentheses accounts for the interaction between the resonance frequencies of the sensor and the particles, including the damping effects.

The left-hand side of the equation represents the normalised complex frequency shift, which combines both the real part (frequency shift) and the imaginary part (bandwidth shift) relative to the fundamental frequency. The right-hand side of the equation describes the contribution of the adsorbed spheres to the frequency shift and bandwidth shift of the QCM. It takes into account the number and mass of the spheres, their resonant frequency, and the dissipative interactions.

$$\frac{\Delta f + i\Delta\Gamma}{f_0} = \frac{N_S m_S \omega}{\pi Z_q}\left(\frac{\omega_S^2 + i\omega\gamma}{\omega^2 - \omega_S^2 - i\omega\gamma}\right) = -\frac{N_S m_S \omega}{\pi Z_q}\cdot\frac{1}{1-\frac{\omega^2}{\omega_S^2}+i\frac{\omega\gamma}{\omega_S^2}} \approx -\frac{N_S m_S \omega}{\pi Z_q}\cdot\frac{1}{1-\frac{\omega^2}{\omega_S^2}} \quad (4.1)$$

Where:

- Δf: The change in real part of the frequency shift of the QCM due to the adsorption of particles (Hz)
- $\Delta\Gamma$: The change in the resonance bandwidth (half-bandwidth at half-maximum), representing dissipative losses in the system (Hz) - dissipation and bandwidth are equivalent

ways of quantifying the dissipative process ($D = 2\Gamma/f$)

- f_0 The fundamental frequency of the quartz crystal (Hz)
- N_S: Number density of the spheres (m^{-2})
- m_S: Mass of a single sphere (g)
- ω: Resonance frequency of the crystal
- ω_S: Resonance frequency of the coupled-resonator
- γ: Damping coefficient (s^{-1})
- Z_q: Acoustic impedance of AT-cut quartz (8.8×10^6 kg m^{-2} s^{-1})
- $\frac{N_S m_S \omega}{\pi Z q}$: This term represents the scaling factor related to the number density of particles (N_S), their mass (m_S) the resonance frequency of the QCM sensor (ω) and the acoustic impedance of quartz (Z_q).
- $\frac{\omega^2 - \omega_S^2 - i\omega\gamma}{\omega_S^2 + i\omega\gamma}$: This term accounts for the interaction between the resonance frequencies of the sensor (ω) and particles (ω_S), including the damping effects (γ).

The approximation in Eq. 4.1 is valid when the dissipative component (γ) is small or can be neglected.

Inertial Loading - Sauerbrey Equation:

Eq. 4.1 simplifies to the Sauerbrey equation when $\omega_S \gg \omega$, which simplifies the fraction:

$$1 - \frac{\omega^2}{\omega_S^2} + i\frac{\omega\gamma}{\omega_S^2} \approx 1 \tag{4.2}$$

Thus, the equation simplifies to:

$$\frac{\Delta f + i\Delta\Gamma}{f_0} \approx -\frac{N_S m_S \omega}{\pi Z_q} \tag{4.3}$$

Since the imaginary part (dissipative term) is negligible in the Sauerbrey limit, the real part is the focus:

$$\Delta f \approx -\frac{N_S m_S \omega}{\pi Z_q} f_0 \tag{4.4}$$

Angular frequency, ω, can be rewritten in terms of frequency, f ($\omega = 2\pi f$):

$$\Delta f \approx -\frac{N_S m_S 2f}{Z_q} f_0 \tag{4.5}$$

Equation 4.5 can be simplified to the Sauerbrey equation (1.1).

The acoustic impedance Z_q of quartz is given by $Z_q = v_q \rho_q$, and can be substituted in:

$$\Delta f = -\frac{2 f N_s m_s}{v_q \rho_q} f_0 \tag{4.6}$$

$f = n f_0$, can also be substituted into the equation:

$$\Delta f = -\frac{2 n f_0^2 N_s m_s}{v_q \rho_q} \tag{4.7}$$

The sensitivity constant, C (1.2), can be substituted into the simplified frequency change equation:

$$\Delta f = -\frac{n N_s m_s}{C} \tag{4.8}$$

$N_s m_s$ represents the change in mass per unit area, Δm_f:

$$\Delta m = -C \frac{\Delta f}{n} \tag{4.9}$$

The Sauerbrey equation indicates that the negative frequency shift observed in a QCM arises from the mass loading of adsorbed particles, in accordance with the Sauerbrey limit for small adsorbed objects. This model applies when the adhered particles are small compared to the sensor's resonance frequency.

Particle size plays a critical role in determining the intrinsic resonance frequency (ω_S) of the particles. Nanometre-sized particles, owing to their low mass and high effective stiffness, exhibit high resonance frequencies, thereby satisfying the condition $\omega_S \gg \omega$. In this regime, the fundamental frequency shift is primarily governed by mass loading. In contrast, larger particles such as bacteria have lower intrinsic resonance frequencies due to their greater mass and deformability. Consequently, the QCM-D response for bacteria is significantly influenced by local viscoelastic properties, leading to elastic loading effects and, in some cases, even positive frequency shifts. This distinction underscores the importance of considering both inertial and elastic loading effects when interpreting QCM-D data from biological systems [190, 248].

Therefore, under the condition $\omega_S \gg \omega$, equation 4.1 reduces to the Sauerbrey equation, where the frequency shift is primarily attributable to the added mass of small particles. For nanometre-sized particles, this implies a direct correlation between the observed negative frequency shift and mass deposition, whereas deviations from this behaviour, such as those observed with bacterial samples, reflect the influence of additional viscoelastic factors.

Elastic Loading:

In the elastic loading regime, where $\omega \gg \omega_S$, the term $\frac{\omega^2}{\omega_s^2}$ becomes very large. Using the Taylor expansion, the denominator in equation 4.1, $1 - \frac{\omega^2}{\omega_s^2}$, becomes approximately:

$$\frac{1}{1 - \frac{\omega^2}{\omega_s^2}} \approx -\frac{\omega_s^2}{\omega^2} \tag{4.10}$$

Using this result, equation 4.1 becomes:

$$\frac{\Delta f + i\Delta\Gamma}{f_0} \approx \frac{-N_s m_s \omega}{\pi Z_q} \cdot -\frac{\omega_s^2}{\omega^2} \tag{4.11}$$

This simplifies to:

$$\frac{\Delta f + i\Delta\Gamma}{f_0} \approx \frac{N_s m_s \omega_s^2}{\pi Z_q \omega} \tag{4.12}$$

To express this in a form consistent with the stiffness of the sphere-plate contact κ_S, the relation $\kappa_S = m_S \omega_S^2$ can be applied:

$$\frac{\Delta f + i\Delta\Gamma}{f_0} \approx \frac{1}{\pi Z_q} \frac{N_s k_s}{\omega} \tag{4.13}$$

- κ_S: Stiffness of the sphere-plate contact (N/m)

This derivation shows how the elastic loading equation is obtained from the coupled resonance model, highlighting the dependence on the stiffness of the contact and the resonance properties of the system. In this form, it is demonstrated that the frequency shift (Δf) in the elastic loading regime depends on the stiffness of the contact (κ_S), the number density of the spheres (N_S) and is inversely proportional to the resonance frequency of the crystal (ω).

Note the negative sign in Eq.4.1 is accounted for in the complex notation of Eq. 4.11-4.12, indicating that a higher particle resonance (ω_S) leads to a negative Δf (added inertial mass), whereas a much lower ω_S (elastic loading) leads to a positive Δf. Eq. 4.13 describes the scenario where large particles are attached to the sensor via a weak bridge, resulting in a positive frequency shift. Large (micron-sized) particles have lower or comparable resonance frequencies ($\omega_S \leq \omega$), leading to positive frequency shifts due to elastic loading. The particles do not move significantly but exert a restoring force, increasing the system's stiffness. Positive frequency shifts depend on the stiffness of the contact (κ_S) and the number density of the particles (N_S), rather than mass.

The coupled resonance theory provides a framework for interpreting QCM-D data. It captures the dynamic interplay between the adhering particles and the sensor surface, offering insights into both frequency shifts and energy dissipation. The distinction between small and large particles, and their respective influence on frequency shifts, highlights the importance of

the coupled resonance model in explaining both negative and positive frequency shifts observed in QCM-D experiments.

The silica deposition QCM-D experiments showed positive Δf values in all experiments. According to traditional QCM-D understanding as a mass balance, such positive frequency shifts should not occur. However, positive Δf have been observed when large particles are loosely attached to a surface. Pomorska *et al.* were the first to report positive Δf for micrometre-sized particles on the crystal surface in liquid, aligning their results with the coupled-oscillator theory. Subsequent studies have documented the impact on colloidal particles.[250–252] In this scenario, positive frequency shifts are interpreted as a force balance indicating the stiffness of the sphere-crystal contact.

Silica particles were chosen to be within the micrometre-size range to mimic the dimensions and morphology of the previously examined bacterial cells. This size range is, incidentally, essential for the manifestation of positive Δf as per the coupled-oscillator theory, suggesting that the observed positive Δf in the results could indeed be attributed to the coupled oscillator effect.

The Δf values can be plotted against the overtone order to determine if the coupled-resonance model is applicable to QCM-D data. The overtone, n, signifies the crystal's operating frequency. Coupled-resonance occurs when the sensor's frequency surpasses that of the depositing particles. Hence, if n is sufficiently low, the crystal's resonant frequency will be too low to induce coupled-resonance, resulting in typical QCM-D behaviour and negative Δf shifts at low harmonics. Although often excluded in data analysis, the first overtone can therefore be useful in identifying coupled-resonance. As n increases, the sensor's frequency exceeds that of the depositing particles, and positive Δf shifts can be observed due to coupled-resonance occurring at higher overtones.

The Δf values from the individual experiments at the 5-h point, after signal stabilisation, were plotted against their respective overtones to explore variations based on sensor frequency (Fig. 4.6). The associated errors suggest that the data are reproducible. The resulting graph indicates that negative Δf occurs at $n = 1$ and positive Δf at $n \geq 3$, suggesting the presence of coupled-resonance. The corresponding time-averaged ΔD values demonstrate a decrease with increasing overtone for higher concentrations. Although coupled-resonance is likely to be occurring, implying that the QCM-D results relate to bond strength rather than deposited mass, the plots indicate a significant concentration effect on both Δf and ΔD. Higher colloid concentrations result in greater magnitudes of Δf and ΔD, aligning with the equation describing coupled-resonance (Eq. 4.13), which states that an increase in particle surface density leads to a higher Δf.

The ratio of Δf values for the three concentrations and their respective overtones is not

constant, indicating that Δf is influenced by more than just particle concentration. The equation (Eq. 4.13) demonstrates that Δf is also dependent on the stiffness of the particle-substrate bond. This implies that bond stiffness varies across experiments differing only in particle concentration. Specifically, in the coupled-resonance regime, Δf and bond stiffness are proportional.

Another method of displaying the data is through the *df* plots, illustrated in Fig. 4.7. Unlike the distinct profiles observed when comparing various bacteria in different environments (Chapter 3), a consistent pattern is noticeable across all three concentrations. Generally, the $n = 1$ results show a negative slope, indicating the negative Δf throughout the experiments. Significant fluctuations are observed for the lowest concentration of 0.25 wt.%. As mentioned earlier, lower overtones are more prone to noise and artifacts. Apart from this, no significant changes occur in the long term for other overtones at all three concentrations. This is expected after colloid deposition finishes at approximately 20 min and signal stabilisation occurs. Higher overtones, however, exhibit positive slopes, corresponding to the positive Δf in all the plots. Thus, these *df* plots provide an alternative visualisation method to easily identify coupled resonance, which can be easily identified at all three concentrations.

Although bacterial cells are also approximately micrometer sized, the coupled-resonance effect was not broadly seen in the bacteria QCM-D data described in Chapter 3. The negative Δf for $n = 1$, and positive Δf for all other overtones was not observed in any of the data. One exception is the data for the two *S. aureus* strains, ATCC 6538™and SH1000-GFP, in TSB, seen in Fig. 4.8. In the QCM-D experiments with *S. aureus* in TSB, the frequency response exhibits a distinct progression, as described in Section 3.1.2. During the initial phase (approximately 0–7 hours), Δf increases, which is indicative of a weak, elastic attachment where only a few reversible bonds are formed. This early stage is characterised by a loosely adhered bacterial layer, in which the interaction is dominated by elastic loading and the associated viscoelastic damping. This transient positive peak in Δf is likely marking the transition from weak, elastic bonding to a stronger, more irreversible adhesion state. At this point, EPS production is thought to be initiated to facilitate the establishment of a stronger, more permanent bond between the cells and the substrate. As EPS accumulates and bonds strengthen, the loading condition shifts toward an inertial regime, resulting in a subsequent decrease Δf in as the biofilm matures.

The $n = 1$ data were plotted (Fig. 4.8) to determine whether the characteristic negative frequency shift of the fundamental frequency contrasts with the positive shifts observed in the higher overtones. Interestingly, the Δf at $n = 1$ is also positive, differing from the colloidal system. One possible explanation for the coupled-resonance regime occurring in TSB is that the high nutrient environment not only facilitates enhanced attachment and multiplication of bacteria but also alters bacterial physiology in a manner that affects QCM-D measurements. In addition to the increased viscosity of TSB, which raises the overall damping (γ) in the system and enhances the elastic loading effect [166], the nutrient-rich medium stimulates higher

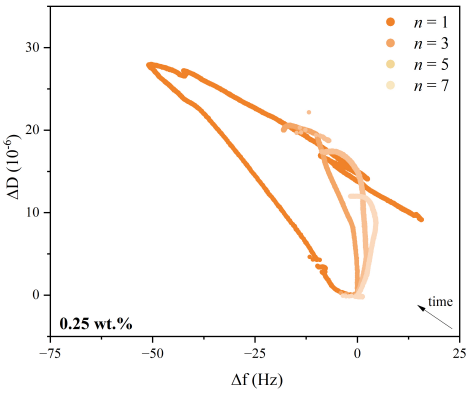

(a) Frequency

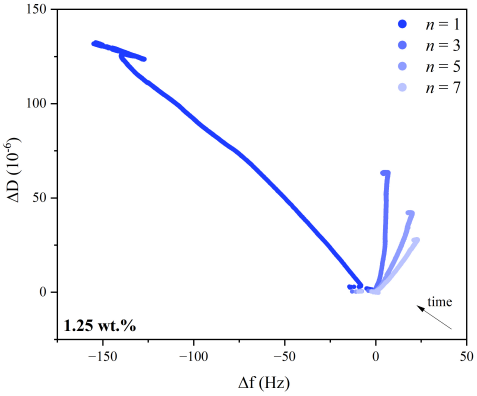

(b) Dissipation

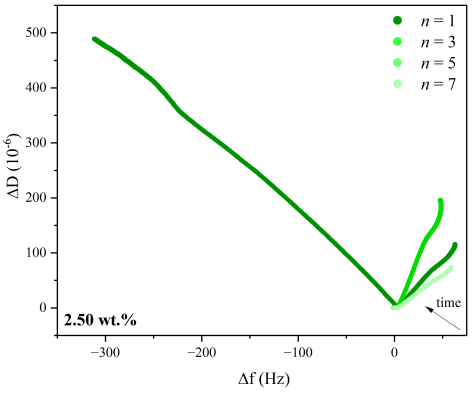

(c) Dissipation

Figure 4.7: Dissipation versus frequency (df) plots of the individual colloid deposition experiments at the three concentrations: 0.25 wt.% (a), 1.25 wt.% (b), 3.50 wt.% (c).

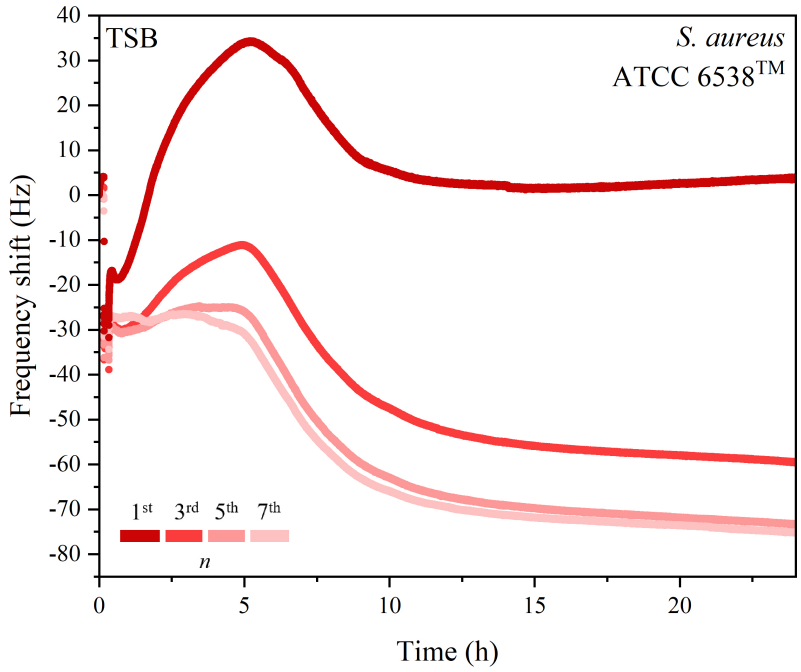

(a) ATCC 6438™

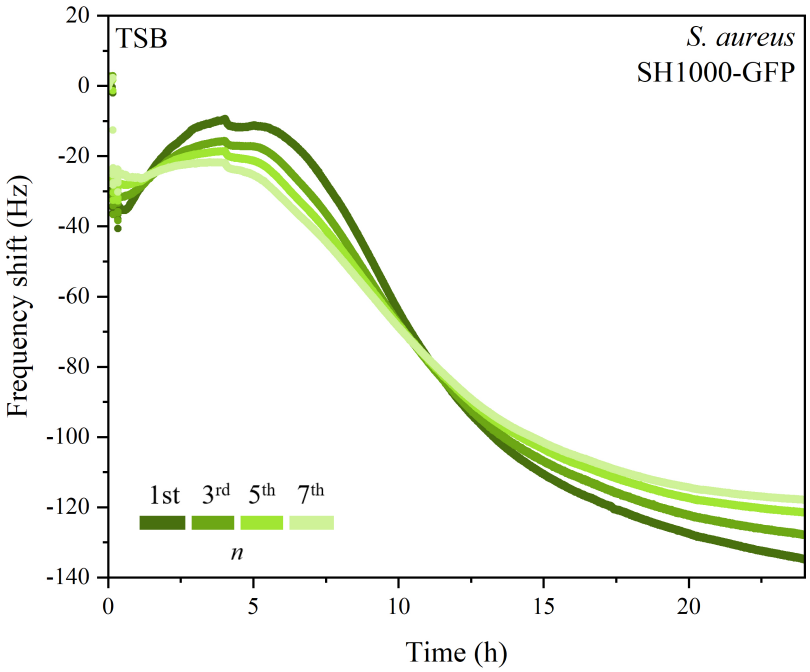

(b) SH1000-GFP

Figure 4.8: QCM-D Δf data for two strains of *S. aureus*, ATCC 6538™and SH1000-GFP, in TSB over time. Both strains exhibit coupled-resonance regimes, demonstrated by positive Δf. Fundamental frequency, $n = 1$, is included to compare its behaviour to the higher overtones.

metabolic activity and EPS production [91, 253]. These biological responses introduce significant viscoelastic damping, a factor largely absent in inert colloids. The viscoelastic damping in the bacterial layer generates a restoring force that effectively increases the sensor's resonance frequency. Consequently, even the fundamental frequency exhibits a positive Δf shift, reflecting that the deposit's elastic properties override the simple mass-loading contribution. This combined effect may place bacterial adhesion within the elastic loading regime (Eq. 4.13), resulting in positive frequency shifts across all overtones. This indicates that bacterial adhesion is governed not only by mass loading but also by changes in the film's viscoelastic properties

4.5 Conclusions

This chapter explored bacterial adhesion from a colloidal physics perspective by comparing the surface attachment of living bacteria to that of inert colloidal particles. The goal was to discern which aspects of bacterial adhesion can be explained by conventional colloid theory and where biological complexity causes deviations. The key finding is that while bacteria can be conceptually treated as "living colloids" to some extent, their attachment behaviour is not identical to non-living particles, due to additional interactions (e.g. active motility, cell-cell adhesion, and extracellular polymer production). The side-by-side experiments with silica microspheres versus *S. aureus* cells highlighted both similarities and critical differences in deposition mechanisms.

Microscopic deposition patterns starkly contrasted between colloids and bacteria. Under identical conditions (gold surface, equivalent particle/cell concentrations, and incubation times), silica colloids deposited as a fairly uniform monolayer of individual spheres. In other words, the inert particles adhered independently and evenly across the surface. *S. aureus* cells, in contrast, showed significant clustering on the surface, accumulating in multi-cell aggregates rather than isolating evenly. This aggregation of bacteria, absent for the colloids, indicates that biological factors drive the cells to attach near one another, forming microcolonies. Likely contributors to this behaviour are quorum-sensing and cell–cell adhesion molecules that encourage bacteria to congregate, as well as surface proteins that cause cells to stick together. Such mechanisms have no counterpart in simple colloidal physics. For instance, *S. aureus* produces adhesins that promote coaggregation, and cell signalling can induce communal behaviour, whereas silica spheres have only physicochemical forces acting on them. The observation of bacterial clumping aligns with the concept that bacteria are not independent particles but communicate and interact as they attach. This is supported by literature on biofilm initial stages, where cells often attach in groups to initiate microcolony formation rather than purely random deposition[216]. In short, bacterial surface colonisation is influenced by biology (cell-cell interactions, signalling, etc.), leading to heterogenous, clustered attachment, whereas colloidal particles follow a more uniform, dispersion-limited deposition pattern.

QCM-D measurements further underscored the differences in how colloids versus bacteria interact with a surface. For silica colloids, the QCM-D frequency and dissipation responses were dominated by a coupled resonance effect. Specifically, anomalous positive frequency shifts at higher overtones (n $\geq$ 3) were observed when silica microspheres attached. Instead of the expected Sauerbrey-type frequency decrease from added mass, the resonant frequency increased at certain harmonics, a clear signature that the particles and the quartz sensor were oscillating in tandem as a coupled system. This phenomenon is well-documented in QCM literature: when a rigid particle attaches to the sensor with finite contact stiffness, the system can behave like two coupled oscillators, leading to upward frequency shifts if the particle's natural resonance is below that of the crystal[190]. In this case, the silica spheres (1 µm) acted as small resonators on the surface, and the magnitude of the positive Δf correlated with particle density (higher colloid concentrations yielded more pronounced positive shifts). These findings match theoretical predictions and prior studies of micrometer-sized particles on QCM-D. The implication is that for colloidal deposits, the QCM-D signal is influenced not just by mass loading but by the mechanical stiffness of the particle-surface contacts and resonance coupling. This complicates direct interpretation of frequency changes in terms of "mass of particles attached," since a stiffer bond or certain particle resonance can actually increase frequency. In summary, the inert colloids provided a clear example where QCM-D deviates from simple mass sensing due to physical resonance effects.

For the bacteria, the QCM-D responses were notably different despite some superficial resemblances. *S. aureus* did occasionally show transient positive frequency peaks in the QCM-D data, including on the fundamental overtone. during the very early stages of attachment. However, these positive shifts were short-lived and much smaller in magnitude than those of the silica colloids. Unlike the colloids, the bacterial frequency shifts did not remain positive at higher overtones, instead, the QCM-D traces for bacteria quickly transitioned to the sustained negative frequency shifts characteristic of soft biofilm accumulation. In other words, any coupled-resonance effect with whole bacterial cells was transient and soon overwhelmed by the viscoelastic loading from biofilm growth. Bacterial attachment led to a complex QCM-D signature, an initial minor increase, followed by a significant drop in frequency accompanied by increasing dissipation as the cells produced extracellular matrix and formed a hydrated biofilm layer. This contrasts sharply with the colloids, where dissipation remained low and frequency shifts could be positive for extended periods. The fact that the bacteria's fundamental frequency also showed a peak (whereas silica's fundamental did not) suggests that the bacterial layer, even when starting to behave colloid-like, was never as strictly rigidly coupled as the silica case. Instead, the presence of soft biofilm components (EPS, cell surface appendages) and the cells' propensity to move or adjust on the surface introduced additional energy dissipation and non-rigid behaviour early on. This finding supports the idea that bacteria cannot be treated as ideal spherical colloids after the moment of initial contact because their biology (growth, polymer secretion, surface motility) quickly adds viscoelastic characteristics to the layer. Indeed, by the time microcolonies form,

the QCM-D response is governed by the properties of a growing biofilm, rather than discrete particles.

Ultimately, the comparison revealed that coupled resonance effects, which dominated the QCM-D signal for rigid colloids, were present but not dominant for bacteria. The silica particle data showed that one must be cautious interpreting QCM-D purely in terms of mass for any particulate adhesion scenario. In the bacterial case, however, biological processes quickly mitigated these resonance artifacts: the growth of a softer viscoelastic film meant the QCM-D frequencies for bacteria settled into the negative domain expected for mass loading, and dissipation rose due to energy losses in the deformable biofilm. Therefore, direct quantitative comparison between the colloidal and bacterial QCM-D data is not straightforward because the bacteria's signal is a convolution of both physicochemical and biological factors, whereas the colloid's signal, while simpler in lacking biology, is complicated by resonance physics. These findings reinforce what has been suggested in prior literature: basic colloid theories (like DLVO and elastic coupling models) can approximate certain aspects of bacterial initial adhesion, but they fail to account for the active and adaptive nature of living cells. For instance, bacteria can regulate their surface properties, produce sticky polymers, or move, none of which a silica bead can do. As a result, while a bacterium in suspension might be treated as a colloidal particle in terms of size and surface charge, once it contacts a surface it behaves in a far more complex manner.

In conclusion, the QCM-D analysis of colloidal particle deposition versus bacterial adhesion provided valuable mechanistic insights. It demonstrated that purely physicochemical interactions (as probed by inert colloids) are only part of the story in biofilm formation. Colloidal models are useful but limited: they highlighted phenomena like resonance coupling that also appear transiently with cells, but they cannot reproduce the full timeline of biofilm development. Bacteria were shown to exhibit additional adhesion dynamics governed by biological forces and interactions absent in inert colloids, confirming that bacteria are colloidal entities subject to regulation and change by metabolism and signalling. These conclusions are supported by existing studies that compare microbial adhesion to colloid theory and that emphasise how extracellular polymers and active processes give biofilms unique properties distinct from abiotic particle layers. Importantly, this work underscores that when interpreting QCM-D data for biofilms, coupled resonance artifacts and the evolving viscoelastic nature of the biological layer must be taken into account. Ignoring either aspect could lead to misestimation of attached "mass" or misunderstanding of the adhesion mechanism. By merging concepts from colloid science with biological knowledge, one can better decipher early bacterial adhesion events. This has practical implications: for example, designing anti-fouling surfaces or coatings might involve disrupting the initial physicochemical attachment (as one would for colloids) and interrupting the subsequent biological aggregation (e.g. by targeting QS or matrix formation). Thus, Chapter 4 bridged colloid physics and microbiology, highlighting both the utility and the pitfalls of treating bacteria as colloidal particles in biophysical analyses.

Chapter 5

Conclusions

This thesis has aimed to collectively advance understanding of how bacteria colonise surfaces by integrating biological experiments with biophysical analyses. Using *S. aureus* and *P. aeruginosa* as model organisms, we examined the steps from initial adhesion to mature biofilm formation under various conditions, and we probed how interfering with bacterial communication or using colloidal analogues can alter these processes. Key findings from the research are discussed below.

QCM-D was demonstrated to be a robust tool to monitor early bacterial attachment and biofilm growth in real time. It reliably detected adhesion events and viscoelastic changes even in complex media, and those signals were corroborated by traditional biofilm assays (crystal violet biomass measurements) and imaging (fluorescence microscopy, AFM). The successful application of QCM-D here confirms its value for biofilm studies, complementing more established end-point measurements. QCM-D was showed to distinguish between different growth conditions, for instance, revealing strong biofilm formation in nutrient-rich media versus negligible growth in nutrient-poor conditions, which underscores its sensitivity to biologically relevant changes. This contributes to the broader literature by validating QCM-D's capability to study live biofilm development over extended periods and by highlighting the importance of using multiple analytical methods to get a complete picture of biofilm state.

Nutrient availability and temperature were confirmed as crucial determinants of biofilm behaviour. The results showed that both *S. aureus* and *P. aeruginosa* form significantly thicker, more biomass-rich biofilms in a high-nutrient environment (TSB) compared to minimal media, which is consistent with known biofilm physiology that nutrients fuel EPS production and growth. Likewise, it was found that incubation at body temperature (37 °C) accelerates adhesion and biofilm initiation, whereas room temperature (25 °C) leads to slower accumulation but denser final biofilms. This finding is particularly relevant to real-world scenarios: in the human host, bacteria may rapidly form biofilms, a concern for infections on implants or tissues, while in cooler environments like water systems, biofilms might develop more gradually but still become resilient. The observations align with reports that temperature shifts induce substantial changes in biofilm structure and composition[221]. These results reinforce the biological principle that

biofilm formation is highly context-dependent, adapting to the surrounding environment. For researchers and practitioners, this emphasises the need to consider environmental parameters when assessing biofilm risks or designing control strategies. For example. disinfectant protocols might need adjustment for different temperatures or nutrient conditions.

Distinct biofilm formation strategies between a Gram-positive coccus (*S. aureus*) and a Gram-negative rod (*P. aeruginosa*) were uncovered. *S. aureus* tends to rapidly accumulate on surfaces, forming multilayered clusters held together by its secreted matrix and cell–cell adhesion factors. This resulted in QCM-D signatures characteristic of a soft, viscoelastic film, notably higher energy dissipation and a detectable transition from initial reversible attachment to irreversible anchoring. In contrast, *P. aeruginosa* exhibited a more gradual, evenly spread attachment with lower dissipation, consistent with a thinner and stiffer biofilm layer. These differences were attributed to the bacteria's biology: *P. aeruginosa* is motile (flagella, pili) and can actively modulate its attachment, whereas *S. aureus* relies on passive adhesion and rapid clumping. Indeed, the presence of flagella in *P. aeruginosa* is known to influence its initial attachment and subsequent biofilm architecture[216], leading to a more spread-out community, whereas *S. aureus* propensity for microcolony formation leads to a thicker but more heterogeneous biofilm. Importantly, by using both a common lab *S. aureus* strain (ATCC 6538™) and a GFP-tagged variant (SH1000-GFP), these characteristics were showed to not be strain-specific peculiarities but general features of *S. aureus* biofilms, strengthening the conclusion that *S. aureus* biofilm mechanics (e.g. the reversible-to-irreversible attachment peak) are reproducible traits of the species. The comparative approach thus adds to the body of knowledge by directly illustrating how two different bacteria employ different biophysical strategies for surface colonisation, a point supported by other studies contrasting biofilms of various species. Recognising such differences is important for tailored anti-biofilm approaches, what works to remove or prevent a P. *aeruginos*a biofilm (perhaps targeting motility or specific polysaccharides) might differ from what works against *S. aureus* (targeting its clumping or matrix).

A novel aspect of this work was investigating how interfering with bacterial QS affects biofilm formation in real time. Using the *agr* system inhibitor savirin, it was found that blocking QS in *S. aureus* significantly alters its biofilm growth dynamics. Savirin-treated *S. aureus* showed delayed biofilm maturation, the QCM-D indicated prolonged initial attachment with a postponed transition to heavy biofilm accrual. Correspondingly, confocal microscopy showed that early biofilm layers formed under savirin were similar in cell density to untreated biofilms, but the later expansion and tower formation were stunted. These results provide direct evidence that the *agr*-mediated QS circuit accelerates normal biofilm development after a certain point (approximately 5–6 hours into formation in this system), and that chemically disrupting this signal keeps the bacteria in a quasi-adhesive state longer. Biologically, this makes sense: *agr* in *S. aureus* upregulates enzymes and surfactants that typically facilitate biofilm restructuring and eventual dispersal[234], by inhibiting AgrA with savirin, those processes are blunted, yielding

a flatter, less mature biofilm. These findings are in line with emerging literature that views QS inhibitors as anti-virulence and anti-biofilm agents. For example, other studies have shown that *agr* inhibitors like savirin can reduce *S. aureus* pathogenicity in animal infection models without killing the bacteria[237]. Here that concept is extended to the biofilm context, as savirin not only reduces toxin production (as known from prior work) but also tangibly impacts the physical characteristics of a biofilm, which could enhance susceptibility to antibiotics or immune clearance. This highlights a broader implication - targeting bacterial communication pathways can modulate biofilm formation in ways that might complement traditional antibiotics. It opens avenues for designing therapies that disarm biofilms, making them easier to remove, rather than trying to destroy bacteria outright, potentially mitigating resistance. The real-time data pinpoint the window during which such interventions are most effective, information that could guide scheduling of combined treatments, for example adding a QS blocker early, then a biofilm-disrupting agent or antibiotic later.

By incorporating colloidal particle deposition experiments, a biophysical perspective was added to interpret bacterial adhesion. It was found that many initial aspects of bacterial adhesion could be qualitatively mimicked by silica microspheres (size on the order of bacterial cells), but critical differences arose from the "living" nature of bacteria. The colloids helped illustrate certain physical phenomena in QCM-D (like coupled resonance) that are also relevant when interpreting bacterial adhesion data[190]. However, the bacteria deviated from colloidal behaviour as soon as biological processes kicked in, for instance, bacteria exhibited aggregation (cluster formation) on surfaces, whereas colloids did not, and bacteria generated a viscoelastic biofilm matrix that colloids obviously lack. The overall conclusion is that while basic colloid models (e.g. DLVO theory for initial attraction/repulsion forces) can describe the early physics of adhesion, they fail to capture time-dependent biological changes like growth, polymer secretion, and active movement. The side-by-side comparison, therefore, reinforces the idea that bacteria behave as "active colloids", they obey physical principles but also continuously modify their environment. This finding is supported by discussions in the literature that bacteria in biofilms exhibit colloid-like behaviour up to a point, after which extracellular polymeric substances and physiology dominate. For researchers, this means that one can use colloidal particles as a convenient model to study certain aspects of adhesion, but caution must be taken not to overgeneralise those results to biological systems. For practitioners (e.g. in industrial biofouling contexts), it suggests that anti-fouling strategies effective against non-living particles (like simply making a surface super-smooth or charge-neutral to deter particle sticking) may not suffice against bacteria, which can produce glue-like substances and aggregate actively.

The interdisciplinary approach of this thesis, combining microbiology (biofilms, quorum sensing) with biophysics (QCM-D, colloid theory), yielded a more nuanced understanding of biofilm formation. Biologically, the work provides insight into how a major Gram-positive pathogen (*S. aureus*) and a major Gram-negative pathogen (*P. aeruginosa*) differ in colonisation tactics, and

how those tactics can be influenced or disrupted. This has implications for infection control: knowing that *S. aureus* biofilms can be "locked" in an early phase by QS inhibitors, for example, could inform new treatments for *S. aureus* device-related infections by combining QS inhibition with mechanical or chemical biofilm removal at a strategic time. Likewise, understanding that *P. aeruginosa* biofilms are initially more rigid and reliant on motility could guide the design of surfaces or drugs that target those early mechanisms, for instance, coatings that interfere with flagellar attachment or initial EPS deposition. From a biophysical standpoint, these findings emphasise the importance of accounting for viscoelastic and active effects when analysing microbial adhesion. The observation of coupled resonance in colloids but not dominating in bacteria is a reminder that measuring "mass" of attached biomass with QCM-D isn't straightforward – researchers must use models that include elasticity of contacts and the rheology of biofilms[190]. This contributes to the field of biointerfacial science by providing a case study where physical modelling and biological reality intersect.

While this thesis has answered several important questions, it also opens up new avenues. One limitation is that QCM-D measurements, while informative, provide aggregate signals and they cannot alone pinpoint molecular details of the biofilm. Future work could combine QCM-D with real-time microscopy or spectroscopy to directly observe EPS production or gene expression concurrently with adhesion signals. Additionally, expanding the colloidal comparison to other shapes or to "soft colloids" (e.g. hydrogel beads that mimic the softness of bacteria) could further bridge the gap between model particles and living cells, refining our understanding of the physics–biology interface in biofilms. From a microbiological perspective, investigating other QS inhibitors or biofilm-disrupting compounds in the QCM-D setup would be valuable, for example, does targeting *P. aeruginosa* QS or second messenger systems produce a measurable delay in biofilm formation akin to the savirin effect in *S. aureus*? And how do mixed-species biofilms (which are common in nature) behave in such QCM-D analyses. Do they show intermediate characteristics or dominant traits of one species? These questions are pertinent for both fundamental science and practical control of biofilms. The broader impact of this research lies in its potential applications: improving anti-biofilm coatings for medical implants, optimising cleaning protocols in industries by knowing when biofilms are weakest, and guiding the use of anti-virulence drugs to manage chronic infections. By elucidating how early adhesion can be quantified and influenced, we contribute knowledge that could help mitigate biofilm-related problems, which are ubiquitous from hospital settings (infections on catheters, prosthetics) to environmental systems (biofouling of membranes, pipes). In conclusion, the work presented in this thesis underscores the complexity of bacterial adhesion, a process governed by an interplay of physicochemical forces and biological regulation.

Bibliography

(1) R. H. Deurenberg and E. E. Stobberingh, *Infect. Genet. Evol.*, 2008, **8**, 747–763.

(2) L. G. Harris, S. J. Foster and R. G. Richards, *Eur. Cells Mater.*, 2002, **4**, 39–60.

(3) S. Y. C. Tong, J. S. Davis, E. Eichenberger, T. L. Holland and V. G. Fowler, *Clin. Microbiol R.ev.*, 2015, **28**, 603–661.

(4) A. Sakr, F. Brégeon, J.-L. Mège, J.-M. Rolain and O. Blin, *Front. Microbiol.*, 2018, **9**.

(5) J.-L. Sun, S. Zhang, X.-X. Chen, J.-Y. Chen and B.-Z. Han, *Afr. J. Microbiol. Res.*, 2012, **6**, 3284–3291.

(6) F. D. Lowy, *J. Clin. Investig.*, 2003, **111**, 1265–1273.

(7) L. D. Sabath, M. Laverdiere, N. Wheeler, D. Blazevic and B. Wilkinson, *Lancet*, 1977, **309**, 443–447.

(8) S. Stefani, D. R. Chung, J. A. Lindsay, A. W. Friedrich, A. M. Kearns, H. Westh and F. M. MacKenzie, *Int. J. Antimicrob. Agents*, 2012, **39**, 273–282.

(9) M. C. Enright, D. A. Robinson, G. Randle, E. J. Feil, H. Grundmann and B. G. Spratt, *Proc. Natl. Acad. Sci. U.S.A.*, 2002, **99**, 7687–7692.

(10) M. Otto, *Cell. Microbiol.*, 2012, **14**, 1513–1521.

(11) S. Brown, J. P. S. Maria and S. Walker, *Annu. Rev. Microbiol.*, 2013, **67**, 313–336.

(12) S. J. Kim, J. Chang and M. Singh, *Biochim. Biophys. Acta. Biomembr.*, 2015, **1848**, 350–362.

(13) T. J. Foster, J. A. Geoghegan, V. K. Ganesh and M. Höök, *Nat. Rev. Microbiol.*, 2014, **12**, 49–62.

(14) T. J. Foster, *Microbiol. Spectr.*, 2019, **7**.

(15) A. Peix, M.-H. Ramírez-Bahena and E. Velázquez, *Infect. Genet. Evol.*, 2009, **9**, 1132–1147.

(16) A. J. Spiers, A. Buckling and P. B. Rainey, *Microbiology*, 2000, **146**, 2345–2350.

(17) J.-M. Meyer, *Arch. Microbiol.*, 2000, **174**, 135–142.

(18) I. L. Lamont and L. W. Martin, *Microbiology*, 2003, **149**, 833–842.

(19) E. Deligianni, S. Pattison, D. Berrar, N. G. Ternan, R. W. Haylock, J. E. Moore, S. J. Elborn and J. S. Dooley, *BMC Microbiol.*, 2010, **10**, 38.

(20) M. E. Ojewumi, J. O. Okeniyi, J. O. Ikotun, E. T. Okeniyi, V. A. Ejemen and A. P. I. Popoola, *Data Br.*, 2018, **19**, 101–113.

(21) G. Young, *J. Bacteriol. Res.*, 1947, **54**, 109–117.

(22) J. Botelho, F. Grosso and L. Peixe, *Drug Resist. Updat.*, 2019, **44**, 100640.

(23) Z. Pang, R. Raudonis, B. R. Glick, T.-J. Lin and Z. Cheng, *Biotechnol. Adv.*, 2019, **37**, 177–192.

(24) J. A. Driscoll, S. L. Brody and M. H. Kollef, *Drugs*, 2007, **67**, 351–368.

(25) D. Reynolds and M. Kollef, *Drugs*, 2021, **81**, 2117–2131.

(26) H. P. Hahn, *Gene*, 1997, **192**, 99–108.

(27) G. A. O'Toole and R. Kolter, *Mol. Microbiol.*, 1998, **30**, 295–304.

(28) L. L. Burrows, *Annu Rev Microbiol*, 2012, **66**, 493–520.

(29) M. Semmler, E. K. Mann, J. Rička and M. Borkovec, *Langmuir*, 1998, **14**, 5127–5132.

(30) Y.-L. Shih and L. Rothfield, *Microbiol Mol Biol Rev*, 2006, **70**, 729–754.

(31) M. T. Cabeen and C. Jacobs-Wagner, *J Cell Biol*, 2007, **179**, 381–387.

(32) V. Nieto, A. R. Kroken, M. R. Grosser, B. E. Smith, M. M. E. Metruccio, P. Hagan, M. E. Hallsten, D. J. Evans and S. M. J. Fleiszig, *mBio*, 2019, **10**, e02880–18.

(33) T. J. Beveridge, *J. Bacteriol.*, 1999, **181**, 4725–4733.

(34) B. Jubeh, Z. Breijyeh and R. Karaman, *Molecules*, 2020, **25**, 2888.

(35) M. Rohde, *Microbiol. Spectr.*, 2019, **7**, 10.1128/microbiolspec.gpp3–0044–2018.

(36) Z. Breijyeh, B. Jubeh and R. Karaman, *Molecules*, 2020, **25**, 1340.

(37) A. Gauba and K. M. Rahman, *Antibiotics*, 2023, **12**, 1590.

(38) T.-Y. Liu, Y. Chen, H. Wang, Y. Huang, Y. Chao, K.-T. Tsai, W.-C. Cheng, C. Chuang, Y. Tsai, C. Huang, D.-W. Wang, C.-H. Lin, J. Wang and Y.-L. Wang, *J. Nanosci. Nanotechnol.*, 2012, **12**, 5004–8.

(39) C. Pecoraro, D. Carbone, B. Parrino, S. Cascioferro and P. Diana, *Int J Mol Sci*, 2023, **24**, 4872.

(40) R. Ruhal and R. Kataria, *Microbiological Research*, 2021, **251**, 126829.

(41) I. Grekov, J. G. Thöming, A. Kordes and S. Häussler, *ISME J*, 2021, **15**, 1165–1177.

(42) S. Lewenza, J. Abboud, K. Poon, M. Kobryn, I. Humplik, J. R. Bell, L. Mardan and S. Reckseidler-Zenteno, *PLoS One*, 2018, **13**, e0198384.

(43) C. Berne, C. K. Ellison, A. Ducret and Y. V. Brun, *Nat. Rev. Microbiol.*, 2018, **16**, 616–627.

(44) N. P. Boks, W. Norde, H. C. v. d. Mei and H. J. Busscher, *Microbiology*, 2008, **154**, 3122–3133.

(45) T. Schweinitzer and C. Josenhans, *Arch. Microbiol.*, 2010, **192**, 507–520.

(46) J. Humphries, L. Xiong, J. Liu, A. Prindle, F. Yuan, H. A. Arjes, L. Tsimring and G. M. Süel, *Cell*, 2017, **168**.

(47) H. H. Tuson and D. B. Weibel, *Soft Matter*, 2013, **9**, 4368–4380.

(48) L. Vaccari, M. Molaei, T. H. R. Niepa, D. Lee, R. L. Leheny and K. J. Stebe, *Adv. Colloid Interface Sci.*, 2017, **247**, 561–572.

(49) A. S. Utada, R. R. Bennett, J. C. N. Fong, M. L. Gibiansky, F. H. Yildiz, R. Golestanian and G. C. L. Wong, *Nat. Commun.*, 2014, **5**, 4913.

(50) Y. Ren, C. Wang, Z. Chen, E. Allan, H. C. V. D. Mei and H. J. Busscher, *FEMS Microbiol. Rev.*, 2018, **42**, 259–272.

(51) T. A. Camesano and B. E. Logan, *Environ. Sci. Technol.*, 2000, **34**, 3354–3362.

(52) A.-M. Holban, C. Farcasiu, O.-C. Andrei, A. M. Grumezescu and A.-T. Farcasiu, *Materials (Basel)*, 2021, **14**, 6994.

(53) Y. H. An and R. J. Friedman, *J. Biomed. Mater. Res .*, 1998, **43**, 338–348.

(54) A. I. Hochbaum and J. Aizenberg, *Nano Lett.*, 2010, **10**, 3717–3721.

(55) R. Helbig, D. Günther, J. Friedrichs, F. Rößler, A. Lasagni and C. Werner, *Biomater. Sci.*, 2016, **4**, 1074–1078.

(56) S. Bagherifard, D. J. Hickey, A. C. d. Luca, V. N. Malheiro, A. E. Markaki, M. Guagliano and T. J. Webster, *Biomaterials*, 2015, **73**, 185–197.

(57) E. P. Ivanova, V. K. Truong, H. K. Webb, V. A. Baulin, J. Y. Wang, N. Mohammodi, F. Wang, C. Fluke and R. J. Crawford, *Sci. Rep.*, 2011, **1**, 165.

(58) F. Hizal, N. Rungraeng, J. Lee, S. Jun, H. J. Busscher, H. C. v. d. Mei and C.-H. Choi, *ACS Appl. Mater. Interfaces*, 2017, **9**, 12118–12129.

(59) N. Lu, W. Zhang, Y. Weng, X. Chen, Y. Cheng and P. Zhou, *Food Control*, 2016, **68**, 344–351.

(60) A. Jain and N. B. Bhosle, *Biofouling*, 2009, **25**, 13–19.

(61) K. Zhao, B. S. Tseng, B. Beckerman, F. Jin, M. L. Gibiansky, J. J. Harrison, E. Luijten, M. R. Parsek and G. C. L. Wong, *Nature*, 2013, **497**, 388–391.

(62) A. Nickzad and E. Déziel, *Lett. Appl. Microbiol.*, 2014, **58**, 447–453.

(63) B. M. Martins and J. C. Locke, *Curr. Opin. Microbiol.*, 2015, **24**, 104–112.

(64) K. Amako and A. Umeda, *Microbiol. Immunol.*, 1982, **26**, 113–117.

(65) R. S. Friedlander, H. Vlamakis, P. Kim, M. Khan, R. Kolter and J. Aizenberg, *Proc. Natl. Acad. Sci. U.S.A.*, 2013, **110**, 5624–5629.

(66) D. M. Missiakas and O. Schneewind, *Curr Protoc Microbiol*, 2013, **CHAPTER 9**, Unit–9C.1.

(67) L. M. G. Bui, P. Hoffmann, J. D. Turnidge, P. S. Zilm and S. P. Kidd, *Infect Immun*, 2015, **83**, 470–481.

(68) G. Domingue, J. W. Costerton and M. R. Brown, *FEMS Immunology & Medical Microbiology*, 1996, **16**, 223–228.

(69) J. W. Schmidt, A. Greenough, M. Burns, A. E. Luteran and D. G. McCafferty, *FEMS Microbiol Lett*, 2010, **310**, 104–111.

(70) A. E. LaBauve and M. J. Wargo, *Curr Protoc Microbiol*, 2012, **0 6**, Unit–6E.1.

(71) K. Sauer, P. Stoodley, D. M. Goeres, L. Hall-Stoodley, M. Burmølle, P. S. Stewart and T. Bjarnsholt, *Nat. Rev. Microbiol*, 2022, **20**, 608–620.

(72) L. Yang, J. A. J. Haagensen, L. Jelsbak, H. K. Johansen, C. Sternberg, N. Høiby and S. Molin, *J Bacteriol*, 2008, **190**, 2767–2776.

(73) G. H. W. Bowden and Y. H. Li, *Adv. Dent. Res.*, 1997, **11**, 81–99.

(74) K. Schilcher and A. R. Horswill, *Microbiol. Mol. Biol. Rev.*, 2020, **84**.

(75) L. D. Renner and D. B. Weibel, *MRS Bull.*, 2011, **36**, 347–355.

(76) J. B. Kaplan, *IJAO*, 2011, **34**, 737–751.

(77) N. M. Oliveira, E. Martinez-Garcia, J. Xavier, W. M. Durham, R. Kolter, W. Kim and K. R. Foster, *PLoS Biol.*, 2015, **13**, e1002232.

(78) T.-F. C. Mah and G. A. O'Toole, *Trends Microbiol.*, 2001, **9**, 34–39.

(79) R. M. Donlan, *Clin. Infect. Dis.*, 2001, **33**, 1387–1392.

(80) D. Dufour, V. Leung and C. M. Lévesque, *Int. Endod. J.*, 2010, **22**, 2–16.

(81) K. Lewis, *Nat. Rev. Microbiol.*, 2007, **5**, 48–56.

(82) G. Loss, P. M. Simões, F. Valour, M. F. Cortês, L. Gonzaga, M. Bergot, S. Trouillet-Assant, J. Josse, A. Diot, E. Ricci, A. T. Vasconcelos and F. Laurent, *Front. Cell. Infect. Microbiol.*, 2019, **9**.

(83) G. O'Toole, H. B. Kaplan and R. Kolter, *Annu. Rev. Microbiol.*, 2000, **54**, 49–79.

(84) M. Toyofuku, T. Inaba, T. Kiyokawa, N. Obana, Y. Yawata and N. Nomura, *Biosci. Biotechnol. Biochem*, 2016, **80**, 7–12.

(85) J. D. Bryers and W. G. Characklis, *Biotechnol. Bioeng.*, 1982, **24**, 2451–2476.

(86) V. Carniello, B. W. Peterson, H. C. V. D. Mei and H. J. Busscher, *Adv. Colloid Interface Sci.*, 2018, **261**, 1–14.

(87) H.-C. Flemming, T. R. Neu and D. J. Wozniak, *J. Bacteriol. Res.*, 2007, **189**, 7945–7947.

(88) H.-C. Flemming, *Microorganisms*, 2016, **4**, 41.

(89) L. Yang, Y. Hu, Y. Liu, J. Zhang, J. Ulstrup and S. Molin, *Environ. Microbiol.*, 2011, **13**, 1705–1717.

(90) M. Asally, M. Kittisopikul, P. Rué, Y. Du, Z. Hu, T. Çağatay, A. B. Robinson, H. Lu, J. Garcia-Ojalvo and G. M. Süel, *Proc. Natl. Acad. Sci. U.S.A.*, 2012, **109**, 18891–18896.

(91) M. Otto, *Annu. Rev. Med.*, 2013, **64**, 175–188.

(92) M. B. Miller and B. L. Bassler, *Annu. Rev. Microbiol.*, 2001, **55**, 165–199.

(93) Y.-H. Dong and L.-H. Zhang, *Korean J. Microbiol.*, 2005, **43 Spec No**, 101–9.

(94) C. M. Waters and B. L. Bassler, *Annu. Rev. Cell Dev. Biol.*, 2005, **21**, 319–346.

(95) M. Weber and J. Buceta, *BMC Syst. Biol.*, 2013, **7**, 6.

(96) N. A. Whitehead, A. M. L. Barnard, H. Slater, N. J. L. Simpson and G. P. C. Salmond, *FEMS Microbiol. Rev.*, 2001, **25**, 365–404.

(97) R. P. Novick and E. Geisinger, *Annu. Rev. Genet.*, 2008, **42**, 541–564.

(98) F. Khan, A. Javaid and Y.-M. Kim, *Curr. Drug Targets*, 2019, **20**, 655–667.

(99) D. L. Mould, N. J. Botelho and D. A. Hogan, *mBio*, 2020, **11**.

(100) M. Feoktistova, P. Geserick and M. Leverkus, *Cold Spring Harb. Protoc.*, 2016, **2016**, pdb.prot087379.

(101) L. Boulos, M. Prévost, B. Barbeau, J. Coallier and R. Desjardins, *J. Microbiol. Methods*, 1999, **37**, 77–86.

(102) X. Guo, S. Liu, X. Zhou, H. Hu, K. Zhang, X. Du, X. Peng, B. Ren, L. Cheng and M. Li, *Sci. Rep.*, 2019, **9**, 6689.

(103) Y. Deng, L. Wang, Y. Chen and Y. Long, *BioTechniques*, 2020, **69**, 88–98.

(104) P. Stiefel, S. Schmidt-Emrich, K. Maniura-Weber and Q. Ren, *BMC Microbiol.*, 2015, **15**, 36.

(105) M. Rosenberg, N. F. Azevedo and A. Ivask, *Sci. Rep.*, 2019, **9**, 6483.

(106) C. L. Malone, B. R. Boles, K. J. Lauderdale, M. Thoendel, J. S. Kavanaugh and A. R. Horswill, *J. Microbiol. Methods*, 2009, **77**, 251–260.

(107) M. D. Rodriguez, Z. Paul, C. E. Wood, K. C. Rice and E. W. Triplett, *Front. Microbiol.*, 2017, **8**.

(108) I. Matai, A. Sachdev, P. Dubey, S. U. Kumar, B. Bhushan and P. Gopinath, *Colloids Surf. B*, 2014, **115**, 359–367.

(109) P. M. Pereira, H. Veiga, A. M. Jorge and M. G. Pinho, *Appl. Environ. Microbiol.*, 2010, **76**, 4346–4353.

(110) Y. Y. Pang, J. Schwartz, M. Thoendel, L. W. Ackermann, A. R. Horswill and W. M. Nauseef, *J. Innate Immun.*, 2010, **2**, 546–559.

(111) A. Staats, D. Li, A. C. Sullivan and P. Stoodley, *Ann. Jt.*, 2021, **6**, 43–43.

(112) G. Binnig, C. F. Quate and C. Gerber, *Phys. Rev. Lett.*, 1986, **56**, 930–933.

(113) S. Liu and Y. Wang, *Scanning*, 2010, **32**, 61–73.

(114) A. Alessandrini and P. Facci, *Meas. Sci. Technol.*, 2005, **16**, R65–R92.

(115) M. S. Rana, H. R. Pota and I. R. Petersen, *Asian J. Control*, 2018, **20**, 1379–1399.

(116) T. Ando, T. Uchihashi and N. Kodera, *Annu. Rev. Biophys.*, 2013, **42**, 393–414.

(117) J. T. Blakeman, Ph.D. Thesis, University of Sheffield, 2019.

(118) T. Okajima, H. Sekiguchi, H. Arakawa and A. Ikai, *Appl. Surf. Sci.*, 2003, **210**, 68–72.

(119) I. B. Beech, C. W. S. Cheung, D. B. Johnson and J. R. Smith, *Biofouling*, 1996, **10**, 65–77.

(120) L. Kailas, E. C. Ratcliffe, E. J. Hayhurst, M. G. Walker, S. J. Foster and J. K. Hobbs, *Ultramicroscopy*, 2009, **109**, 775–780.

(121) M. C. Grantham and P. M. Dove, *Geochim. Cosmochim. Acta.*, 1996, **60**, 2473–2480.

(122) T. Hugel and M. Seitz, *Macromol. Rapid Commun.*, 2001, **22**, 989–1016.

(123) E. M. Puchner and H. E. Gaub, *Curr. Opin. Struct. Biol.*, 2009, **19**, 605–614.

(124) J. M. Thwala, M. Li, M. C. Y. Wong, S. Kang, E. M. V. Hoek and B. B. Mamba, *Langmuir*, 2013, **29**, 13773–13782.

(125) T. Shibata, K. Nakamura, S. Horiike, M. Nagai, T. Kawashima, T. Mineta and E. Makino, *Microelectron. Eng.*, 2013, **111**, 325–331.

(126) K. Hyonchol, H. Arakawa, T. Osada and A. Ikai, *Colloids Surf. B*, 2002, **25**, 33–43.

(127) D. Alsteens, E. Dague, P. G. Rouxhet, A. R. Baulard and Y. F. Dufrêne, *Langmuir*, 2007, **23**, 11977–11979.

(128) Y. F. Dufrêne, *Micron*, 2001, **32**, 153–165.

(129) P. Herman, S. El-Kirat-Chatel, A. Beaussart, J. A. Geoghegan, T. J. Foster and Y. F. Dufrêne, *Mol. Microbiol.*, 2014, **93**, 356–368.

(130) E. Brzozowska, A. Leśniewski, S. Sęk, R. Wieneke, R. Tampé, S. Górska, M. Jönsson-Niedziółka and J. Niedziółka-Jönsson, *Sci. Rep.*, 2018, **8**, 10935.

(131) J. Helenius, C.-P. Heisenberg, H. E. Gaub and D. J. Muller, *J. Cell. Sci.*, 2008, **121**, 1785–1791.

(132) A. Beaussart, A. E. Baker, S. L. Kuchma, S. El-Kirat-Chatel, G. A. O'Toole and Y. F. Dufrêne, *ACS Nano*, 2014, **8**, 10723–10733.

(133) M. I. Giannotti and G. J. Vancso, *ChemPhysChem*, 2007, **8**, 2290–2307.

(134) M. Hernando-Pérez, S. Setayeshgar, Y. Hou, R. Temam, Y. V. Brun, B. Dragnea and C. Berne, *mBio*, 2018, **9**.

(135) W. H. King, *Anal. Chem.*, 1964, **36**, 1735–1739.

(136) M. Rodahl, F. Höök, C. Fredriksson, C. A. Keller, A. Krozer, P. Brzezinski, M. Voinova and B. Kasemo, *Faraday Discuss.*, 1997, **107**, 229–246.

(137) Q. Chen, S. Xu, Q. Liu, J. Masliyah and Z. Xu, *Adv. Colloid Interface Sci.*, 2016, **233**, 94–114.

(138) M. Pohanka, *Int. J. Electrochem. Sci.*, 2021, ArticleID:211220.

(139) A. L. Morales-García, Ph.D. Thesis, The University of Sheffield, 2014.

(140) G. Sauerbrey, *Z. Phys.*, 1959, **155**, 206–222.

(141) K. K. Kanazawa and J. G. Gordon, *Anal. Chem.*, 1985, **57**, 1770–1771.

(142) B. D. Vogt, E. K. Lin, W.-l. Wu and C. C. White, *J. Phys. Chem. B*, 2004, **108**, 12685–12690.

(143) J. Hu, G. Yesilbas, Y. Li, X. Geng, P. Li, J. Chen, X. Wu, A. Knoll and T.-L. Ren, *Anal. Chem.*, 2022, **94**, 5760–5768.

(144) N. M. Alves, C. Picart and J. F. Mano, *Macromol. Biosci.*, 2009, **9**, 776–785.

(145) N. R. Hollingsworth, S. I. Wilkanowicz and R. G. Larson, *Soft Matter*, 2019, **15**, 7838–7851.

(146) S. E. Moya and J. Irigoyen, *J. Polym. Sci. B: Polym. Phys.*, 2013, **51**, 1068–1072.

(147) M. V. Voinova, M. Rodahl, M. Jonson and B. Kasemo, *Phys. Scr.*, 1999, **59**, 391–396.

(148) D. Johannsmann, *The quartz crystal microbalance in soft matter research : fundamentals and modeling*, Springer, 2015.

(149) A. Mechler, S. Praporski, K. Atmuri, M. Boland, F. Separovic and L. L. Martin, *Biophysical Journal*, 2007, **93**, 3907–3916.

(150) S. Goka, K. Okabe, Y. Watanabe and H. Sekimoto, *Jpn. J. Appl. Phys.*, 2000, **39**, 3073.

(151) S. Spagnolo, E. S. Muckley, I. N. Ivanov and T. Hianik, *Chemosensors*, 2022, **10**, 143.

(152) S. X. Liu and J.-T. Kim, *J. Lab. Autom.*, 2009, **14**, 213–220.

(153) T. McArdle, T. P. McNamara, F. Fei, K. Singh and C. F. Blanford, *ACS Appl. Mater. Interfaces*, 2015, **7**, 25270–25280.

(154) K. Sadman, C. G. Wiener, R. A. Weiss, C. C. White, K. R. Shull and B. D. Vogt, *Anal. Chem.*, 2018, **90**, 4079–4088.

(155) T. E. Alexander, L. D. Lozeau and T. A. Camesano, *The Cell Surface*, 2019, **5**, 100024.

(156) K. Otto, *Res. Microbiol.*, 2008, **159**, 415–422.

(157) J. Gutman, S. L. Walker, V. Freger and M. Herzberg, *Environ. Sci. Technol.*, 2013, **47**, 398–404.

(158) R. Ripa, A. Shen and R. Funari, *ACS Omega*, 2020, **5**, 2295–2302.

(159) J. Strauss, Y. Liu and T. A. Camesano, *JOM*, 2009, **61**, 71–74.

(160) I. M. Marcus, M. Herzberg, S. L. Walker and V. Freger, *Langmuir*, 2012, **28**, 6396–6402.

(161) D. Yongabi, M. Khorshid, A. Gennaro, S. Jooken, S. Duwé, O. Deschaume, P. Losada-Pérez, P. Dedecker, C. Bartic, M. Wübbenhorst and P. Wagner, *ACS Appl. Mater. Interfaces*, 2020, **12**, 18258–18272.

(162) D. Yongabi, S. Jooken, S. Givanoudi, M. Khorshid, O. Deschaume, C. Bartic, P. Losada-Pérez, M. Wübbenhorst and P. Wagner, *J. Colloid Interface Sci.*, 2021, **585**, 583–595.

(163) X. Jing, Y. Wu, D. Wang, C. Qu, J. Liu, C. Gao, A. Mohamed, Q. Huang, P. Cai and N. M. Ashry, *Environ. Sci. Technol.*, 2022, **56**, 16707–16715.

(164) O. Orgad, Y. Oren, S. L. Walker and M. Herzberg, *Biofouling*, 2011, **27**, 787–798.

(165) A. Sweity, W. Ying, M. S. Ali-Shtayeh, F. Yang, A. Bick, G. Oron and M. Herzberg, *Water Res.*, 2011, **45**, 6430–6440.

(166) A. L. Olsson, H. C. van der Mei, H. J. Busscher and P. K. Sharma, *J. Colloid Interface Sci.*, 2011, **357**, 135–138.

(167) A. L. J. Olsson, H. C. van der Mei, H. J. Busscher and P. K. Sharma, *Langmuir*, 2009, **25**, 1627–1632.

(168) K. Otto, H. Elwing and M. Hermansson, *J Bacteriol*, 1999, **181**, 5210–5218.

(169) A. Tarnapolsky and V. Freger, *Anal Chem*, 2018, **90**, 13960–13968.

(170) D. Yongabi, M. Khorshid, C. Korbas, P. Losada-Pèrez, S. Givanoudi, S. Jooken, F. Ahmed Sadiq, C. Bartic, M. Wübbenhorst, M. Heyndrickx and P. Wagner, *Phys. Status Solidi A*, 2023, **220**, 2300310.

(171) L. D. Lozeau, T. E. Alexander and T. A. Camesano, *J. Phys. Chem. B*, 2015, **119**, 13142–13151.

(172) M. Hermansson, *Colloids and Surfaces B: Biointerfaces*, 1999, **14**, 105–119.

(173) C. K. Lee, J. Vachier, J. de Anda, K. Zhao, A. E. Baker, R. R. Bennett, C. R. Armbruster, K. A. Lewis, R. L. Tarnopol, C. J. Lomba, D. A. Hogan, M. R. Parsek, G. A. O'toole, R. Golestanian and G. C. Wong, *mBio*, 2020, **11**, in collab. with F. M. Ausubel.

(174) S. Kreve and A. C. D. Reis, *Jpn Dent Sci Rev*, 2021, **57**, 85–96.

(175) R. S. Friedlander, N. Vogel and J. Aizenberg, *Langmuir*, 2015, **31**, 6137–6144.

(176) R. M. do Nascimento, U. Sarig, N. C. da Cruz, V. R. de Carvalho, C. Eyssartier, L. Siad, J.-F. Ganghoffer, A. C. Hernandes and R. Rahouadj, *Adv. Theory Simul.*, 2019, **2**, 1900079.

(177) M. Saini, Y. Singh, P. Arora, V. Arora and K. Jain, *World J Clin Cases*, 2015, **3**, 52–57.

(178) N. Vanoyan, S. L. Walker, O. Gillor and M. Herzberg, *Langmuir*, 2010, **26**, 12089–12094.

(179) W. W. Navarre and O. Schneewind, *Microbiology and Molecular Biology Reviews*, 1999, **63**, 174–229.

(180) A. van Belkum, D. C. Melles, J. Nouwen, W. B. van Leeuwen, W. van Wamel, M. C. Vos, H. F. L. Wertheim and H. A. Verbrugh, *Infection, Genetics and Evolution*, 2009, **9**, 32–47.

(181) J. M. Patti, B. L. Allen, M. J. McGavin and M. Hook, *Annual Review of Microbiology*, 1994, **48**, 585–618.

(182) Y. Zhu, E. C. Weiss, M. Otto, P. D. Fey, M. S. Smeltzer and G. A. Somerville, *Infection and Immunity*, 2007, **75**, 4219–4226.

(183) M. Idrees, S. Sawant, N. Karodia and A. Rahman, *International Journal of Environmental Research and Public Health*, 2021, **18**, 7602.

(184) S. P. Watson, M. O. Clements and S. J. Foster, *J. Bacteriol.*, 1998, **180**, 1750–1758.

(185) C.-H. Liao and L. Shollenberger, *Lett. Appl. Microbiol.*, 2003, **37**, 45–50.

(186) D. Zhou, W. Song, S. Zhang, L. Chen and G. Ge, *RSC Adv.*, 2022, **12**, 29727–29733.

(187) C.-J. Huang, L.-C. Wang, C.-Y. Liu, A. S. T. Chiang and Y.-C. Chang, *Biointerphases*, 2014, **9**, 029010.

(188) H. A. Harms, N. Tétreault, V. Gusak, B. Kasemo and M. Grätzel, *Phys. Chem. Chem. Phys.*, 2012, **14**, 9037–9040.

(189) N. Tymchenko, E. Nilebäck, M. V. Voinova, J. Gold, B. Kasemo and S. Svedhem, *Biointerphases*, 2012, **7**, 43.

(190) A. Pomorska, D. Shchukin, R. Hammond, M. A. Cooper, G. Grundmeier and D. Johannsmann, *Anal Chem*, 2010, **82**, 2237–2242.

(191) A. Granéli, M. Edvardsson and F. Höök, *Chemphyschem*, 2004, **5**, 729–733.

(192) C. Tonda-Turo, I. Carmagnola and G. Ciardelli, *Front. Bioeng. Biotechnol.*, 2018, **6**.

(193) H.-C. Flemming and J. Wingender, *Nat Rev Microbiol*, 2010, **8**, 623–633.

(194) H.-C. Flemming, J. Wingender, U. Szewzyk, P. Steinberg, S. A. Rice and S. Kjelleberg, *Nat Rev Microbiol*, 2016, **14**, 563–575.

(195) M. R. Parsek and E. P. Greenberg, *Trends Microbiol*, 2005, **13**, 27–33.

(196) J. Salazar, M.-À. Amer, A. Turó, N. Castro, M. Navarro, S. Soto, Y. Gabasa, Y. López and J.-A. Chávez, *Chemosensors*, 2023, **11**, 68.

(197) A. Itoh and M. Ichihashi, *Meas. Sci. Technol.*, 2010, **22**, 015402.

(198) W. Li, M. S. Siddique, N. Graham and W. Yu, *Environ. Sci. Technol.*, 2022, **56**, 8908–8919.

(199) K. Ivanova, A. Ivanova, J. Hoyo, S. Pérez-Rafael and T. Tzanov, *Int J Mol Sci*, 2022, **23**, 7632.

(200) I. W. Sutherland, *Microbiology*, 2001, **147**, 3–9.

(201) P. Stoodley, R. Cargo, C. J. Rupp, S. Wilson and I. Klapper, *Journal of Industrial Microbiology and Biotechnology*, 2002, **29**, 361–367.

(202) M. Piatek, C. O'Beirne, Z. Beato, M. Tacke and K. Kavanagh, *Antibiotics (Basel)*, 2023, **12**, 348.

(203) M. R. Nejadnik, A. L. J. Olsson, P. K. Sharma, H. C. van der Mei, W. Norde and H. J. Busscher, *Langmuir*, 2009, **25**, 6245–6249.

(204) Y. Shan, L. Liu, Y. Liu, H. Harms and L. Y. Wick, *Environ. Sci. Technol.*, 2020, **54**, 14036–14045.

(205) M. Kostakioti, M. Hadjifrangiskou and S. J. Hultgren, *Cold Spring Harb Perspect Med*, 2013, **3**, a010306.

(206) M. Klausen, A. Heydorn, P. Ragas, L. Lambertsen, A. Aaes-Jørgensen, S. Molin and T. Tolker-Nielsen, *Mol Microbiol*, 2003, **48**, 1511–1524.

(207) T. J. Foster and M. Höök, *Trends Microbiol*, 1998, **6**, 484–488.

(208) S. E. Cramton, C. Gerke, N. F. Schnell, W. W. Nichols and F. Götz, *Infect Immun*, 1999, **67**, 5427–5433.

(209) A. Touhami and T. Beveridge, *Journal of bacteriology*, 2004, **186**, 3286–95.

(210) Y. F. Dufrêne, *Trends Microbiol.*, 2015, **23**, 376–382.

(211) M. Gross, S. E. Cramton, F. Götz and A. Peschel, *Infect Immun*, 2001, **69**, 3423–3426.

(212) L. C. Powell, M. F. Pritchard, C. Emanuel, E. Onsøyen, P. D. Rye, C. J. Wright, K. E. Hill and D. W. Thomas, *Am J Respir Cell Mol Biol*, 2014, **50**, 483–492.

(213) R. Sonohara, N. Muramatsu, H. Ohshima and T. Kondo, *Biophys Chem*, 1995, **55**, 273–277.

(214) F. Götz, *Mol Microbiol*, 2002, **43**, 1367–1378.

(215) J. S. Mattick, *Annu Rev Microbiol*, 2002, **56**, 289–314.

(216) F. F. Tuon, L. R. Dantas, P. H. Suss and V. S. Tasca Ribeiro, *Pathogens*, 2022, **11**, 300.

(217) A. Persat, C. D. Nadell, M. K. Kim, F. Ingremeau, A. Siryaporn, K. Drescher, N. S. Wingreen, B. L. Bassler, Z. Gitai and H. A. Stone, *Cell*, 2015, **161**, 988–997.

(218) A. Ghafoor, I. D. Hay and B. H. A. Rehm, *Appl Environ Microbiol*, 2011, **77**, 5238–5246.

(219) T. Bjarnsholt, *APMIS Suppl*, 2013, 1–51.

(220) S. Kim, X.-H. Li, H.-J. Hwang and J.-H. Lee, *Appl Environ Microbiol*, 2020, **86**, e01584–20.

(221) K. Bisht, A. R. Luecke and C. A. Wakeman, *Front. Microbiol.*, 2023, **13**.

(222) T. M. Rode, S. Langsrud, A. Holck and T. Møretrø, *Int J Food Microbiol*, 2007, **116**, 372–383.

(223) E. Karatan and P. Watnick, *Microbiol Mol Biol Rev*, 2009, **73**, 310–347.

(224) E. E. Mann, K. C. Rice, B. R. Boles, J. L. Endres, D. Ranjit, L. Chandramohan, L. H. Tsang, M. S. Smeltzer, A. R. Horswill and K. W. Bayles, *PLOS ONE*, 2009, **4**, e5822.

(225) K. J. Lauderdale, B. R. Boles, A. L. Cheung and A. R. Horswill, *Infect Immun*, 2009, **77**, 1623–1635.

(226) H. R. Ali, P. Collier and R. Bayston, *Microorganisms*, 2024, **12**, 203.

(227) L. Netuschil, T. M. Auschill, A. Sculean and N. B. Arweiler, *BMC Oral Health*, 2014, **14**, 2.

(228) O. Makarova, P. Johnston, B. Walther, J. Rolff and U. Roesler, *Genome Announc*, 2017, **5**, e00293–17.

(229) C. Shaw, J. M. Stitt and S. T. Cowan, *Microbiology*, 1951, **5**, 1010–1023.

(230) M. J. Horsburgh, J. L. Aish, I. J. White, L. Shaw, J. K. Lithgow and S. J. Foster, *J Bacteriol*, 2002, **184**, 5457–5467.

(231) E. Peeters, G. Hooyberghs, S. Robijns, K. Waldrant, A. De Weerdt, N. Delattin, V. Liebens, S. Kucharíková, H. Tournu, N. Verstraeten, B. Dovgan, L. Girandon, M. Fröhlich, K. De Brucker, P. Van Dijck, J. Michiels, B. P. A. Cammue, K. Thevissen, J. Vanderleyden, E. Van der Eycken and H. P. Steenackers, *Antimicrob. Agents Chemother.*, 2016, **60**, 6483–6497.

(232) M. Dittmer, F. H. H. Brill, A. Kampe, M. Geffken, J.-D. Rembe, R. Moll, I. Alio, W. R. Streit, E. S. Debus, R. Smeets and E. K. Stuermer, *Biomedicines*, 2023, **11**, 2640.

(233) M. Borowicz, D. M. Krzyżanowska and S. Jafra, *Journal of Microbiological Methods*, 2023, **204**, 106656.

(234) E. K. Sully, N. Malachowa, B. O. Elmore, S. M. Alexander, J. K. Femling, B. M. Gray, F. R. DeLeo, M. Otto, A. L. Cheung, B. S. Edwards, L. A. Sklar, A. R. Horswill, P. R. Hall and H. D. Gresham, *PLoS Pathog*, 2014, **10**, ed. E. P. Skaar, e1004174.

(235) P. R. Murray, *Medical microbiology [electronic resource]*, in collab. with K. S. Rosenthal and M. A. Pfaller, Elsevier, Amsterdam, Eighth edition., 2015.

(236) B. R. Boles and A. R. Horswill, *PLoS pathogens*, 2008, **4**, e1000052.

(237) N. Pant, S. Miranda-Hernandez, C. Rush, J. Warner and D. P. Eisen, *Front Pharmacol*, 2022, **13**, 989417.

(238) K. E. Beenken, L. N. Mrak, L. M. Griffin, A. K. Zielinska, L. N. Shaw, K. C. Rice, A. R. Horswill, K. W. Bayles and M. S. Smeltzer, *PLOS ONE*, 2010, **5**, e10790.

(239) U. Römling and C. Balsalobre, *J Intern Med*, 2012, **272**, 541–561.

(240) G. Brackman and T. Coenye, *Curr Pharm Des*, 2015, **21**, 5–11.

(241) D. A. Rasko, C. G. Moreira, D. R. Li, N. C. Reading, J. M. Ritchie, M. K. Waldor, N. Williams, R. Taussig, S. Wei, M. Roth, D. T. Hughes, J. F. Huntley, M. W. Fina, J. R. Falck and V. Sperandio, *Science*, 2008, **321**, 1078–1080.

(242) E. Dziubakiewicz, K. Hrynkiewicz, M. Walczyk and B. Buszewski, *Colloids Surf. B*, 2013, **104**, 122–127.

(243) H. Bai, J. Chen, Y. Hu, G. Wang, W. Liu and E. Lamy, *Korean J. Chem. Eng.*, 2022, **39**, 38–57.

(244) T. B. Cavitt and N. Pathak, *Pharmaceuticals (Basel)*, 2021, **14**, 977.

(245) D. Cunliffe, C. De las Heras Alarcon, V. Peters, J. Smith and C. Alexander, *Langmuir*, 2003, **19**, 2888–2899.

(246) M. C. van Loosdrecht, J. Lyklema, W. Norde and A. J. Zehnder, *Microb Ecol*, 1989, **17**, 1–15.

(247) R. Bos, H. C. van der Mei and H. J. Busscher, *FEMS Microbiology Reviews*, 1999, **23**, 179–230.

(248) G. L. Dybwad, *J. Appl. Phys.*, 1985, **58**, 2789–2790.

(249) J. N. D'Amour, J. J. R. Stålgren, K. K. Kanazawa, C. W. Frank, M. Rodahl and D. Johannsmann, *Phys Rev Lett*, 2006, **96**, 058301.

(250) A. L. J. Olsson, H. C. van der Mei, D. Johannsmann, H. J. Busscher and P. K. Sharma, *Anal. Chem.*, 2012, **84**, 4504–4512.

(251) Q. Kang, Q. Shen, P. Zhang, H. Wang, Y. Sun and D. Shen, *Anal Chem*, 2018, **90**, 2796–2804.

(252) Z. Adamczyk, M. Sadowska and P. Żeliszewska, *Anal Chem*, 2020, **92**, 15087–15095.

(253) J. W. Costerton, P. S. Stewart and E. P. Greenberg, *Science*, 1999, **284**, 1318–1322.